EXPERIMENTAL INVESTIGATION OF SPACECRAFT RENDEZVOUS AND DOCKING BY DEVELOPMENT OF A 3 DEGREE OF FREEDOM SATELLITE SIMULATOR TESTBED

JOSHUA COOKSON

A THESIS SUBMITTED TO
THE FACULTY OF GRADUATE STUDIES
IN PARTIAL FULFILLMENT OF THE REQUIREMENTS
FOR THE DEGREE OF
MASTER OF SCIENCE

GRADUATE PROGRAM IN EARTH AND SPACE SCIENCE
YORK UNIVERSITY
TORONTO, ONTARIO

AUGUST 2019

Abstract

This thesis developed a 3 degree of freedom air bearing satellite simulator testbed. The major components of this testbed are a 2-meter by 4-meter granite table, a pair of satellite simulators, and a passive infrared marker array. The goal of this implementation was to achieve soft docking between 2 satellite simulators while relying only on hardware and systems onboard the satellite simulator. The satellite simulators make use of compressed air stored onboard in tanks to supply the air bearing and gas thrusters. The air bearing system provides a thin cushion of air for the satellite simulator to float on, removing surface contact and friction between the satellite simulator and the granite table. This produces a 3 degree of freedom system which is effectively free of the effects of gravity. The infrared marker array is used to provide reference points similar to stars to enable an onboard positioning system using a single observer. The experimental results obtained here demonstrate the successful implementation of this testbed.

Acknowledgments

I would like to thank my supervisor, Dr. George Z.H. Zhu, for his guidance and assistance throughout the undertaking of this thesis research. I would also like to thank Dr. Franz Newland and the late Dr. George Vukovich for the guidance they have given me over the course of this project.

I would also like to thank my family, friends, and colleagues who have always been there for me.

Table of Contents

List of Tables

List of Figures

Symbols and Conventions

All values are given in SI units, such as seconds (s), and meters (m), unless specified otherwise.

List of Symbols

d_i	Distance from identified point *i* and the satellite simulator center location
d_{ij}	Distance between object *i* and object *j*
e	Control error term
K_d	Derivative gain
K_p	Proportional gain
n	Number of objects
u	Control output value
X, Y	Center coordinates of satellite simulator in the granite table reference frame
x_i, y_i	x and y coordinates of object *i* in the image reference frame
X_i, Y_i	X and Y coordinates of object *i* in the granite table reference frame
α	Total number of position solutions calculated by the positioning system
β	Total number of attitude solutions calculated by the positioning system
Δ	Conversion ratio, meters per pixel
θ	Satellite simulator attitude in the granite table reference frame
$\angle ijk$	The angle between points *i*, *j*, and *k*, where *j* is the vertex point

List of Abbreviations

DOF	Degree of Freedom
FOG	Fiber Optic Gyroscope
FPS	Frames Per Second
ft	feet
GEO	Geostationary Orbit
GNC	Guidance, Navigation, and Control
HIL	Hardware-In-The-Loop
IR	Infrared
m	meters
mm	millimeters
mNm	MilliNewton Meters
MPa	Mega Pascals
N	Newton
OBC	Onboard Computer
PD	Proportional Derivative
RVD	Rendezvous and Docking
SS	Satellite Simulator

Chapter 1 INTRODUCTION AND JUSTIFICATION

Summary: This chapter outlines the problem, justifies performing the research, and outlines the objective and the approach taken through the research, as well as summarizing the layout of this thesis.

1.1 Background

In the field of modern spaceflight, the applications for rendezvous and docking (RVD) capabilities for spacecraft are increasing. Rendezvous refers to the process of two or more objects coming together in the same vicinity and maintaining proximity. The actual proximity at which rendezvous occurs is subject to the requirements of the specific mission, some missions may determine successful rendezvous at several kilometers, while others may require rendezvous in the range of meters. Docking is the act of a spacecraft propelling itself on a trajectory which allows it to align and interface with a docking mechanism on a target body, while maintaining control to avoid a catastrophic collision. The act of docking itself is technically a collision, which requires the docking craft to be carefully and deliberately controlled to avoid damaging or destroying itself, its target, or other objects in the vicinity. Docking connections can be referred to as either being soft or hard. Soft

docking is done by contacting and connecting the docking mechanism of the spacecraft with the target, either with a magnetic or mechanical system. Hard docking occurs following soft docking where the spacecrafts form a rigid mechanical connection through the docking mechanism. [1]

Since the 1960's the concept of orbital RVD between spacecraft has been explored as a way to resupply spacecraft with fuel and crew, alter or construct spacecraft on orbit, and to service spacecraft on orbit. The ability to rendezvous and dock on orbit this opens many possibilities, such as construction of large structures that could not be sent up in a single launch, or to update or improve the performance of an existing system. This technology would also make large scale missions possible, such as a manned mission to other planets in the solar system, where a large crew transport vehicle or habitat would be required.

Flight applications for RVD first emerged during the age of the missions to the moon, the first successful docking on orbit occurred during Gemini VIII on March 16, 1966. [2] Since the days of Gemini docking technology has been an integral part of several large scale undertakings, such as the space stations Salyut in 1971, Skylab in 1973, MIR in 1986, and the International Space Station in 1998. [1] Docking technology was and is essential in both the construction and operations of these facilities, with modules docking on orbit to assemble into the larger structure that makes up the station, as well as capsules and shuttles docking with the stations to exchange crew and supplies to sustain operations. The ability to easily resupply the ISS is what enables research on subjects like the long term effects of

microgravity on the human body, with the One-Year Mission and Twins Study performed by NASA with astronauts spending 340 days in orbit. [3] [4]

In addition to supporting human operations in space, RVD technology could play a critical role in managing the growing problem of space debris around the Earth. Currently it is estimated that there are over 8400 tonnes of debris in orbit around the Earth, of this it is estimated that there are more than 34000 debris objects measure over 10 cm in size, 900000 debris objects between 1 cm and 10 cm, and 128 million debris objects smaller than 1 cm. [5] While space debris has been amassing since the first satellite was launched in 1957, the amount has increased dramatically in recent years, every launch produces more debris with spent rocket stages and release mechanisms for spacecraft being left in orbit. A few major incidents have dramatically increased the amount of space junk, these being the collision between the defunct COSMOS 2251 and Iridium 33 in 2009, the Chinese anti-satellite missile test destroying the weather satellite Fengyun-1C in 2007, and the recent Indian anti-satellite missile test on March 27, 2019. [6] [7] [8]

The development of RVD technology will be critical in managing the growing space debris problem. With the increasing number of satellites being launched, and several hundreds being launched to form new constellations for services such as global internet from OneWeb, Telesat, and SpaceX, as well as the growing popularity of cubesat and microsat operations, the number of spacecraft launches and the amount of space debris resulting from those launches is set to increase greatly. [9] [10] It is possible to develop spacecraft which seek out debris such as defunct satellites and leftover rocket components, dock with

them, and maneuver to deorbit the debris. Docking technology would also allow servicing satellites to attempt to repair or refuel satellites on orbit to stop them from becoming debris in the first place. This would be especially useful for satellites at geostationary orbit, GEO, which is a circular orbit located over the equator, with an inclination of 0°, at an altitude of 35786 km, and orbits in the direction of the Earths rotation. Due to the specific requirements of geostationary orbit there is limited space which would allow a satellite to be positioned over landmasses, as satellites need to be placed far enough apart to ensure they do not interfere with or collide with each other during insertion or operations. Given the limited space available and distance from the Earth, GEO satellites typically have a reserve amount of fuel onboard to use at the end of their life to push them into a higher graveyard orbit, where they will be abandoned and stay for 1000s of years. In the event of a GEO satellite becoming nonoperational in orbit, the area which it occupies is then unusable, or if the satellite drifts it may interfere or collide with neighboring satellites, since the satellite can't move on its own. With a servicing satellite the damaged or decommissioned GEO satellite could be brought to a safe graveyard orbit.

On orbit servicing of satellite would also be attractive to companies seeking to upgrade existing hardware in orbit, which could be done by docking a new module with an existing satellite or maintain large research spacecraft such as the Hubble and Kepler space telescopes, or the upcoming James Web Space Telescope. In these instances, it would be more cost effective to launch a small servicing satellite than an entire new spacecraft.

Recent advances in modern spaceflight have brought about successful autonomous docking with the ISS. The European Space Agency performed autonomous docking operations with the ISS starting in 2008 with the first ATV mission. The ATV spacecraft began autonomous operations at 40 km from the station and was able to successfully dock. [11] On March 3, 2019 the SpaceX Dragon capsule achieved fully autonomous docking with the ISS. [12] Prior to the successful implementation of autonomous docking technology, all spacecraft docking operations required human intervention, either through teleoperation of the spacecraft, or manual piloting by an astronaut. With this technological development there is now functional commercial RVD in operation.

Aside from debris management and satellite servicing, docking technology also has applications in construction on orbit. The ISS is made up of several modules which were launched separately and assembled on orbit. Future space stations will be constructed in the same way, such as the upcoming Lunar Gateway project. It is not possible with current rocket technology to launch a large and complex structure at a single launch, however it can be done in multiple smaller launches.

There are also a number of small satellite missions which are looking at RVD on orbit, such as the Cubesat Proximity Operations Demonstration (CPOD) mission [13], and the 3U RSat mission [14]. These small satellite missions provide on orbit demonstrations of RVD capabilities with a much lower cost than a conventional satellite mission, however the cost for a cubesat mission is still quite high being in the 10’s to 100’s of thousands of dollars or more.

From here it is easy to see that the potential applications for RVD technology are becoming increasingly important, however the barrier to developing this technology, or any space technology, is the extremely large cost of development and launch of a mission.

Through the research work presented here a 3 DOF satellite simulator testbed will be implemented for the purposes of ground testing the guidance, navigation, and control techniques for spacecraft RVD.

1.2 Justification of Research

The environments found on Earth and in space are quite different regarding the maneuvers which can be performed. These environmental differences are the key limiting factors in testing space RVD systems on the ground, most notably the effects of gravity. There are other limiting factors that are considered in ground testing of space systems, such as the presence of atmosphere, the thermal profile, and the local magnetic field, however the focus here will be on the limitations imposed by gravity for testing RVD.

It goes without saying that any object which is placed unsupported in free space near the ground will simply fall to the ground. This is the main challenge in testing the guidance, navigation, and control (GNC) algorithms of a flight system, there is a constant force being applied along the local gravity vector. This constant force makes it impossible to observe the movements of a system in free space.

1.3 Limitations of Existing Approaches

Currently there exist multiple solutions enabling ground testing of space GNC systems, however each only accomplishes this testing in a limited scope. Aside from computer simulations of systems, hardware testing can be performed using neutral buoyancy tanks, hardware-in-the-loop (HIL) testbeds, and air bearing testbeds.

Neutral buoyancy tanks are large tanks of water in which space flight operations can be tested. Neutral buoyancy refers to the nature of an object in water which neither sinks or floats past a certain depth; it simply remains suspended. Neutral buoyancy tanks are commonly used by NASA to train astronauts, as the neutral buoyancy is an analog for zero gravity. [15] The large size of these tanks enables structures such as the ISS to be mocked up within them, which provides a suitable place to train astronauts for operations during space walks at the ISS. Outside of training astronauts however, these tanks are not very useful for testing or developing space systems. The issues with these facilities are that water is generally a poor place to test exposed electronic components and waterproofing a spacecraft system would require it to be altered from the flight specifications. The water is also a viscous medium, meaning that it introduces a large amount of resistance to objects moving within it. This resistance would serve to damp out vibrations and inhibit motion.

HIL systems seek to emulate the 6 degree of freedom motions of spacecraft. These systems operate using 1 or more robot arms with an end effector that is representative of a spacecraft component such as a docking mechanism. These robotic arms are capable of manipulating the end effector such that it is able to achieve 6 DOF movement. One application for this

testbed would be for spacecraft docking, with the arm representing the spacecraft attempting to dock. [16] Either a stationary target or another arm emulating a moving target spacecraft would be used to simulate the docking event. These testbeds depend on complex simulations of the expected dynamics running on powerful computers driving closed loop control systems to manipulate the robotic arms. The arms themselves are only able to operate within a limited space which limits the testing area. As the arms are fixed to the ground and are driven by an external simulation and controller, the accuracy of the 6 DOF movements is entirely dependent on the accuracy of the simulation, as well as the response time of sensors within the arm and actuation speed of the arm itself.

Air bearing testbeds are another solution to test GNC systems on Earth, however they are different than the HIL systems. An air bearing refers to a bearing which utilizes air as a lubricant, in terms of a satellite testbed they can be employed to demonstrate either 3 or 5 DOF dynamics. These testbeds utilize a smooth and level platform, the plane of which is normal to the local gravity vector. The air bearing system is attached to a spacecraft simulator which allows it to slide over this surface without the effects of friction, providing free body motion within the plane. Movement is not possible in the vertical direction without the effects of gravity being introduced to the system, this also means that rotation is only possible about the vertical axis. These air bearing testbeds are restricted to the size of the level and smooth surface which is available, many of which measure in the realm of $1m^2$ and are made of glass panes or stone slabs, while larger testbeds such as NASA's air bearing floor testbed uses an epoxy coated floor to produce an area of 637 m^2. [17] Such a

large testbed is very useful for testing full-scale models of large spacecraft, however this is an extremely large and costly facility.

These testbeds are also limited by the fact that they require air to operate the air bearings. This air must either be stored onboard, which requires air tanks that must be charged and provide a finite operation time, or be supplied by an umbilical which introduces external forces which may act on the system as it is no longer truly free floating. The satellite simulator systems typically employed on an air bearing testbed are small and lightweight, which requires less compressed air to operate, as such onboard hardware is usually limited to the necessary actuators and a small onboard computer to drive them. This lack of computational power generally means that the systems are incapable of performing all computational processes onboard and must rely on external computers to relay commands.

It is also common to use software simulations in place of physical test facilities. These simulators can provide accurate and reliable simulations of the space environment and how physical systems should behave. Software simulations depend on accurate models of both the spacecraft or component which is being analyzed, as well as the physics of the environment. Software simulations can also be computationally taxing to run, requiring powerful hardware. The main limitation of software simulations is that they operate without the real errors or variances that hardware systems do, such as environmental noise, efficiencies of components, how motion influences systems. While software simulations may be able to effectively simulate the performance of a system, it is in an idealized way and does not factor in many physical variables which cannot generally be modeled.

1.4 Objective of Proposed Research

The objectives of this research are to:

1. Implement a 3 DOF satellite simulator testbed:
    a. For the purposes of testing autonomous RVD using only onboard hardware.
    b. Which can examine the characteristic dynamics of the 0g environment.
    c. Which can examine the soft contact dynamics in a 0g environment.
2. Develop a positioning system which allows a single observer onboard the satellite simulator to determine the simulators absolute position to within 1 cm, and attitude within 0.5°.
3. Develop a pair of satellite simulators which are:
    a. Capable of operating with hardware systems limited to what would be theoretically capable of operating in the space environment. Ex. Cooling computer hardware without relying on a fan which would introduce a gyroscopic force and relies on air as a medium.
    b. Capable of performing all GNC operations using only onboard systems.
    c. Capable of determining their own position relative to a known target to within 1 cm and 0.5°.
    d. Capable of planning and executing a trajectory to the target from an initial distance less than 2 m.
    e. Capable of performing soft docking with a stable, stationary target and avoiding tumbling after docking.

1.5 Methodology of Approach

The approach taken to this research project begins with a detailed literature review. This review focuses on existing ground test facilities for zero and microgravity, including existing air bearing testbeds and alternative solutions.

The development of this testbed incorporates two key aspects; the hardware systems, and the software systems. The fundamentals of a 3 DOF satellite simulator testbed require many components and aspects of the system to be the same between all testbeds. These testbeds require a level and consistent surface which a satellite simulator can be tested on using some method of eliminating friction with the surface, as well as some method of controlling and tracking the simulator as it operates. Existing solutions all use an optical bench platform, air bearings mounted on the satellite simulators, and off board computing. Significant focus in this research was put into making the satellite simulators for this testbed as similar to flight satellites as possible, by being able to operate independently of off board hardware. As such the development of an absolute positioning system on the satellite simulator which does not depend on computing power from external sources or external data plays a key role in the development of this testbed.

The remainder of the research focuses on the additional hardware and software systems required for docking operations to be performed, as well as the laboratory setup and equipment. The experimental results will support the successful implementation of this system and accomplishment of the research objectives that have been outlined.

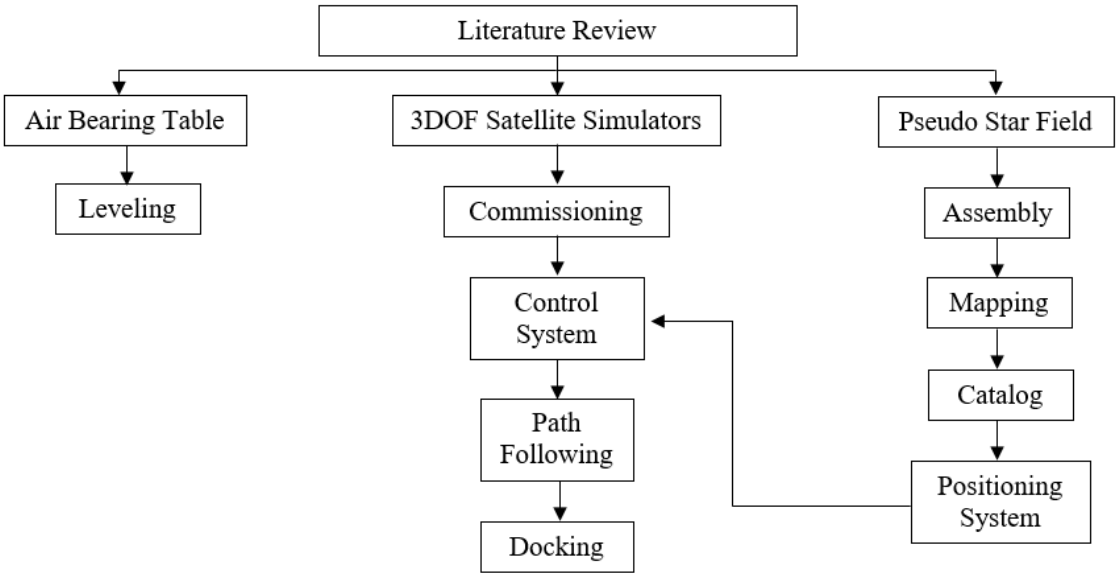

Figure 1.1 – Approach Outline

1.6 Outline of Thesis

This document contains 8 chapters. Following this introduction in Chapter 1, Chapter 2 outlines and reviews relevant work performed by others in similar areas of study, notably existing zero and microgravity test environments, existing 3 DOF testbeds, and existing 5 DOF testbeds. Chapter 3 gives an in-depth breakdown of the hardware systems implemented in this testbed. Chapter 4 gives a detailed breakdown of the software systems developed to enable the operations of this testbed. Chapter 5 goes over the various experimental results collected through testing of each of the systems and aspects of operation. Chapter 6 concludes this thesis, identifies the original contributions of this research, and outlines the directions for future work with this testbed.

Chapter 2 LITERATURE REVIEW

Summary: ground testing of space flight systems and algorithms is essential for the development and implementation of new space technologies. There are several different ways that systems can be tested on Earth to analyze how they would perform in the space environment. The focus of this chapter will be on the various ways of testing GNC systems for the behaviours due to microgravity and zero gravity.

2.1 Existing Zero/Microgravity Testing Technologies

Studying the effects of the zero and microgravity environment can provide useful data for many different areas of space flight research. Testing the effects of reduced gravity conditions is essential for training astronauts, examining the biological effects on organisms, and for analyzing the dynamics and behaviours of systems. The common ways of testing for the effects of reduced gravity on Earth are through various technologies, such as neutral buoyancy tanks, drop towers, parabolic flights, and air bearings.

A neutral buoyancy tank is commonly used to create an environment where it possible to examine the effects of microgravity with 6DOF for long periods of time. The tank itself

must be sized such that it can contain whatever test body within it, and is filled with a medium, typically water. The body which is submerged in the tank is balanced such that at a certain depth it neither sinks further down nor floats up. [15] A facility such as this is advantageous since the environment can be sustained for very long periods of time, making it ideal for long duration tests such as astronaut training exercises.

Neutral buoyancy testing can also be advantageous for testing 6DOF spaceflight maneuvers for satellites, such a testbed is proposed by Sun et. al [18]. To test the behaviours of a spacecraft in a neutral buoyancy tank, an analog of the spacecraft must be created which is capable of operations underwater. The test body developed by Sun for that testbed was small and contained an inertial measurement unit (IMU), a computer, battery, and utilized propellers to maneuver. Considerations for such a testbed are the drag forces introduced to the body by the water the system is moving through, and the limitations of the onboard hardware. As the system needs to be small, balanced, and waterproof, off board systems are used to track and operate the test body.

The simplest and most common method of microgravity testing is with a drop tower. A drop tower is simply a tall enclosed structure where an object can be dropped. Where the inertial force of a falling object is equal in magnitude to the force of gravity the object is effectively weightless. The NASA Glenn Research Center has been operating drop towers for decades now, the earliest in the 1950's standing 3.5 meters tall provided a 0.015g environment for 1 second. Later facilities were taller to achieve longer test periods, a 30.5-meter facility capable of 2.2 seconds, and a 131-meter facility capable of 5.2 seconds.

These testing facilities are also susceptible to the effects of air drag which provides resistance to the falling object. This air drag acts on the falling object and interferes with the simulation of 0g, which is why the 3.5-meter tower, for example, could only achieve 0.015g. to combat this a drop tower is commonly constructed as a vacuum chamber, with the drop tower housing a tube which is able to be used as a vacuum chamber. [19] A similar drop tower facility is the ZARM drop tower in Bremen, Germany which stands at 146-meters, and is capable of dropping for 4.74 seconds, or 9.3 seconds using a catapult system, under vacuum. [20] [21] [22]

Even under vacuum conditions, a drop tower will still have some residual effects of gravity. As the residual gravity in these test chambers is very small, it is very difficult to measure, and requires either a very sensitive accelerometer or a very precise timing system. An accelerometer would allow the residual acceleration due to gravity to be measured directly, while the timing system would allow the acceleration to be determined by the temporal displacement of the test body as it falls. An experiment to measure the residual acceleration due to gravity in the Beijing drop tower was undertaken by Liu et al. and using a high precision accelerometer measured it to be better than $2x10^{-4}$g. [23]

Drop tower facilities are capable of providing good test environments for microgravity, and are relatively simple to implement. These facilities however are limited to short duration tests due to the limited free fall time for a single test, and the test object must be dropped within the limited space of the test chamber, usually contained within a capsule which can be safely collected at the bottom. This limits the size and duration of tests, and

is not really suitable for testing navigation and control of a system in microgravity, but is very good for static experiments.

Another alternative testing method for microgravity is through parabolic flights. A parabolic flight is where an aircraft climbs and descends in a parabolic trajectory, at the top of this parabola where the aircraft transitions from ascending to descending the aircraft is in freefall. During this phase the cabin of the aircraft is a microgravity environment, and lasts for 20-30 seconds. [24] This method of testing is quite similar to the drop tower facilities, however due to the nature of the aircraft it is difficult to operate the environment under vacuum, but do achieve a longer test time and have a much larger testing volume.

The main advantages to a parabolic flight is that it is a relatively simple task to fly a plane on a parabolic trajectory, with an experienced pilot, and be able to repeat the same trajectory multiple times in a single flight to increase the testing time. The testing space is also contained within the volume of the aircraft, so the space available does depend on the which aircraft is being used, however the space also houses human occupants to monitor and oversee the experiments being done. This makes the testing environment ideal for testing technologies such as docking mechanisms and deployment mechanisms, as well as examining the effects of microgravity on people. [25] [26]

Given the large cost of operating an aircraft with an experienced crew, these testing facilities are operated by larger agencies such as the Canadian Space Agency (CSA) or National Aeronautics and Space Administration (NASA), and time is given to smaller entities to perform experiments.

Another alternative microgravity testing method makes use of air bearing technology. An air bearing is a bearing which uses a film of air as a lubricant to eliminate surface contact. While this technology cannot truly emulate the microgravity environment, it does balance out the influences of the Earths gravity on a body.

2.2 Existing 3 DOF Testbeds

One class of 3 DOF testbed is comprised of 3 key components, an air bearing platform, a satellite hardware simulator, and a tracking and control system. 3 DOF testbeds use a satellite hardware simulator with 3DOF, 2 translational and 1 rotational, and are commonly used to verify simulations and models [27], develop autonomous satellite systems [28], and test guidance, navigation, and control algorithms (GNC) [29], for autonomous operations, proximity operations [30] [31], RVD operations [32], and operations involving robotic manipulators [33] [34].

An air bearing testbed requires a platform which is consistently flat, smooth, and level. Materials commonly used for this are glass plates, granite slabs, and epoxy coated surfaces such as a floor. The materials selected each have some advantages and disadvantages. Glass plates can be obtained for a relatively low cost; however, the size of the glass plate is limited due to the difficulties of manufacturing a single plate of glass that is large, large plates of glass can also bend or warp is they are not sufficiently thick or properly supported. An alternative to glass is granite. Granite slabs provide a very stable platform where the surface is able to be machined very flat and smooth, and granite is commonly used for optical benches which have the same requirements as an air bearing platform. Granite slabs

are available in large sizes, such as 4-meters square, however, to have a slab that size be stable it must be quite thick. This large volume makes the slabs extremely heavy, which makes shipping them and assembling the testbed itself quite difficult and potentially expensive. A third alternative is to use an epoxy resin to coat a surface. Using this method, it is possible to create an air bearing surface which is significantly larger than any of the other alternatives. However getting such a large surface to be the same quality in all places can be difficult, and for a very large surface it may not be possible to adjust the level of the surface afterwards. [35]

The satellite simulators comprise the test vehicles which operate upon the air bearing platform using an air bearing system to eliminate surface friction and move freely in dimensions which are independent of the local gravity vector. As the air bearing platform is leveled, the surface which the satellite simulators move over is perpendicular to the local gravity vector. This removes the influence of the local gravity vector from the 3 DOF which the satellite simulators move in.

The tracking systems are responsible for observing the position and motions of the satellite simulators as they operate. Existing solutions employ a series of external cameras connected to a powerful computer to process the multiple video feeds and track the simulators. Common systems for this are Optitrack and Vicon, both commercially available, and are capable of providing position updates with sub-millimeter and sub-degree precision, and at rates above 100 Hz. [36]

The POSEIDYN test bed at the Naval Postgraduate School is a notable air bearing testbed. The POSEIDYN test bed makes use of a 4 m X 4 m granite slab as an air bearing platform, and has been used to develop multiple and operate multiple satellite simulators for the purposes of testing GNC algorithms. The tracking system employed for this test bed is composed of 10 Vicon cameras powered by an external computer. The 3 DOF satellite simulators operate using compressed air stored in onboard tanks to operate the air bearings and 8 gas thrusters, and a small onboard computer to operate the systems, however the required computationally intensive work is done off board, such as the tracking system, and relayed over a wireless network. The satellite simulators in this testbed also make use of technologies such as fiber optic gyroscopes (FOG), and reaction wheels (RW). [31]

There exist many 3 DOF testbeds at many institutions, the majority of which are granite or glass, and are between 1 and 2 meters squared in size. There are a few granite testbeds measuring larger than 3 meters squared, however not many. The larger testbeds use epoxy floors and measure several meters squared. [35] The 3DOF satellite simulators employed across all these testbeds have many things in common; utilizing compressed gas for an air bearing system, using gas thrusters/reaction wheels to maneuver, and using gyroscopes and external cameras to track to the position and orientation of the system.

A short summary of a few testbeds is given below in Table 2.1.

Table 2.1 - Testbed Summary

Location	Material	Size	Tracking System
Florida Institute of Technology [28]	Glass	1.8 X 3.6 m	Optitrack
Space Research Center PAS [34]	Granite	2 X 3 m	Custom External Pose Estimation System
NPS POSEIDYN [31]	Granite	4 X 4 m	Vicon
Georgia Tech ASTROS [36]	Epoxy	3.96 X 4.26 m	Vicon/SICK

2.3 5 DOF Testbeds

A 5DOF testbed is fundamentally the same as a 3DOF, however the satellite simulators employed are capable of motion with 2 additional degrees of freedom. The 5DOF satellite simulator operates using an air bearing base, the same a 3DOF would, however it has an additional hemispherical air bearing mounted on top of that base. A hemispherical air bearing is a round surface which sits within a cup, and the same way the air bearing pads remove surface contact with the epoxy surface, air is used to remove contact between this hemispherical surface and the cup. This allows parts mounted to the hemisphere to rotate and tilt within a certain angular range with 3DOF. Since one of the degrees of freedom from the hemispherical air bearing, the rotation about the vertical axis, aligns with the rotational degree of freedom of the base, the total degrees of freedom are 5. The air bearing platforms and tracking systems requirements are not affected by the 5DOF nature of the testbed. One notable 5DOF testbed is ASTROS at Georgia Tech.

The ASTROS testbed uses an epoxy surface measuring 3.96 X 4.26 meters and uses a Vicon tracking systems along with a SICK laser sensor, capable of millimeter level accuracy and an update rate of 2 Hz, to provide inertial information about the system. [36] The satellite simulator uses 12 gas thrusters mounted in 4 clusters of 3 for control, as well as 4 variable-speed control moment gyroscopes (VSCMG) for fine attitude control. [36]

2.4 This Testbed

As has been discussed in this section, the implementation of air bearing testbeds is not uncommon. The testbed developed here will set itself apart from existing solutions by implementing a positioning system onboard the satellite simulators, removing the need for an expensive and computationally demanding external solution, and by having the satellite simulators operate using only onboard systems. These differences attempt to bring the hardware systems of the satellite simulators closer to that of actual flight satellites. In this implementation, the use of onboard systems without reliance on external equipment seeks to better emulate autonomous operations.

Chapter 3 HARDWARE SYSTEMS

Summary: This chapter covers the various hardware systems implemented and developed through this research. Firstly, the systems requirements for the systems are outlined, then each subsequent section details the specific design parameters and results of each system.

3.1 Systems Overview

The testbed designed here consists of 3 major subsystems: a granite air bearing table, 2 air bearing satellite simulators (SS), and a pseudo-galactic star system.

The granite table is required to provide a level and smooth surface which is consistent at all points across it. The air bearing SS are required to be capable of performing all required operations and calculations using only onboard systems and technologies which would theoretically work in the space environment; however no components are required to be space grade as this testbed is intended for ground tests only. The star system is required to provide control points for the SS positioning system to observe in order to calculate its position and attitude at all points across the granite table surface. While it is referred to as

a star system here, it is an array of infrared markers which are distributed above the surface of the granite table and do not reflect or represent any actual stars.

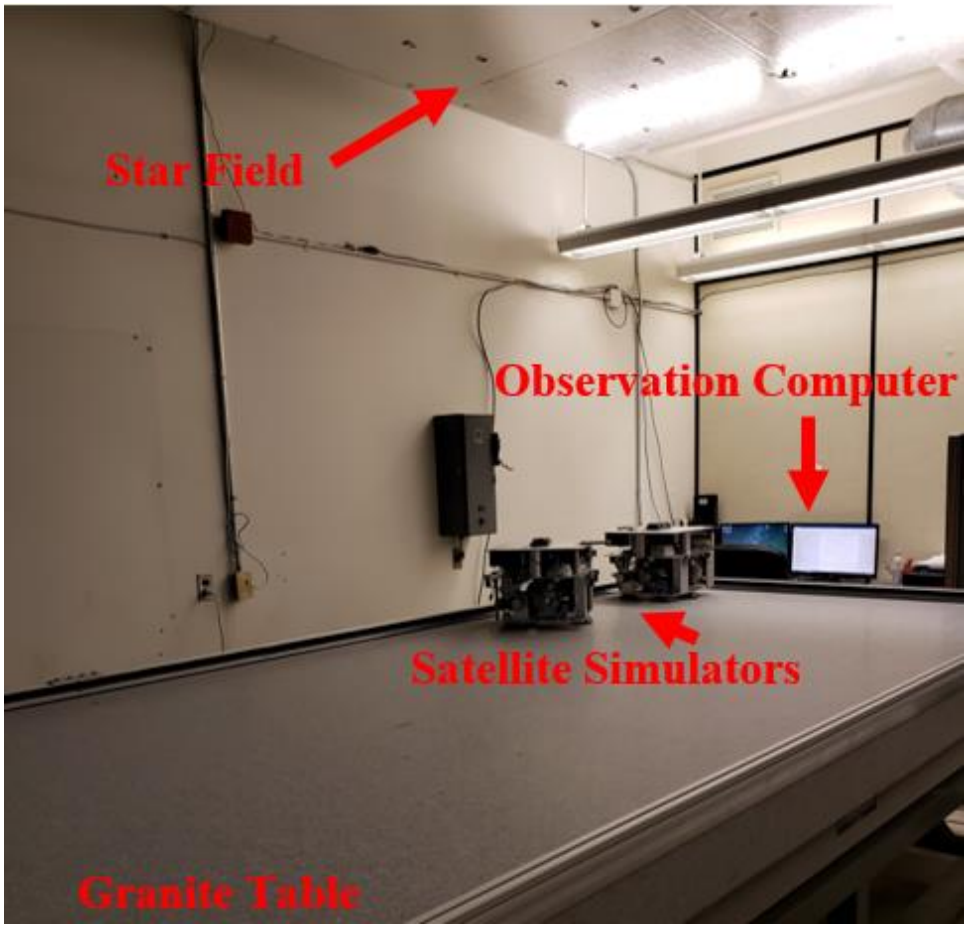

Figure 3.1 - Laboratory Setup

3.2 Granite Air Bearing Table

The testbed designed here operates using an air-bearing platform to allow for unrestricted planar motion. The air-bearing testbed makes use of an existing granite slab air bearing platform. The granite slab is a product of Standridge Granite, which measures 2-meters X 4-meters X 0.5 meters. The surface which has been machined to be consistently smooth and flat, meaning there are no local deviations in the surface quality of the table. For the

experiments being performed on the air-bearing platform, it must minimize the influences of gravity in the dimensions which are being analyzed, meaning that the surface plane must be accurately leveled. A level plane will be perpendicular to the local gravity vector, which minimizes the contribution of gravity on motions within the plane.

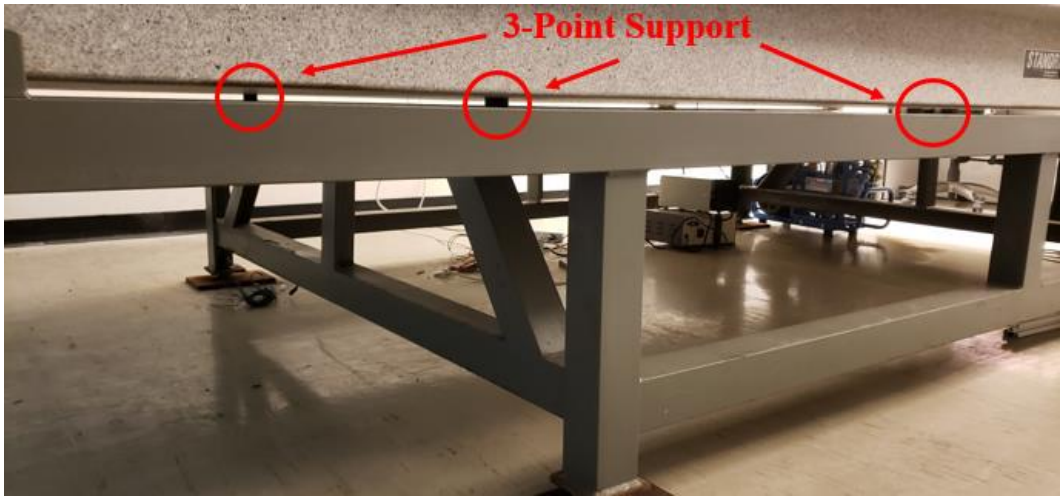

Figure 3.2 - Granite Table Supports

The slab sits on a 3-point support on a steel frame with 4 legs. This 3-point support system allows the plane of the table to be adjusted. In order for the air-bearing platform to be usable, the local gravity vector must be normal to the plane of the surface. The plane of the table is adjusted by adjusting the heights of the 4 bolts found on the bottom of each of the 4 legs of the support frame. Adjusting the height of these bolts forces that corner of the frame to be higher, thus adjusting the height of the table. As the table itself is mounted on a 3-point support system on top of this 4-point support system, the adjustments of the 4 bolts must be done carefully.

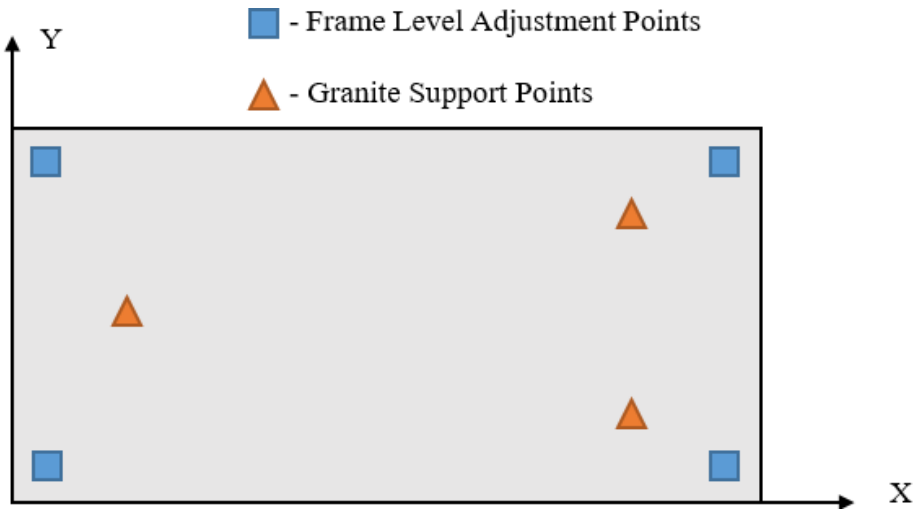

Figure 3.3 - Granite Table Support Outline

With the mounting points and adjustment points laid out in this way, the leveling procedure is more complex than for a traditional 3 point leveling system, as the 3 points simply support the table on the frame, however the frame itself relies on a 4 point leveling system. In order to adjust the level in the X dimension, the 2 adjustment points along the Y axis must be adjusted an equal amount. Adjusting these points by different amounts will result in an off axis adjustment of the level. Similarly, to adjust the level in the Y dimension the 2 adjustment points along the X axis must be adjusted.

In the absence of a high precision level, the granite surface was leveled by observing the drift of the SS as it floated on the surface and adjusting to counter this drift. This process of observation and adjustment was repeated multiple time until the residual drift of the SS allowed it 1 minute of uncontrolled drift before reaching the edge of the platform. Through further experimentation it was determined that the level of the granite surface was sufficient for operations, however it was not able to be measured.

Releveling of the surface is to be performed in the same manner, however releveling would only be required if the residual drift in the system is problematic for the experiments being performed. The drift of the SS is caused by the effects of gravity in the horizontal dimensions as the surface is not perfectly perpendicular to the local gravity vector. Different experiments being performed will have different tolerances for the residual effects of gravity.

3.3 Air-bearing Satellite Simulators

The SS used in this testbed were inherited from a prior project, and original design and construction was done by Tsinghua University, however modifications were made and are noted in the following, and all software was produced from scratch. [37]

The SS are small mock satellites which are designed to operate within the plane of the air bearing table. An air bearing is a bearing which uses a thin cushion of air to separate 2 surfaces. In this case, the SS has 3 circular metal feet which have micro machined grooves in the bottom and are fed with compressed air. The micro machined grooves distribute the air evenly and results in a layer of compressed air forming between the bottom of the feet and the surface of the granite. This layer of air eliminates surface contact, and thereby removes friction. This essentially frictionless surface allows the SS to float freely over the surface of the granite. With the granite surface being level, the local gravity vector only affects the SS in the vertical axis, and therefore has no effect on either of the translational degrees of freedom of the system, or the rotational degree. This results in a testbed which is essentially free from the effects of gravity within its degrees of freedom. The system is

still affected by air currents, so during flight operations the air circulation system within the lab is disabled. The resistance of static air is present, however is negligible.

The SS are constructed in 2 layers, as can be seen in Figure 3.4 - Figure 3.7. On the very bottom of the simulator the air bearing feet can be found. The first layer of the SS contains 2 high pressure air tanks which have a combined capacity of 2.0 L of compressed air at a pressure of 20 MPa. These tanks are connected to a pressure regulating valve which takes the pressure down from 20 MPa to 1 MPa, and then to another valve which reduces the pressure further to 0.4 MPa. Air at this pressure is then fed through a series of air lines, which were replaced from the original construction to minimize couplers to prevent leakage, which connect to 8 gas thrusters mounted on the 4 vertical faces of the SS, and to the air bearing feet located on the bottom of the SS.

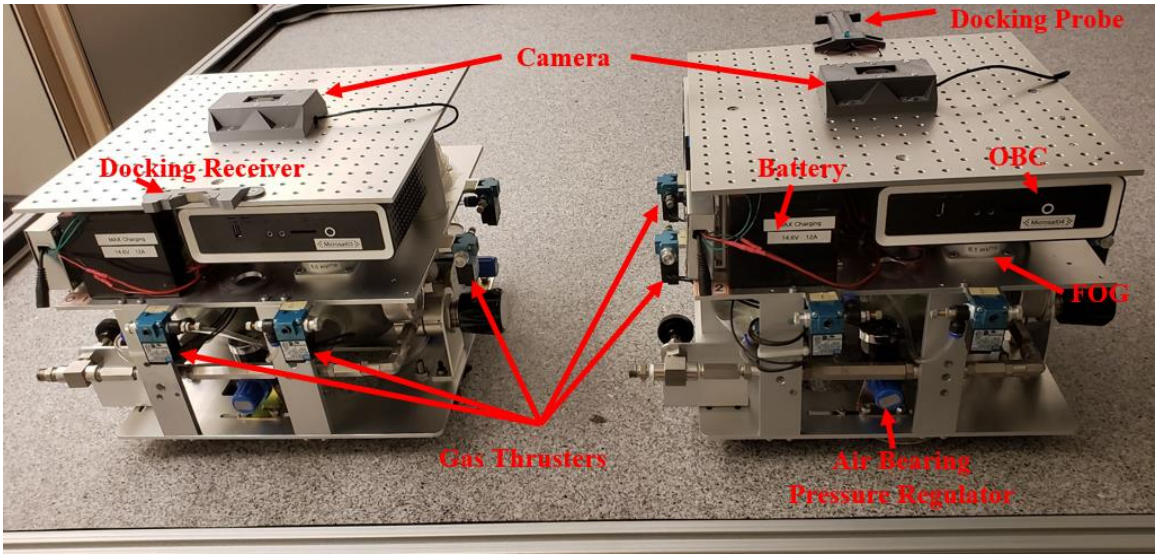

Figure 3.4 - Satellite Simulator Pair

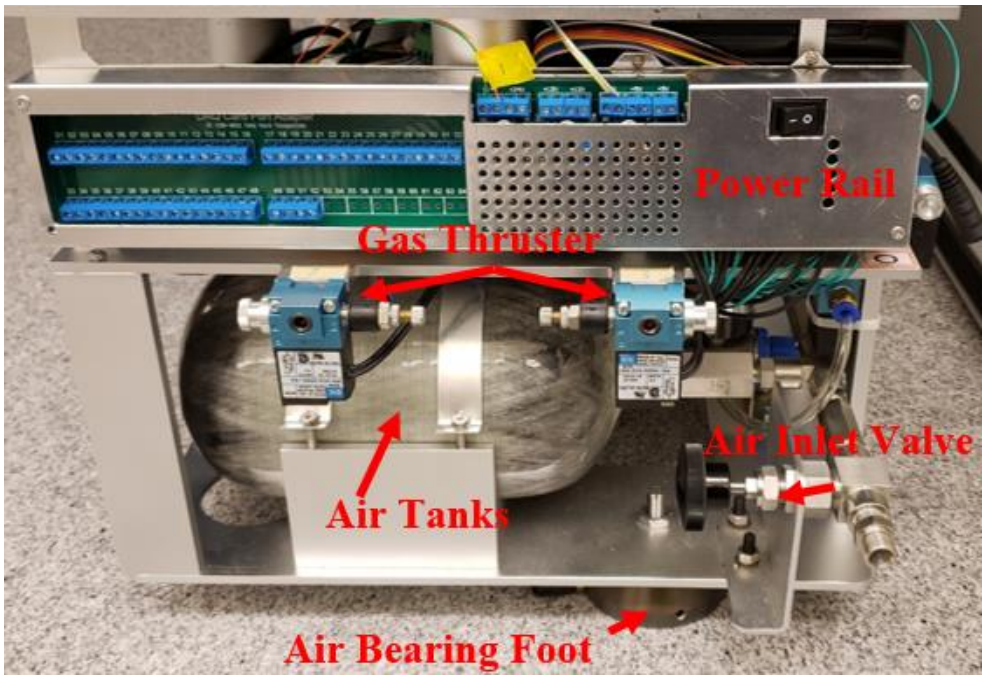

Figure 3.5 - Satellite Simulator Labeled

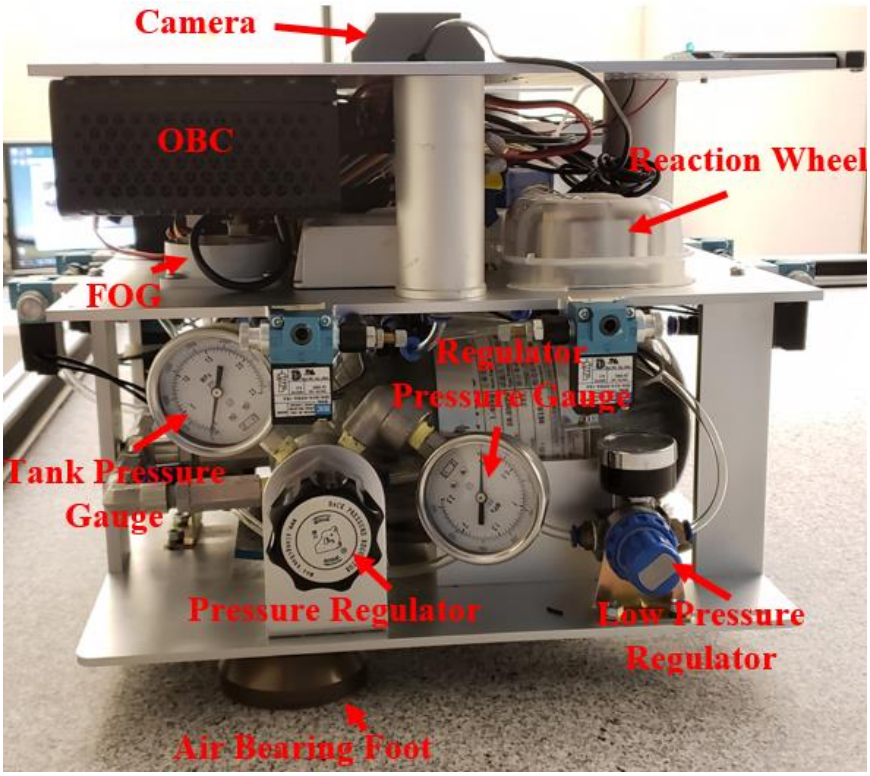

Figure 3.6 - Satellite Simulator Labeled

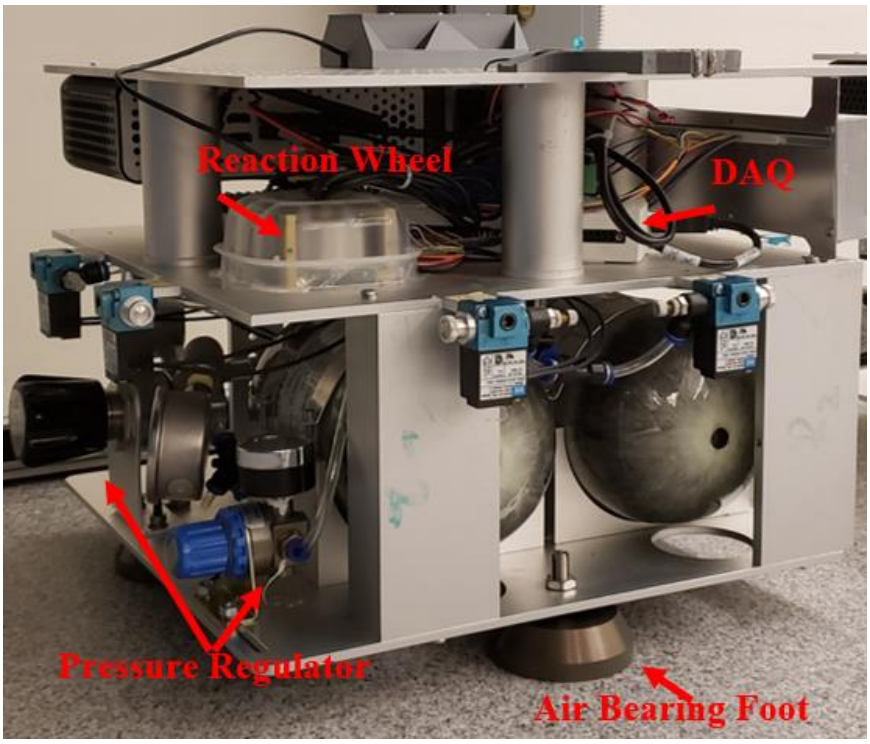

Figure 3.7 - Satellite Simulator Labeled

The second layer of the SS contains all hardware systems required to operate. Table 3.1 breaks down the major components of the SS and denotes whether the component was from the original inherited structure or modified. In this layer there is the battery and power distribution rail. The battery is a 12V LiFePO4 battery, which provides onboard power storage. This is sent to the distribution rail which contains a series of converters that output connections at 5V, 12V, and 24V. these connections available to attach hardware onboard that may require them. A 19V converter was added to facilitate the use of a different onboard computer (OBC). The original OBC was a small form factor Windows machine with a low power Celeron processor. This OBC was used to develop most of the operational software and was replaced due to the OBC beginning to malfunction and inhibit experimental operations. The current OBC is a small form factor Windows machine with

an i7-8550U processor, a solid-state hard drive, and a passive cooling system. It is capable of providing significantly more processing power than is found on a comparably sized, flight capable satellite, however this testbed is not intended to validate flight software, but rather to experiment with GNC and dynamics, so this is acceptable. This also allows for operations to be performed simultaneously that are only relevant in a lab environment, such as recording the screen or running a development environment to debug and develop code onboard.

The fact that the OBC has a solid-state hard drive and a passive cooling system is also critical. Traditional hard drives use spinning media, and typical cooling systems utilize fans to produce air currents which cool the hardware. For this simulator, the spinning of a hard drive or fan would produce an uncontrolled torque, and essentially act as a momentum wheel, which would interfere with the attitude and control of the SS. Additionally the fan used to cool the system would not function in vacuum, so it does not meet the specification that all components need to capable of theoretically functioning in the space environment.

Table 3.1 - Satellite Simulator Component Breakdown

Component	Description	Notes
SS Structure	Rigid body to which all components are attached	Original
High Pressure Air Tank (2)	Compressed air storage tank, 2.0L, 20 MPa	Original
High Pressure Reducing Valve	Control valve that reduces the incoming pressure from the air tank to 1 MPa	Original
Pressure Regulating Valve	Further reduces the pressure from 1 MPa down to 0.4 MPa to be used by the air bearing and gas thrusters	Original
Air Distribution Lines	Supplies air from the regulating valve at 0.4 MPa to the actuators	Replaced
Gas Thruster (8)	Regulated high pressure air feeding through an ejector nozzle, controlled by a solenoid valve	Calibrated
Air Bearing Feet (3)	3 circular pads to allow the SS to move with minimal friction	Replaced
Battery	12V, 150Wh, LiFePO4	Original
Power Distribution System	Converts battery voltage to 24 V, 19V, 12 V, and 5 V DC connections for various systems	Modified to include 19V
Fiber Optic Gyroscope	Fizoptika VG103PT	Replaced
Data Acquisition System	NI 6112 DAQ	Original
Camera	1080p Logitech C920 webcam	Redesigned mount
Reaction Wheel	Sinclair RW-0.01	Original
Onboard Computer	Zotac CI660-nano, i7-8550U, 16GB RAM	Replaced

The second layer also contains a fiber optic gyroscope, FOG. The original digital interface Fizoptika FOG on the SS was damaged from being wired incorrectly by the previous operator and was replaced with a similar analog Fizoptika FOG. This allows for precise

measurements of the rotation rate of the system and a simple interface with the data acquisition system (DAQ). The DAQ is also mounted on this layer. It is a USB device with multiple connections for analog and digital input and output, IO. This allows various systems, such as the FOG or gas thrusters, to interface with it to either send or receive data from the OBC. The reaction wheel for the system is mounted on the second layer of the SS as well. The reaction wheel interfaces with the OBC through an RS232 to USB converter, and is used as an attitude actuator. With the wheel mounted so that it rotates about an axis parallel to the Z-axis of the SS, it can spin at various rates to build or dissipate momentum. This change in momentum acts on the SS through the law of conservation of momentum, where the total momentum in the system before and after an event remains the same. This means that as the wheel increases velocity and therefore momentum rotating clockwise, the SS will begin rotating counter clockwise to conserve the total momentum of the system.

Mounted on the top of the SS body is Logitech C920 USB camera. This camera is capable of taking 1080p video at a rate of 30 frames per second (FPS). The original mount for this camera was a simple metal channel with a compression screw which drove into the side fo the camera to hold it in place. This mounting method warped the camera body over time and did not guarantee that the camera sat looking perpendicular to the top plate of the SS. A new mount was designed and 3D printed which allows the camera to sit within it, and matches the body shape of the camera to ensure it sits properly. The camera is fitted with an infrared (IR) band pass filter. Most digital camera sensors are sensitive to more than just the visible spectrum of light, however they tend to be most sensitive to the visible spectrum. Therefore, a digital camera will not normally display near infrared light in a picture. Some

digital cameras also have a built in IR filter which prevents the IR light from reaching the sensor. This camera was chosen since it does not have a built in IR filter. With the band pass filter the visible spectrum is filtered out and the sensor is only exposed to the IR light.

On top of the SS there is also a docking probe or a docking receiver, which were not present in the original system. The chaser SS is equipped with the docking probe, while the target SS is equipped with the docking receiver. These components are 3D printed to minimize machining work since the components have several intricate features. The docking components are passive, meaning that they have no moving parts. The focus of this SS design is to demonstrate the dynamics and systems requirements for docking, so the development of a docking mechanism with a more complex structure such as a gripper is not considered here. The docking probe and receiver are joined together through the use of magnets which are inlayed in the end of the probe and within the walls of the receiver. This magnetic attachment method allows the simulators to easily attach to one another without the need for additional mechanisms and provides enough strength to allow the 2 simulators to drift together without separating.

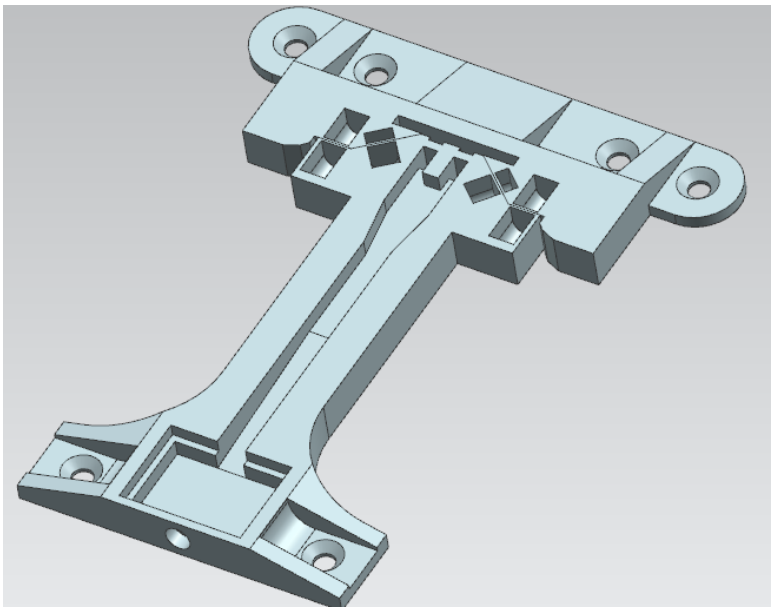

Figure 3.8 - Docking Probe and Receiver CAD Design

The docking mechanism is also designed to allow for the system to sense when docking has occurred. The docking receiver is designed to allow a metal plate to be inserted into the space where the end of the docking probe will reach, while the probe itself has slots in the end to allow a pair of wires to be run to contact this metal plate. The wires run through a channel down the length of the probe to a simple circuit, which when closed will provide a small voltage to a wire connected to a terminal on the DAQ, and to an LED indicator on the probe itself. The presence of this voltage at the DAQ indicates the circuit has been closed, which is only possible if the probe has contacted with receiver and successfully docked.

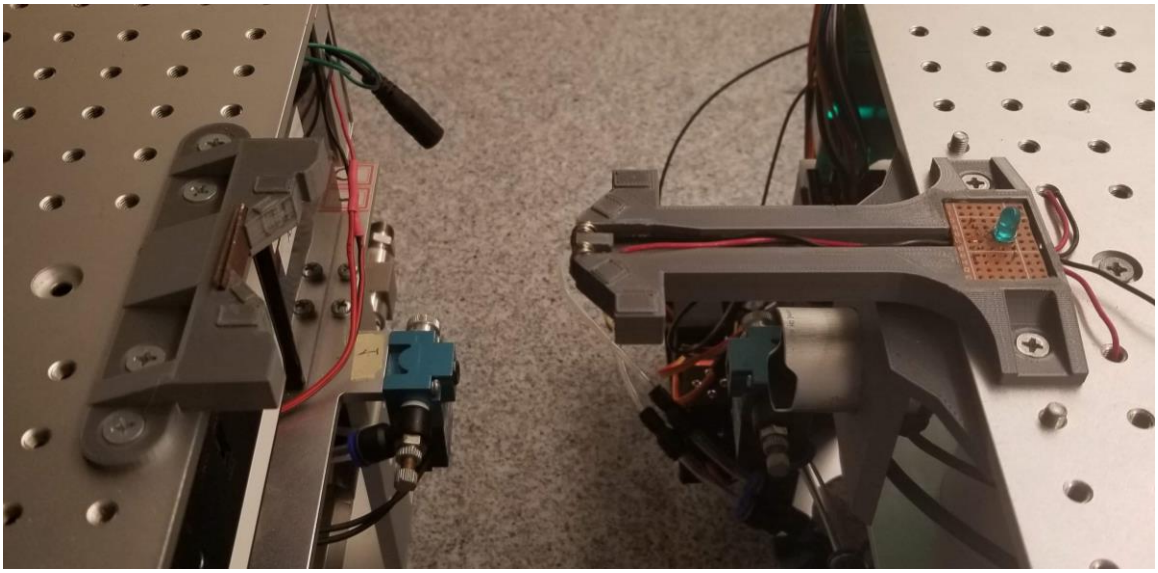

Figure 3.9 - Undocked Probe and Receiver

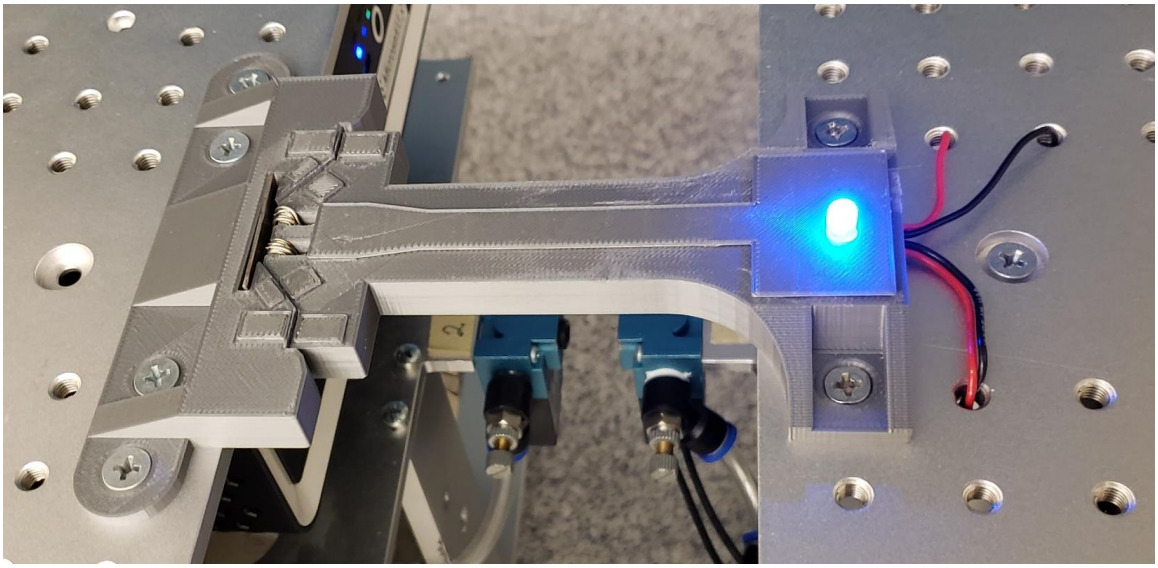

Figure 3.10 - Docked Probe and Receiver

3.4 Pseudo-Galactic Star System

One of the most critical types of data collected during any space flight mission is accurate positioning and attitude data. Common methods of positioning a spacecraft on orbit utilize the GPS satellite network if it is available or tracking from the ground using radar services

and using that information to propagate and correct the spacecraft's position based on its orbit. Determining attitude on orbit can be done with a variety of sensors, such as sun sensors, horizon sensors, and star trackers, each with different advantages. Common methods of attitude determination on orbit are magnetometers, GNSS, and star trackers. By measuring the direction of known stars relative to the spacecraft, the spacecraft orientation can be determined very accurately using a star tracker. In this lab, the absolute position and attitude determination system takes advantage of principles from both GPS and star tracking systems, such as calculation and refinement of position from a series of measured points and making calculations from the observed position and orientation of points compared to a catalog. While it does not function exactly as either system truly works in practice, it seeks to provide a reasonable analog within the lab environment.

Without access to either GPS satellites or actual stars in the lab, an array of infrared (IR) LED markers, herein referred to as "stars", Figure 3.11, is mounted in a plane over the granite surface. While there was an existing IR LED constellation installed in the lab, the constellation covered less that half the area of the table, did not have any related map data, multiple LEDs were damaged, and the array was partially obstructed by a pipe. The original intent of this array, according to Yao et. Al [37], was to provide a positioning system which functioned by calculating the relative shift between points located in successive images. This method if positioning may be accurate for tracking the relative change in position and attitude from some starting point, but provides no information as to where the SS truly is on the tables surface, or relative to another SS which may be operating with the same positioning system. As such the existing constellation was removed and redesigned from

scratch. The positioning system implemented here also functions completely differently than the existing system and does not make use of any part of it. The array implemented here was designed and constructed from scratch for the purposes of implementing this positioning system.

The reason for choosing to use IR LEDs rather than visible spectrum LEDs is that it is much easier to isolate the LEDs in an image if the visible spectrum can be removed entirely. In this case, an IR bandpass filter that was already present on the SS is used to remove the visible spectrum from the images. There are no sources of IR radiation present aside from the IR LEDs and are therefore easily identified within the image.

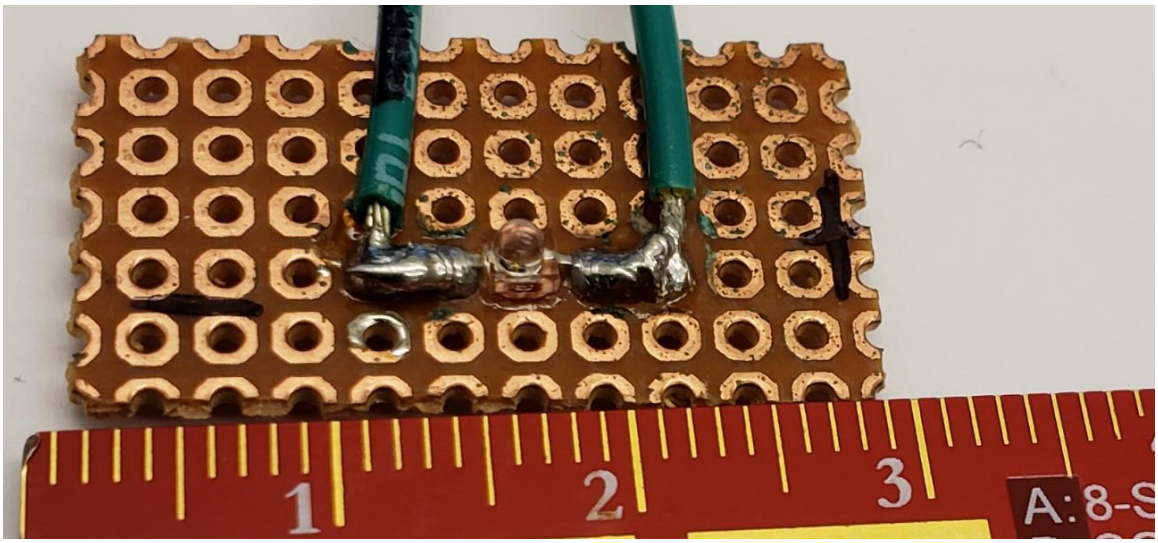

Figure 3.11 – IR LED Marker "Star"

The array consists of 36 stars distributed over an area of 2-meters by 4-meters, in a plane parallel to the granite surface, which are imaged by an onboard camera and used to calculate the SS position and attitude. The array itself is composed of 4 foam tiles, to which the circuit boards for the stars are mounted. These tiles are mounted above the granite table

using scaffolding attached to the ceiling. Figure 3.12 shows this scaffolding, while Figure 3.13 shows the tiles mounted.

Figure 3.12 - Star Field Support Scaffolding

Figure 3.13 - Mounted Star Field

3.4.1 Star Field Design

The placement of these stars was determined using a random number generator to randomly populate an area the same size as the granite table with points. This area was then traversed through in 1mm steps with a circular mask with a radius equal to 90% the shortest side of the field of view from the on-board camera. The camera has a 16:9 aspect ratio, therefore

choosing the short side of the rectangular field of view of the camera and using a circular field of view ensures that the point distribution will be independent of the angle of rotation of the camera relative to the star field. If at any point in the traversal the field of view did not contain at least 5 points the distribution was determined to not be usable.

This was performed for 10000 iterations with the quantity and position of the points being randomly generated, and the usable distributions being saved. The 5 distributions with the least number of points were plotted and the consistency of the distributions was evaluated visually to avoid point clusters. The final distribution which relied on the least number of points and had the most consistent distribution was taken to be the implemented design.

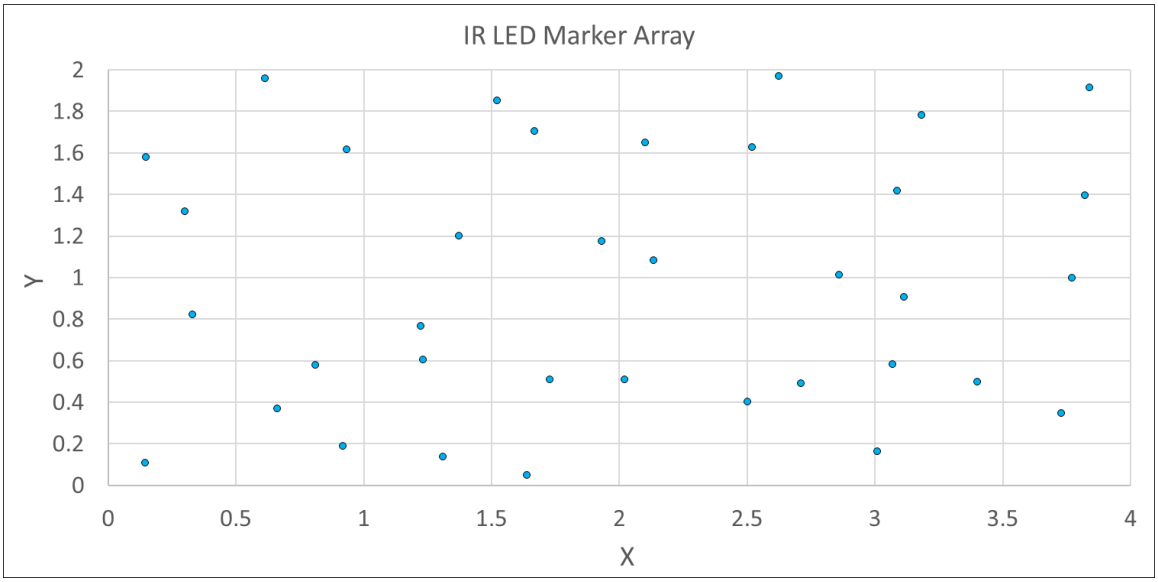

Figure 3.14 – IR LED Marker Array "Star Map"

The distribution chosen consists of 36 points as shown in Figure 3.14. The IR markers were placed in approximately the same locations as described in the chosen distribution, however due to the boards the LEDs are mounted on being comparatively large, and it being difficult to observe the point directly beneath the LED, the markers are not in exactly

the places defined by the generated distribution. This is acceptable however, as the planned distribution is random and the mapping process only accounted for a circular area which is smaller than the true field of view of the camera, small deviations are inconsequential.

As the granite table is rectangular, it is trivial to describe the area using a Cartesian coordinate system, with the X-axis being the 4-meter side, and the Y-axis being the 2-meter side. As the exact position of the stars in the mounted array is not accurately known relative to the granite table's coordinate frame, the position of each needed to be determined. These measurements were performed using a laser plumb line to find the location of the LED on the table's surface, and a tape measure to determine the distance to that point along each axis. The measurements for the Y dimension were taken by measuring with the tape measure from the X axis. While measurements were taken carefully to align the tape as best as possible with the edge of the table and the point being observed, alignment errors in the tape are still present and are not easily quantified. The measurements for the X dimension were taken similarly to the Y dimension, however a laser square was used to project the point on the surface to intersect with the X axis of the table. The distance to this intersecting line was measured from the Y axis, along the X axis. This provided all X measurements the same place to mount the tape measure, minimizing the alignment error as well as any deviation in the orthogonality of the sides of the table. If the sides of the table are not perfectly orthogonal, measuring both the X and Y dimensions from the opposing axis would incur distortions in the map, which is assumed to be have X and Y axis be orthogonal. Given that these measurements were performed using instruments with a limited accuracy, the accuracy of the points is also limited. The laser plumb line does not

have a provided accuracy from the manufacturer, however it is safe to assume that the laser does not align perfectly to the local vertical, however given that the surface of the table is consistently flat, this misalignment is approximately the same for all points. The beam has a diameter of 1mm, therefore the accuracy can be assumed to be ±0.5 mm since the beam can be seen to be over the diode however due to the diode lens it is difficult to determine the exact alignment of the laser over it. The tape measure has markers every millimeter, therefore the accuracy of measurements is taken to be ±0.5 mm, as the point being measured can be estimated to lie either on or in the middle of 2 markers by the observer. The combined accuracy of these measurements therefore produces a map of points with an accuracy of ±1 mm.

This provides a series of control points in the granite tables reference frame which can be used by the SS to calculate its absolute position and attitude. Each of these points is given a unique ID number, from 0 to 35, and the SS is equipped with a catalog with each unique ID number and the associated location measured relative to the granite table.

An excerpt of this catalog is shown in Table 3.2.

Table 3.2 - Star Location Catalog Excerpt

Star ID	X (m)	Y (m)
0	0.14	1.576
1	0.145	0.109
2	0.659	0.37
3	0.329	0.819
4	0.297	1.317
…		
31	3.181	1.7815
32	3.7285	0.345
33	3.779	0.9935
34	3.819	1.396
35	3.835	1.912

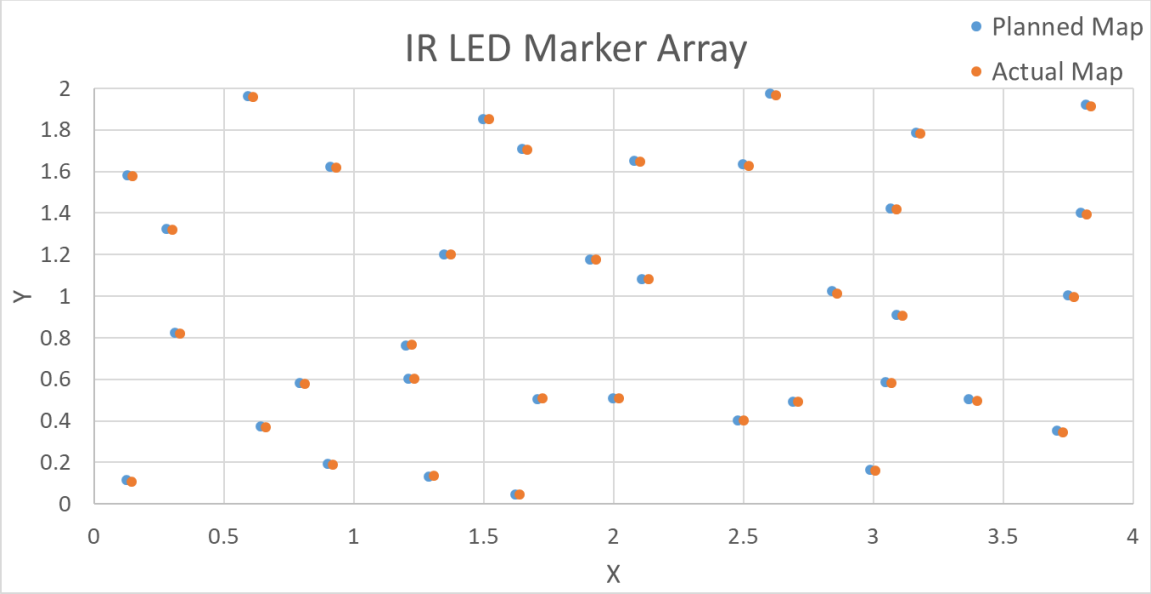

Figure 3.15 - Star Map Comparison

The distribution of the mapped markers is illustrated in Figure 3.15. The planned position of each star in the array is shown in blue, while the mapped position is shown in orange. It is worth noting that each mapped value appears to be translated along the X axis slightly and by approximately the same amount. One potential cause of this translation is the positioning error offset of the measuring tape. Given that all X dimension measurements were taken with the tape measure in the same position, it can be assumed that the measurement offset for all points is consistent. It is also likely that when the panels that make up the array were being installed, they were not aligned exactly with the table. This would account for the consistent shift in all points in the array. This difference between the planned map and the measured map is precisely the reason for performing this mapping operation, the determine what errors were made in constructing and assembling the array.

3.4.2 Star Catalogs

In order to provide absolute position and attitude information, the SS must be capable of identifying the specific stars and locations it is using in calculations. This is done by utilizing a series of catalogs containing known information about the star field. The first catalog was mentioned in the previous section containing a unique ID number for each star and its location. The second catalog the SS has onboard is used to identify the stars using a series of geometric relationships between the stars.

Table 3.3 below shows an excerpt of this relationship catalog.

Table 3.3 - Star Relationship Catalog Excerpt

S0	***S1***	***S2***	***S3***	***S4***	***d01 (m)***	***∠102°***	***∠012°***	***∠103°***	***∠013°***	***∠104°***	***∠014°***
8	12	7	11	15	0.16	89.846	69.185	174.06	4.452	104.95	59.274
8	12	7	11	6	0.16	89.846	69.185	174.06	4.452	139.4	31.364
8	12	7	11	13	0.16	89.846	69.185	174.06	4.452	16.886	157.32
…											
14	18	9	5	12	0.213	114.43	50.517	142.87	30.415	61.636	108.03
14	18	9	5	8	0.213	114.43	50.517	142.87	30.415	59.317	111.81
14	18	9	5	4	0.213	114.43	50.517	142.87	30.415	112.63	59.464
…											
19	20	25	30	32	0.49	127.47	39.922	107.15	53.296	169.71	7.366
19	20	25	11	22	0.49	127.47	39.922	25.512	139.25	77.808	79.093
19	20	25	11	32	0.49	127.47	39.922	25.512	139.25	169.71	7.366

The relationship catalog details the geometric relationships between a star, S0, and 4 of its neighboring stars, S1 – S4, listed in order of distance to S0 with S1 being the closest. The star numbers in the relationship catalog, listed as S0-S4, are the unique ID numbers of the stars as listed in the location catalog, Table 3.2.

For each star, the relationship catalog lists the relationships with the closest 10 stars in the field, in all unique permutations for S1 and S4 with S0 remaining constant for that particular star. The number of neighboring stars to use, 10, was chosen as not all stars are possible to have in view at any one time, so including stars spaced far apart would increase the size of the catalog and provide no benefit. A catalog containing the relationships between all permutations of all the stars would also be very large and greatly increase the time it takes to search the catalog.

The minimum number of neighboring stars required to function is 4, however if one of the neighboring stars in that set was outside the field of view the system would fail to identify that set. Increasing the number to 10 provides significant redundancy without a noticeable impact on search time, which was validated experimentally. 10 stars is also more than are in view in some areas of the granite table, the inclusion of this number of points ensures that at any point the stars in view will be listed in the catalog. This produces a relationship catalog with a total of 7560 unique entries defined, the equation defining the number of entries is given by (1), where n is the number of neighboring stars used.

$$\#_{entries} = 36 * \frac{n!}{(n-4)!\,4!} \qquad (1)$$

In order to use this catalog to identify the stars within view in the image, the catalog contains a series of geometric relationships between each group of 5 stars, which can also be calculated between the stars as they are observed by the camera onboard the SS to compare against.

The calculations of these identifying relationships are dependent on the listed order of the stars as S0-S4. The fact that these points are listed in order of proximity gives the system a logical way to sort the points in the image and helps avoid the possibility of reprocessing the same group of 5 stars in a different order, increasing efficiency.

The identifying values in the relationship catalog begin in column 6, with the value d01. The numbers listed in the column headers for columns after and including 6 reflect which of the points S0-S4 are being used, and the order they are being used in. The value d01 represents the distance between S0 and S1, calculated in meters. This distance is also used to sort the relationship catalog, making it easier to search. If the catalog were sorted based on the number for S0 then there would be no efficient way to search through it without first knowing the ID for the stars. Sorting by this distance value provides a simple way to organize the catalog based on a calculable feature. With the catalog sorted, an additional catalog is generated containing the first and last index numbers of each distance that occurs.

The remaining 6 columns provide a series of angles, calculated in pairs for subsets of 3 stars, each subset containing S0 and S1, and one of the remaining points. The angles listed describe the vertex angle between the 3 points, ∠ijk°, where Sj is the vertex point. Figure 3.16 below depicts this series of calculations.

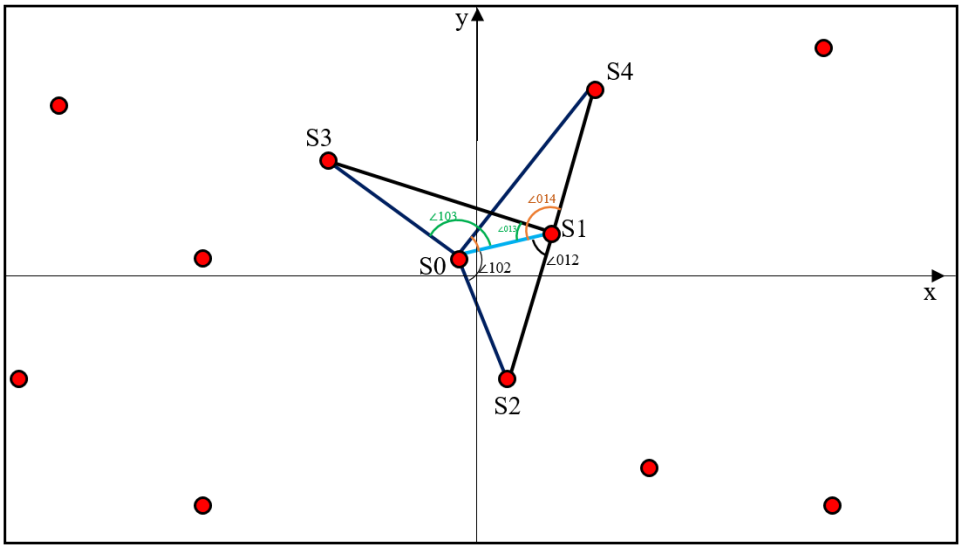

Figure 3.16 - Star Relationship Calculation Layout

The values listed in the relationship catalog provide 3 fully determined triangles, using one side length and 2 angles. [38] [39] [40]

The reason for using 3 triangles is that it provides redundancy, a single triangle may be falsely identified due to similar features between triangles in field, since the field is random it is possible that features are repeated, or some errors within the image, but with 3 unique triangles to identify simultaneously the likelihood of a false identification is greatly reduced. Having 3 triangles also produces 5 known points, these 5 points can all be used to calculate the location of the SS, providing redundant determinations to improve positioning precision.

Chapter 4 SOFTWARE DEVELOPMENT

Summary: This chapter covers the details of the key software systems developed, starting with the positioning system, which provides the absolute positing and attitude of the satellite simulator, then the path planning and tracking system, which is responsible for plotting and executing a desired trajectory.

4.1 Satellite Simulator Software

The software present on the SS to perform all operations was written in LabVIEW, from scratch, and does not make use of existing code. The software has a front panel on which the operator can observe general information as the SS operates, such as the position and attitude, and path trace, and to issue start and stop commands, as well as setting parameters for experiments.

The software begins by reading in the target satellite position and attitude which the operator has entered, and then initiates the path planning function to plot a trajectory. Following this initial setup phase the software then enters the main operations sequence.

In this main section of the software there are multiple parallel loops which perform different operations simultaneously to maximize efficiency. One loop is responsible for tracking the front panel parameters, and logging and displaying data throughout the experiment. Another loop runs the positioning system, allowing the SS to update measurements of its position and attitude as often as possible, operating at an average rate of 15Hz. The last major loop operates the path tracking and control systems. The path planning, positioning, and control portions of the software will be covered in more detail in the following sections.

4.2 Path Planning System

In order to perform actual RVD operations, the SS needs to be able to determine how to get from wherever it currently is to where its target is. To do this the SS knows its current position and attitude, as provided by the positioning system, and also knows the position and attitude of the target SS to dock with. The targets information is supplied by the operator who observes the position and attitude information for the docking target and manually enters it into the system. This is the only information given to the SS by the operator and replaces the need for a target sensing system or communications between the pair of SS. Both are possible to implement, however due to time constraint they were not.

The path planning is done in 3 separate phases and produces a series of waypoints. It is worth noting that the waypoints do not have a time requirement for execution, and that the target SS is free floating and performing station keeping maneuvers with a stable position and attitude at a known location. The path planning system on the chaser SS first

determines a straight line between its current location and the target SS location, knowing the current location of it and its target's centers. Along this line, waypoints are set every 0.01 meters, with the final waypoint in this group being placed a distance of 0.64 meters from the targets position. This distance ensures a safe clearance space between the chaser SS and the target regardless of orientation relative to one another. The system then determines the shortest path around a circle with a radius matching the current distance from the target center to align with the docking receiver. Again, waypoints are placed every 0.01 meters along this path until the point where it aligns with the docking receiver. The final stretch of the path is determined the same as the first, however now the current position at the end of the circular portion of the path means that a line connecting that point with the target's center now passes through the center of the docking receiver. The path is plotted until a distance of 0.47 meters from the target center. At this distance the docking receiver and probe are in contact.

The target attitude for the chaser is also specified at each waypoint in the path, however it is not currently used as a parameter for switching between waypoints. The SS can operate in 2 ways, either pointing along the path's current vector to the next waypoint, or maintaining a constant attitude throughout the path. In order to ensure that the system does actually dock at the end of the path, the SS must achieve the correct attitude to align the docking probe with the docking receiver on the target. The design of the docking probe and docking receiver places them on opposing faces on each of the SS bodies. In order to dock the probe into the receiver, the chaser SS must match the attitude of the target SS,

Figure 4.1 illustrates this relationship. This attitude target is given to the SS at the beginning of the path and will be achieved and maintained over the duration of the path.

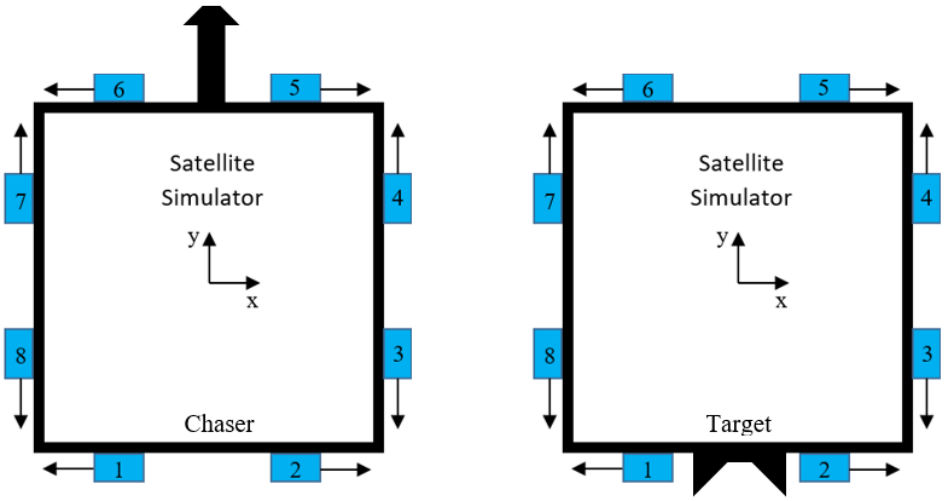

Figure 4.1 - Satellite Simulator Docking Probe and Receiver Mounting Orientations

4.3 Positioning System

The positioning system takes input from the IR camera onboard the SS which images the star field above it. This image data is used in conjunction with the star catalogs described in Chapter 3.4 to calculate the absolute position and attitude of the SS over the surface of the air bearing table. The positioning system here provides position information in terms of the X and Y coordinates relative to the granite surface, as well as the attitude of the satellite simulator. This positioning system does not provide spatial data in terms of orbital parameters or similar such terms related to actual satellite dynamics but is instead intended to facilitate testbed operations in terms of the planar system. The system provides a

measure of the absolute position of the SS which can be used for GNC as well as docking with another SS which is using the same positioning system.

4.3.1 Implementation

The first step in determining the position and attitude of the SS is to capture an image of the star field. This is done using a camera equipped with an 940nm band pass filter, mounted on top of the SS over the geometric center. The image is then processed through a threshold function which sets the brightness of each pixel to either minimum or maximum brightness. This process helps to eliminate noise and makes the actual stars much more prominent within the image. Figure 4.2, Figure 4.3, and Figure 4.4 show the same area of the star field at multiple stages of processing. Figure 4.2 shows the cameras view without the band pass filter installed, and Figure 4.3 is the same area with the filter installed. It is evident that the stars in the image have varying brightness, most notable that the stars get dimmer towards the edges of the image frame.

Figure 4.2 - Positioning System Image - Visible Spectrum

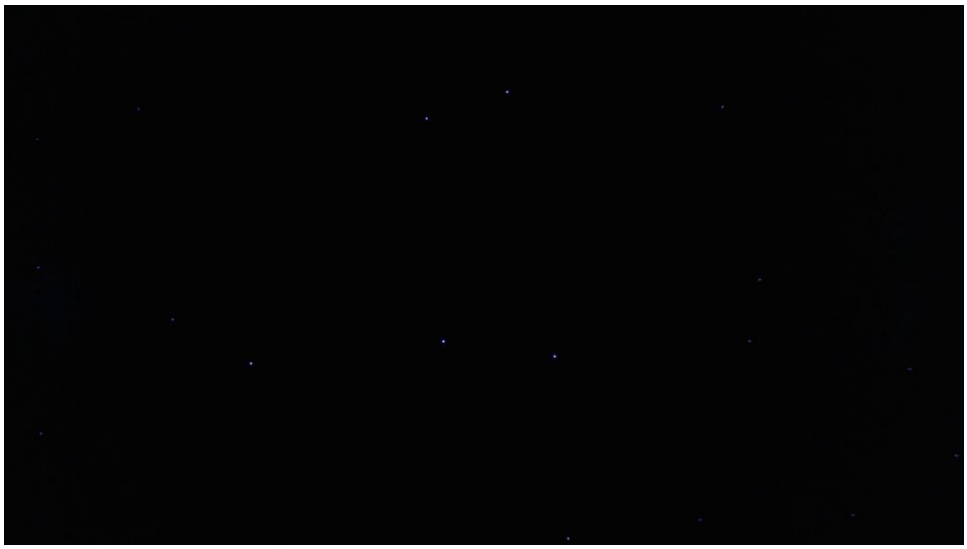

Figure 4.3 - Positioning System Image - IR Spectrum

Variances in brightness can be attributed in part to imperfections and manufacturing differences between individual LEDs, however that does not fully explain why the LEDs are perceived to grow dimmer as they approach the edges of the image.

This dimming is due to the light travelling through the filter at more of an angle as it approaches the edges, resulting in a longer path through the filter, and causing a slight shift in the wavelength of the light, bringing it away from the 940nm center frequency of the band pass filter. As the frequency shifts further from the center frequency it begins to be blocked by the filter, which has a very narrow pass band. Even though the intensities of stars near the edges of the image are lower than near the center, they are still detectable by the camera. The threshold process, Figure 4.4, brings all the intensities to the same value, making all stars in the image easily distinguishable.

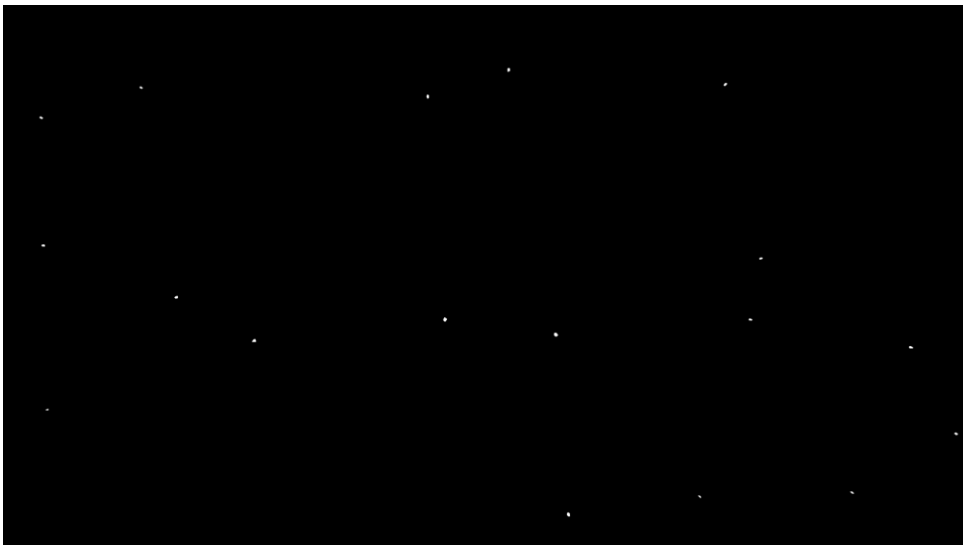

Figure 4.4 - Positioning System Image - IR Spectrum Threshold Applied

With the image in a usable format, the next step is to determine the location of the stars within the image. This is done using a built-in LabVIEW function called IMAQ_CountObjects2. The function performs edge detection around the bright pixels in the image and estimates the center location of each detected object. To avoid potential hot pixels being incorrectly detected as stars, the function requires the object occupy an area of at least 10 pixels.

The function returns an array containing an arbitrary index for the stars detected within the image based on the order they were detected in, along with the pixel coordinates of the center of the star, estimated with subpixel accuracy. The arbitrary index numbers and center locations as they are detected are shown in Figure 4.5 overlaid on the previous image after the threshold was applied.

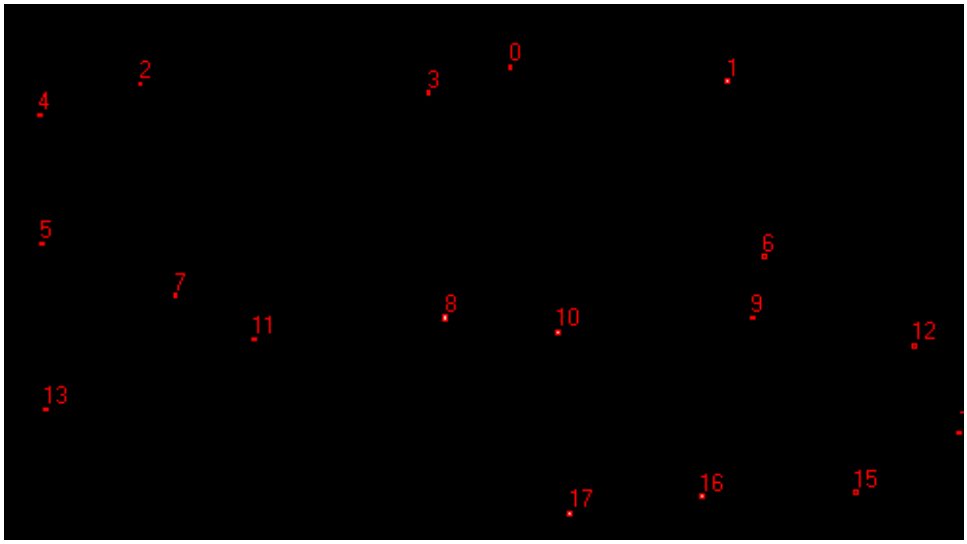

Figure 4.5 - Positioning System Image - Stars Located

In order to utilize the image information to calculate the SS location, the positioning system first must identify which specific stars are in view. The star field has been designed so that at any point over the surface of the granite table, there are a minimum of 5 stars in view. Using the relationship catalog, Table 3.3, the system begins by selecting a group of 5 of the arbitrarily numbered stars from the image. If there are only 5 stars in view, the system takes the star which is closest to the image center to be S0. If there are more than 5 stars in view, the system performs multiple determinations taking each of the stars in view to be S0 in turn, in order of the arbitrary number assigned to them, and the 4 closest stars to the current S0 for S1-S4.

To determine the 4 closest stars to the current S0, the system calculates the distance to every other star using the pixel coordinates of the center points. These distances are then sorted and the 4 closest points are assigned as S1-S4 in order of proximity to S0.

The shortest distance calculated, from S0 to S1, must be converted from units of pixels to meters to compare against the catalog value d01. This is done using a predetermined conversion ratio, Δ, (2).

$$\Delta = \frac{1}{n}\sum \frac{\sqrt{(X_i - X_j)^2 + (Y_i - Y_j)^2}[meters]}{\sqrt{(x_i - x_j)^2 + (y_i - y_j)^2}[pixel]} = 0.0013\,\frac{m}{pix} \qquad (2)$$

This conversion ratio was calculated by imaging and manually identifying points in the star field, calculating the physical distance between each pair of those points and calculating the same distance in the image and determining the ratio. This was repeated several times with different images to produce an average value of 0.0013 meters per pixel. Calculating the distance between S0 and S1 and converting to meters produces the calculated value of d01, (3).

$$d_{01} = \left(\sqrt{(x_0 - x_1)^2 + (y_0 - y_1)^2}\right) * \Delta\left[\frac{m}{pix}\right] \qquad (3)$$

Next the positioning system calculates the angles between the various 3-star subsets in the image using the [x, y] (pixel) coordinates. In (4), indices *i, j, k* denote the makeup of the triangle whose tangent is being calculated, where *j* is the vertex point where the angle is being calculated, and *i* and *k* are the other 2 points of the triangle. The calculations for the angles are independent of the units used to calculate them, so there is no conversion required between the image frame and the granite table frame.

$$\angle ijk° = \tan^{-1}\left(\frac{\|u \times v\|}{u \cdot v}\right) \quad (4)$$

$$u = [x_j - x_i, y_j - y_i, 0]$$

$$v = [x_j - x_k, y_j - y_k, 0]$$

With all the identifying parameters determined, the calculated values are now compared against the reference catalog. The positioning system makes use of another catalog containing the beginning and ending indexes of each distance that occurs within the relationship catalog. Using this, the system determines the range of relevant indexes to search within 5 cm of the calculated value of d01. Searching through a subset of the catalog with a range around the calculated distance allows the system to tolerate inaccuracies in the distance calculation that may arise from incorrect conversion from pixels to meters due to non flat areas of the marker array, since the markers are mounted on a flexible material, if a point lies out of the plane parallel to the granite table then the conversion will not be perfectly accurate for that distance. Another source of error in the calculation may come from warping caused by the camera, the image may be distorted by the lens. As the positioning system compares its value against each of the catalog entries, it calculates an error value for each, as in (5). If the total error calculated is less than 0.07 it is taken as a possible solution. The error for each value is calculated as a deviation from the catalog value in percentage, as in (6). Calculating the error in this way eliminates the scale

differences between meters and degrees. The total error threshold was chosen at 0.07 as it represents an average error across all calculated values of 1%.

$$error = err_{d01} + err_{\angle 102^\circ} + err_{\angle 012^\circ} + err_{\angle 103^\circ} + err_{\angle 013^\circ} + err_{\angle 104^\circ} + err_{\angle 014^\circ} \quad (5)$$

$$err_i = \left\| \frac{i_{calculated} - i_{catalog}}{i_{catalog}} \right\| \quad (6)$$

Each potential solution with a total error below the error threshold is added to a solution array which contains the arbitrary index numbers of the unknown stars, the determined ID numbers which map to them, and the total error associated with that determination. This process is repeated for each star within view as S0, producing multiple solutions from multiple sets of points within the image. The solution array is then sorted based on the error value for each determination. The arbitrary index numbers of the stars within the image are then mapped to the determined unique ID numbers based on the solutions with the lowest error first, until all stars are identified or there are no solutions remaining. In the event that there are no solutions within the error tolerance, the system does not proceed and instead takes another image and begins again.

This process reduces the chances of an incorrect mapping. Once all identified points are mapped the system is able to calculate the position and orientation of the SS.

The system calculates the position using trilateration. This method takes the known coordinates of 3 points, here being 3 of the stars located within the reference frame of the

granite table, and the distances from those points to an unknown point, the center of the SS. There are more than 3 known points, since the identification process requires a minimum of 5, so the system uses all unique subsets of 3 points from the identified points. This produces a number of solutions for the position of the satellite simulator, given as α in (7), where n is the number of identified points.

$$\alpha = \frac{n!}{3!\,(n-3)!} \tag{7}$$

The trilateration method to determine the coordinates of the SS center is performed by solving a system of equations, given below.

$$d_i^2 = (X - x_i)^2 + (Y - y_i)^2 = X^2 - 2Xx_i + x_i^2 + Y^2 - 2Yy_i + y_i^2 \tag{8}$$

Where d_i is the calculated distance from a particular star, i, which has been identified, to the unknown position of interest, the center of the SS. This distance is calculated using the pixel coordinates of the star as it has been imaged, and the center pixel location of the image, and converted to meters using Δ, as determined in (2). The image center is used as the camera is mounted over the geometric center of the satellite simulator, it is assumed that the center of the image therefore represents the center of the satellite simulator.

The coordinates of the particular star are given as $[x_i, y_i]$ in the granite table reference frame.

The coordinates [X, Y] are the coordinates of the SS center that are to be calculated.

The value of i = 1, 2, 3 denotes each of the 3 stars in the selected subset.

First, subtracting d_1 from d_2, and simplifying the equation;

$$d_1^2 - d_2^2 = x_1^2 + y_1^2 - x_2^2 - y_2^2 + X(2x_2 - 2x_1) + Y(2y_2 - 2y_1) \quad (9)$$

$$XA + YB = C \quad (10)$$

$$A = 2x_2 - 2x_1$$

$$B = 2y_2 - 2y_1$$

$$C = d_1^2 - d_2^2 - x_1^2 - y_1^2 + x_2^2 + y_2^2$$

Similarly, subtracting d_2 from d_3:

$$d_2^2 - d_3^2 = x_2^2 + y_2^2 - x_3^2 - y_3^2 + X(2x_3 - 2x_2) + Y(2y_3 - 2y_2) \quad (11)$$

$$XD + YE = F \quad (12)$$

$$D = 2x_3 - 2x_2$$

$$E = 2y_3 - 2y_2$$

$$F = d_2^2 - d_3^2 - x_2^2 - y_2^2 + x_3^2 + y_3^2$$

Now solving (10) and (12) for X and Y:

$$X = \frac{C}{A} - \frac{YB}{A} = \frac{F}{D} - \frac{YE}{D} \tag{13}$$

$$0 = \frac{C}{A} - \frac{F}{D} + Y\left(\frac{E}{D} - \frac{B}{A}\right)$$

$$Y = \frac{FA - CD}{AE - BD} \tag{14}$$

$$Y = \frac{C}{B} - \frac{XA}{B} = \frac{F}{E} - \frac{XD}{E} \tag{15}$$

$$0 = \frac{C}{B} - \frac{F}{E} + X\left(\frac{D}{E} - \frac{A}{B}\right)$$

$$X = \frac{BF - CE}{BD - AE} \tag{16}$$

The solution for the location of the center of the SS in the granite table reference frame is given by equation (14) and (16). The multiple solutions for each subset of 3 stars from all the identified stars are sorted from minimum to maximum, the upper and lower 20% of the solutions are removed to help eliminate outliers. The choice to perform this operation as a percentage rather than a fixed value allows the system to easily adapt to the varying number

of solutions. 20% was chosen to remove a number of solutions without significantly impacting the number of solutions left. For a set of 5 identified points, the minimum number, there would be a total of 10 solutions for the position. After removing the upper and lower bounds of the solution set there would still be 6 solutions left to work with.

The remaining solutions for X and Y are passed through a median filter before being averaged together to produce a single solution for X and Y. The positioning system then makes use of a 4-point moving average filter, considering this updated position and 3 previous solutions. This moving average filter minimizes the effects of noise and outliers on the system.

Similarly, the attitude of the SS can be calculated using information about the identified stars in both the image frame and in the granite table reference frame. The system selects 2 of the identified stars in the image to use, the pixel coordinates of these points are then used to calculate the angle the vector between them makes with the x-axis of the image. The same calculation is performed for the same pair of points using the coordinates in the granite table reference frame. Since the camera is fixed to the SS, the reference frame of the image is free to rotate with the SS. The difference in the 2 calculated angles is equal to the rotation of the SS relative to the stationary reference frame of the granite table, (17).

$$\theta = \tan^{-1}\left(\frac{y_2 - y_1}{x_2 - x_1}\right) - \tan^{-1}\left(\frac{Y_2 - Y_1}{X_2 - X_1}\right) \quad (17)$$

The attitude is calculated for each unique pair of points from the set of identified points, the total number of attitude solutions is given as β, (18).

$$\beta = \frac{n!}{2!\,(n-2)!} \tag{18}$$

The multiple solutions are processed the same as the position solutions, with outliers being removed and the remaining solutions being averaged.

The attitude positioning also makes use of the FOG onboard. Once the absolute attitude is determine using the camera system it is propagated using the FOG for 50 samples, or approximately 2.5 seconds. After the 50 samples the attitude is update from the camera system. These updates prevent drift from accumulating, since the FOG sense the angular rate and not the actual angle, it is possible that over time the propagated value will be noticeably off from what the actual value is.

4.4 Control System

The control system is responsible for achieving and maintaining the desired position and orientation of the satellite simulator. This is done using a PD controller. The control system follows the path designed by the path planning system, which is a series of waypoints. The control system is split into 3 separate PD controllers, one for the x, y, and θ positions of the satellite simulator. The system takes the desired waypoint position, and the desired attitude, and calculates the difference from the satellite simulators current position and attitude. In order to simplify the controller design, the system calculates this difference relative to a body fixed coordinate system, relative to the center of the satellite simulator instead of the granite table reference frame. This allows the system to easily isolate the X

and Y dimensions, which is useful since the thrusters, which are the actuators, are mounted along the X and Y dimensions of the satellite simulator. The difference with the desired X, Y, and θ is calculated, this is referred to as the positioning error. This error is used by the PD controller to produce the necessary outputs to drive the system towards the desired state. The control function for a PD controller is given in (19) where u is the control output, K represents the gain, e is the error, and $\dot{e}$ is the derivative of the error. The terms p and d denote the proportional and derivative components of the equation.

$$u = K_p e + K_d \dot{e} \tag{19}$$

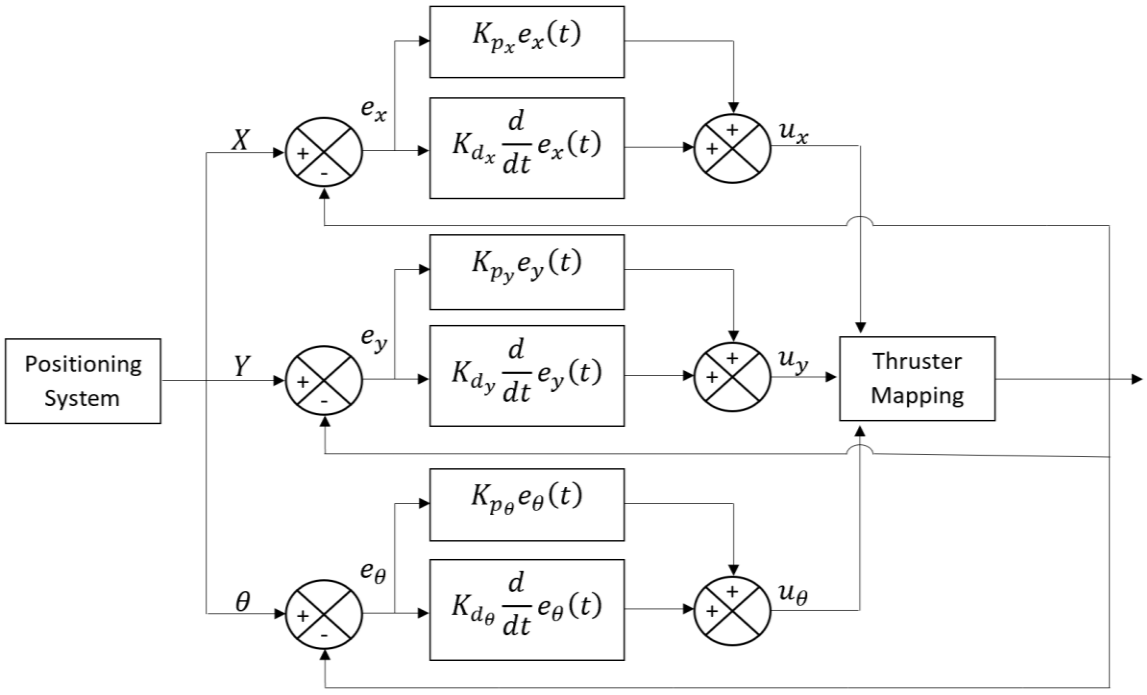

Figure 4.6 - Multiple PD Controller Layout

As there are 3 errors which are calculated, there are 3 control outputs produced. The X and Y control outputs map directly to the X and Y oriented thrusters, respectively, however the θ control output maps to both the X and Y oriented thrusters. To provide a rotational force

to control θ, the satellite simulator can fire the even numbered thrusters to rotate clockwise, or the odd numbered thrusters to rotate counter clockwise. The objective is to control each of the 3 degrees of freedom of the satellite simulator simultaneously, this requires that the control outputs be mapped to the appropriate thrusters. To simplify this mapping, each pair of thrusters per face is treated as a single thruster with a positive and negative output. (20) outlines the mapping procedure of each control output to the paired thruster, and the matrix inverse is taken as the pseudoinverse. [41] [42]

$$\begin{bmatrix} t_{12} \\ t_{34} \\ t_{56} \\ t_{78} \end{bmatrix} = \begin{bmatrix} 1 & 0 & -1 & 0 \\ 0 & 1 & 0 & -1 \\ -1 & -1 & -1 & -1 \end{bmatrix}^{-1} \times \begin{bmatrix} u_x \\ u_y \\ u_\theta \end{bmatrix} \qquad (20)$$

The system then takes the mapped output and determines which of the 2 thrusters to command. This is done by determining if the control value is positive or negative, a positive value will command the positive thruster, and a negative control value will command the negative thruster. Observing the mapping matrix in (20), each of the rows contains the contributions of each thruster to the control of each of the 3 degrees of freedom. The first row contains the X contributions, as can be seen on t_{12} and t_{56} contribute output in the X dimension. The reason for the -1 term is that t_{56} has its thrusters mounted in reverse order relative to t_{12}, this -1 reverses the logical output of the thruster and allows the same logical check that is used on t_{12} to be applied. This choice was made to simplify the software.

The mapping also serves to combine the 3 control outputs into a single control value for each thruster. The X and Y controls are independent, hence the 0 values in the mapping matrix, however the θ control value is present in every thruster.

The PD controllers each output a control value between -1 and 1. The thrusters are only capable of digital operation, meaning that they are only on or off. In order to achieve the output desired by the control system the thrusters are operated using Pulse Width Modulation. The control loop operates over a period of 50ms, the mapped thruster output is set to a percentage of this time period. Operating at 100% thruster output for a fraction of the time period provides comparable output to operating at the desired percentage output over the same period of time. Through experimental testing this control system has been confirmed to function with minimal deviation from the planned path and corrects itself when necessary.

Chapter 5 EXPERIMENTAL RESULTS

Summary: This chapter focuses on the various experiments performed using the satellite simulators at various stages in development. These experiments outline the various tests done to validate the performance and operability of the satellite simulators, and to prove the final functional state for docking operations.

5.1 Gas Thruster Calibration

In order for the SS to be able to control their position and orientation, the thrusters are required to be accurately calibrated. This calibration ensures that the output force for each thruster is equivalent, making the SS easier to control. While it would be possible to design a controller which could compensate for different outputs of each thruster, it is more reasonable to set all outputs to be equal to simplify the controller design. Given the nature of the SS system, it is not necessary to have a high output thrust, therefore the actual output force is not the concern here, but rather that the output forces are all equal.

As can be seen in Figure 5.1, the SS is a square platform with 2 thrusters mounted facing opposite directions on each face, for a total of 8 thrusters pointing in 4 directions. With this configuration it is possible for the SS to travel in a straight line by firing 2 thrusters in the

same direction, or to perform a rotational maneuver by firing alternating thrusters on each face to rotate either clockwise or counter-clockwise. The output pressure for the thrusters is set to 0.4 MPa. This pressure was selected to be within the pressure limits of the airline tubing used and to prevent the airlines from leaking. The lines are connected using quick connect fittings, it was found through testing that at pressures below 0.3 MPa the fittings would not make a proper seal and would leak, and that above 0.6 MPa the fittings and some of the seals on the thruster valves began leaking. The thrusters themselves are rated up to 0.8 MPa, so leaks beginning at 0.6 MPa indicate that the internal seals are degrading.

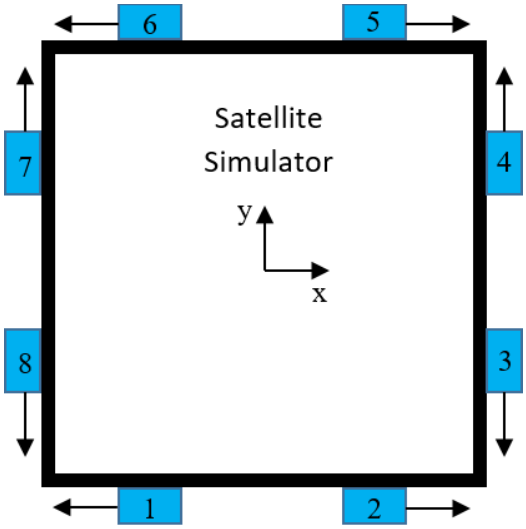

Figure 5.1 - Satellite Simulator Thruster Mounting Diagram.
Thruster locations are marked in blue. Arrows show direction of thruster gas output.

In order to measure the output force of each thruster, a digital force sensor with a magnetic mounting plate was used. The force sensor was attached to a PC to collect data, and is capable of resolving forces with an accuracy of 0.001 N. This high accuracy is required as the output force of each thruster is quite small.

The thrusters themselves consist of a housing, which contains the solenoid to actuate the valve state either open or closed, a setscrew to adjust the inlet air flow, and an ejector nozzle. By adjusting the setscrew, the inlet air flow can either be increased or restricted, which adjusts the output force of the thruster. The thruster is connected to the air and power supplies with extra lengths of tubing and wire to minimize tension forces acting on the thruster.

The sensor is placed on a level surface, here using the air bearing platform. The sensor is oriented vertically, with the magnetic mount on top. The thruster is then mounted on the magnetic plate with the output oriented to either push or pull against the sensor. Either orientation will provide the same magnitude of the measurement with reversed signs. As the thrusters require both power and air lines to be connected in order to operate, extra lengths of both were used to minimize tension forces acting on the thruster. With the thruster mounted on the sensor in this orientation the force of gravity acts along the axis on the sensor, this results in a constant force being measured due to the weight of the thruster. To account for this the sensor is zeroed before taking measurements, where the observed change in force is due only to the thruster output.

Measurements were taken with a sampling rate of 200 samples per second for a 10 second duration. The first 1-3 seconds of data collection is done with the thruster off to get a measurement of the zeroing error and system noise. When the thruster is switched on there is a spike in the measured force, this is the result of the solenoid actuating, so this region of the data set is ignored. The remainder of the collected data represents the steady output

of the thruster. Figure 5.2 shows an example collected data set for a single thruster. The data for the on and off states of the thruster are averaged to reduce the effects of noise and the vibrations in the system due to the air flow through the thruster, and the off state value is subtracted from the on state value. This provides an accurate determination of the steady state output characteristics of the thruster.

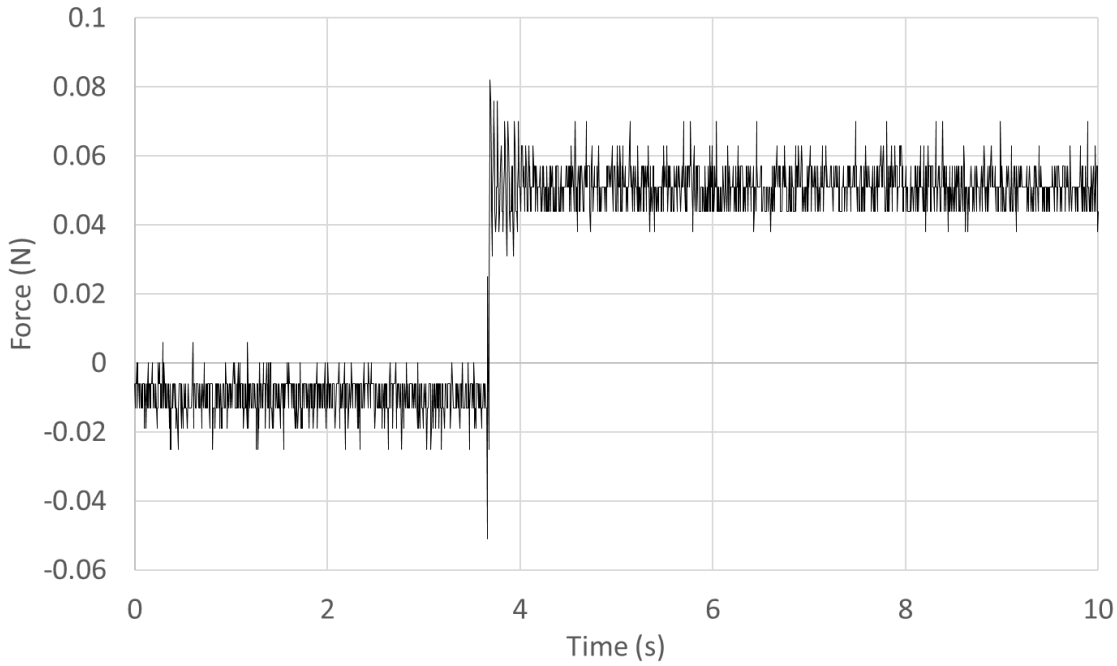

Figure 5.2 - Thruster Force Output Data Sample

In order to calibrate each thruster, the performance envelope for each is determined first. This is done by measuring the output force with the setscrew fully open and fully restricted. It was found that the output envelopes for all 16 thrusters (8 for each of the 2 SS) overlapped at 0.065 N. To set each thruster to this output, each was again mounted on the pressure sensor and the above method was repeated while varying the setscrew position until an output force of 0.065 N was achieved. Table 5.1 depicts the final set of measured values for the 8 thrusters of each SS.

Table 5.1 - Final Thruster Calibration Results for a Satellite Simulator.

Thruster	**Force Measurements**		
	On State (N)	***Off State (N)***	***Force Output (N)***
1	0.065	0	0.065
2	0.074	0.009	0.065
3	0.060	-0.005	0.065
4	0.068	0.003	0.065
5	0.066	0.001	0.065
6	0.073	0.008	0.065
7	0.065	0	0.065
8	0.067	0.002	0.065

5.2 Positioning System Calibration

To determine the performance of the positioning system the noise in the system must be characterized. This noise determines the overall precision of the positioning system as measurements cannot be made within the noise floor of the system. As was mentioned in section 4.3.1, the system makes use of a moving average filter which takes into account the current measurement as well as the previous 3. This is done as the positioning system operates sufficiently fast enough that the latency introduced by this filtering does not impact the SS performance, and it reduces the effects of noise in the calculated position. The noise in this system was measured by leaving the SS stationary with the air bearing disabled to prevent movement and recording the position multiple times.

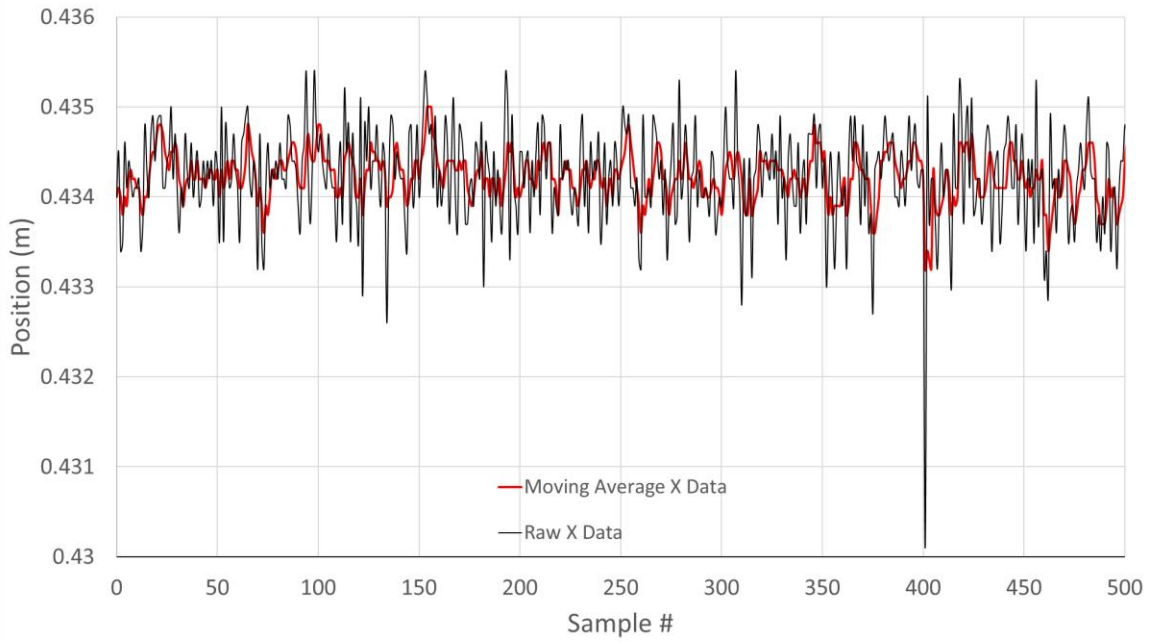

Figure 5.3 - Positioning System X Determination Noise

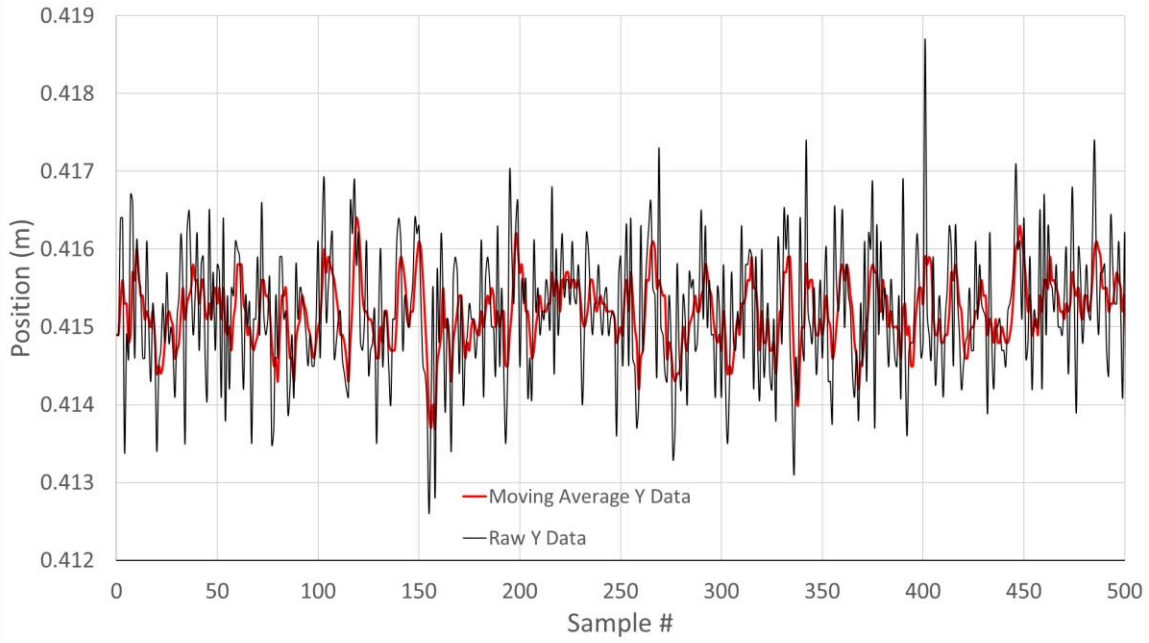

Figure 5.4 - Positioning System Y Determination Noise

Figure 5.3 and Figure 5.4 show the effects of the moving average filter as it is applied to the solution for the coordinates of the SS. The black trace is the unfiltered coordinate, while the red trace is the filtered. As can be seen, the filtered coordinates, shown in red, have less noise than the raw values. The filter also mitigates the effects of poor calculations, as can be seen from the occasional large spikes produced by errors in the calculations, likely resulting from a low quality image. The noise in the system causes the calculated position to fluctuate by about 1 millimeter, therefore the positioning system has an accuracy of ±1 millimeter. This is more than sufficient for the operations performed in this lab.

The standard deviation of the X measurement series is 0.26 mm, while the standard deviation of the Y measurement series is 0.43 mm. This suggests that the X measurement is higher quality than the Y measurement. This makes sense as the camera used here uses a 1920 X 1080 pixel sensor, with the X axis having 1920 pixels, and 1080 pixels on the Y axis. This increased resolution on in the X dimension of almost 50% from the Y dimension explains why the standard deviation of the X measurement is almost 50% of the Y measurement.

The noise within the attitude determination system was determined as well, given in Figure 5.5. Again, the black trace is the unfiltered attitude, while the red is the attitude from the moving average filter with 4 elements.

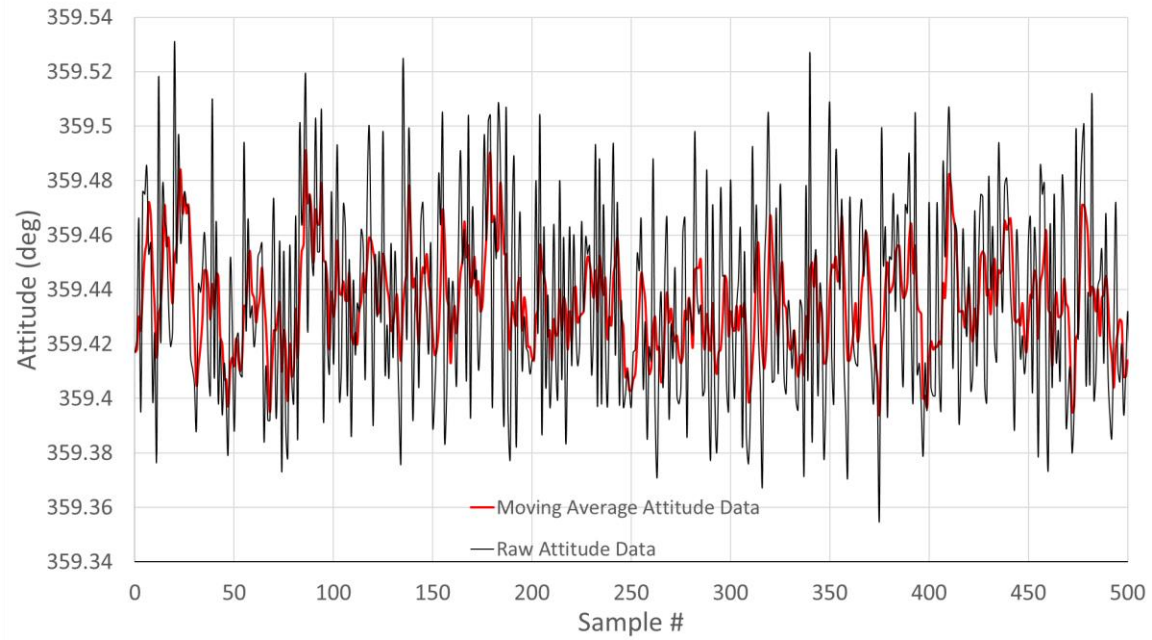

Figure 5.5 - Positioning System Attitude Determination Noise

It can be seen that the accuracy of the attitude determination with the moving average filter is approximately ± 0.05°, with a standard deviation of ±0.017°.

As was mentioned previously in Section 4.3.1, the attitude positioning is also done using the FOG. The absolute attitude from the star camera system is propagated for 2.5 seconds using the FOG to improve the stability of the attitude measurement. The noise in the FOG is also determined, shown in Figure 5.6.

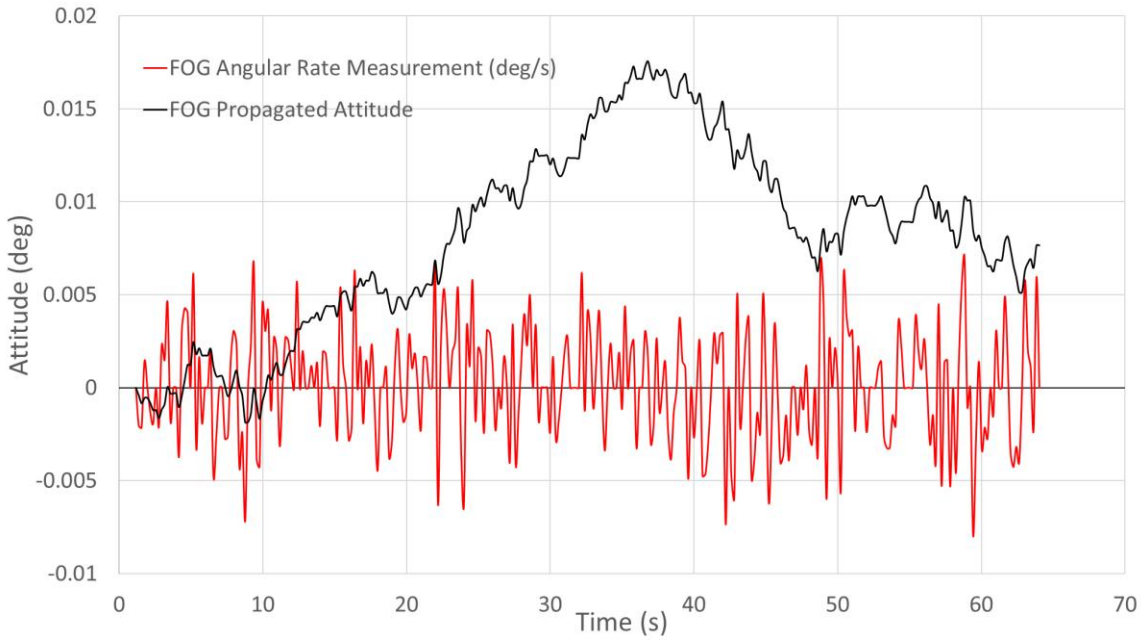

Figure 5.6 - FOG Attitude Noise

The red trace shows the angular rate which is directly measured by the FOG, while the black trace shows the attitude which is propagated from that detected rate. It is easy to see that while the FOG has a very low noise floor, about ±0.007°/s, over time this noise can accumulate noticeable drift. After about 35 seconds the attitude had drifted by almost 0.02 degrees, and while this is small it is important to note that this drift is random. Over the entire 64 second data set shown, the total attitude drift, ignoring signed values, is 0.14°, which is significant. From this trend it is possible to estimate that over the 2.5 second duration when the system is propagating using the FOG between updates from the camera system, the drift which can be expected is approximately 0.005°, which is within the accuracy of the camera system so it is acceptable. However, given that this drift is random, and has only been characterized on a stable, stationary system it may fluctuate for the various states of the SS. To combat this, the system considers any velocity measured by the FOG below 0.01°/s to be 0°/s. This minimum rate is acceptable as it is slightly above

the noise floor, and measurements within the noise floor of the sensor cannot be considered to be useful. With this minimum angular rate set, over the propagation time it is possible for the satellite to drift 0.025° without being detected by the FOG, however the update from the star camera system will be able to detect and correct this drift as it accumulates.

It is worth noting that this positioning system is susceptible to errors due to distortions in the image taken. It is possible that the image taken is corrupted, contains errors, or is otherwise distorted. Corruption and errors can occur in individual frames due to communication errors between the PC and camera, lag or timing issues, or some other issue within the camera itself. The errors that may occur due to the hardware and computer are unavoidable without changing hardware, however there is no guarantee that that will be error free. The other source of error in the images is due to the motion of the SS.

Since the camera used is mounted to the SS which is in motion, it is possible that the image captured is distorted due to the camera moving, causing the points within the image to streak. Given the low translational velocity of the SS, about 1-2 cm/s, the effects of this motion on the image are negligible, as will be seen in the results obtained in Section 5.4. The effects of the rotational motion of the SS are not negligible, however. Since the rotation speed of the SS can be much higher, 5 – 10°/s, the distortion in the image can cause errors. This causes large "jumps" in the position and attitude measurement of the system, however, as can be seen in the results section of this thesis these errors do not make a significant impact on the performance of the SS systems, and do not occur frequently.

The operations performed in this lab require 2 SS systems, each requires its own positioning system. While the performance between the 2 systems is the same, given that they are using the same hardware and same software, the positions calculated between them are not the same. Placing both SS in the same physical space on the granite table, in multiple points on the granite table in multiple orientations yielded an interesting result. The target SS would calculate the same attitude as the chaser SS, but the X and Y positions of the chaser would be translated by +2.1 cm. The reasoning for this is most likely that because the cameras used are consumer grade, and the sensors within them are not necessarily identical, or placed in exactly the same spot within the housing. Given that the offset is the same regardless of the orientation means that the offset can be adjusted for in software, or by adjusting the camera position on the SS. The mounting points on the top of the SS are spaced in 2 cm increments, so moving the camera to account for this is trivial. The additional 1 mm offset is small enough to be considered negligible as it has no impact on the docking performance of the system.

5.3 Attitude Control

The attitude control system is one of the most critical in a docking scenario, which ensures that the SS can achieve and maintain the correct attitude while it is maneuvering. If the system is unable to maintain the attitude of the SS, then during the docking procedure the docking probe will not align with the receiver and the docking attempt will fail. The actuators available to this system are the onboard reaction wheel, and the gas thrusters. The performance of both actuators was tested to determine a viable control system.

5.3.1 Reaction Wheel

The attitude control was first tested with the reaction wheel. The reaction wheel onboard is a Sinclair RW-0.01 capable of outputting a nominal torque of 0.01 Nm. The communications with this actuator is done using an RS232 converter connected to the OBC via USB. The wheel is capable of operating in a number of control modes, including speed, acceleration, torque, and momentum. In this implementation acceleration control is used, however any of the control modes could be used to create a viable controller.

This particular implementation of the reaction wheel is only capable of operating with open loop control, meaning that there is no feedback from the reaction wheel available to the control system. Without feedback it is impossible to determine the current state of the reaction wheel directly, and the control loop cannot be closed. Open loop control is generally inaccurate since the controller is unable to correct itself or account for disturbances to the system. In order to provide feedback to the controller, the onboard positioning system is used. The PD controller implemented to drive the reaction wheel takes in the current attitude of the SS as the process variable, and the desired attitude as the state variable. As the SS is moved by the reaction wheel the current attitude moves towards the desired state, and through proper tuning of the PD controller it is able to accurately reach and maintain the attitude of the SS, Figure 5.7 shows a variety of attitude maneuvers performed using the reaction wheel.

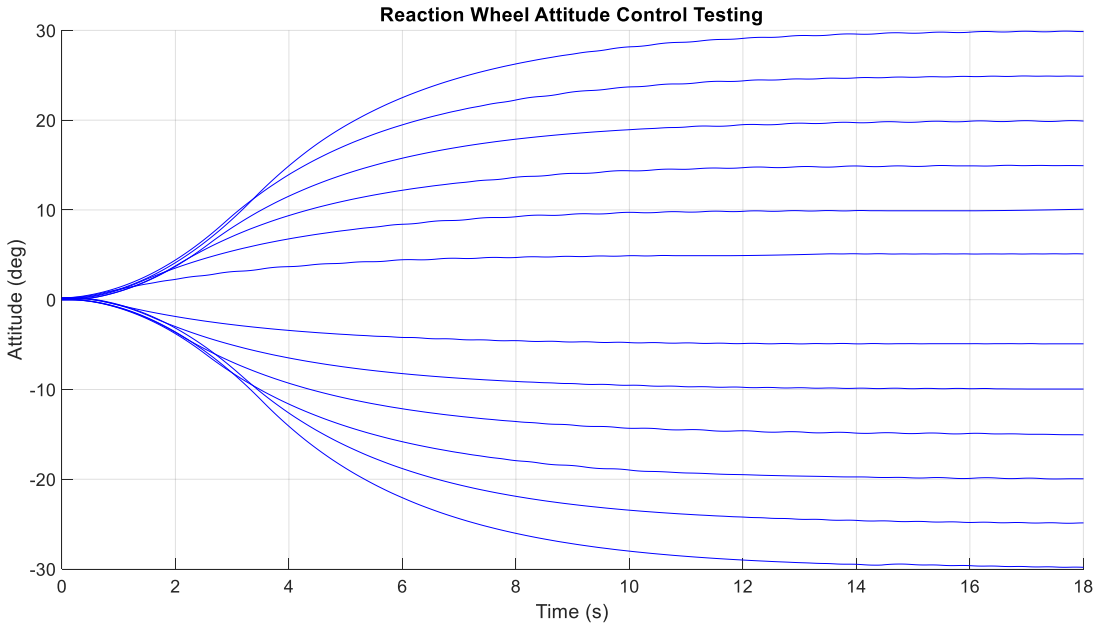

Figure 5.7 - Attitude Control Tests Using Reaction Wheel

It is easy to see from Figure 5.7 that the reaction wheel is capable of maneuvers in both the clockwise and counter clockwise directions, at a variety of angles, and maintaining those angles once they are reached with minimal deviation. For small angular maneuvers, 5°-10° the system achieves a steady state after 10-12 seconds, for larger maneuvers, 25°-30°, it takes 16-18 seconds to achieve a steady state.

The precision of the controller here is limited by the precision and stability of the attitude determination system. To account for noise within the positioning systems attitude determination, the attitude controller considers an angular difference of ±0.1° of the target angle as a 0° difference. This reduces control fluctuations and over activity in the controller induced by sensor noise. By observing the collected data from the maneuvers performed using this control system, the attitude fluctuates by ±0.05° about the target boundary.

Therefore the precision of this implementation of an attitude control system using the reaction wheel is ±0.15°.

One of the main issues with operating the attitude controller using the reaction wheel is the lack of feedback from the wheel itself. Having feedback from the wheel would enable the SS to monitor and adjust the reaction wheels' operations and to perform tasks such as de-spinning the wheel to prevent it from overspinning. The wheel over spins when it attempts to operate outside of its control range, which is either limited by the current or velocity of the wheel. When over spin occurs, the wheel stops accepting commands from the OBC and the wheel spins freely, only experiencing friction from its bearings and drag from the air. The reaction wheel contains very high quality bearings that are extremely efficient, meaning they impart little friction on the system. This is essential for a reaction wheel as a friction forces within the wheel would impart another torque on the system, as well as increasing the required energy to drive the wheel. When the wheel stops receiving commands it begins to spin freely near the maximum speed of the wheel, from this state it takes several minutes for it to stop spinning on its own. During this time the SS does not have any control over its attitude and all momentum stored within the reaction wheel will impart an increasing rotational rate on the SS as the wheel rate slows, and without feedback from the reaction wheel it is not possible to sense the operational state of the wheel.

De-spinning the wheel involves reducing or stopping the wheel's rotation and compensating for this change in momentum using an alternate actuator, such as the gas thrusters to maintain the SS attitude during the process. The reaction wheel can encounter

over spin if the controller tries to sustain constant acceleration for too long, or if over the course of operations, the total speed accumulated by the wheel exceeds the maximum allowable speed. The reaction wheel will also attempt to compensate for other torques acting on the SS, such as torques introduced by the gas thrusters firing, aberrant air currents within the laboratory, or the SS encountering debris on the surface of the granite table causing it to rotate. During testing it was observed that for angular maneuvers larger than 25°-30° this PD controller begins to cause the reaction wheel to over spin. At these angles it was possible to perform maneuvers, as can be seen in the data collected previously, however during testing over spin did begin to occur at these angles, and past 30° it would occur constantly. As the controller operates the reaction wheel in acceleration mode, the initial phase of the maneuver involves accelerating the wheel, while the final phase involves decelerating the wheel. During the maneuver however the velocity of the wheel is constantly changing, and during a large maneuver the acceleration phase is sufficiently long to try to accelerate the wheel past the maximum it is capable of, or the acceleration curve is too steep for the current limits of the reaction wheel. Without feedback it is difficult to determine which specifically is the cause, however both are equally likely.

This could be solved by performing large attitude maneuvers in small increments, however it would greatly increase the maneuver time. Figure 5.8 below outlines a maneuver for an 80° rotation in multiple stages with varying step sizes. While this maneuver is successful, it takes about 95 seconds to complete.

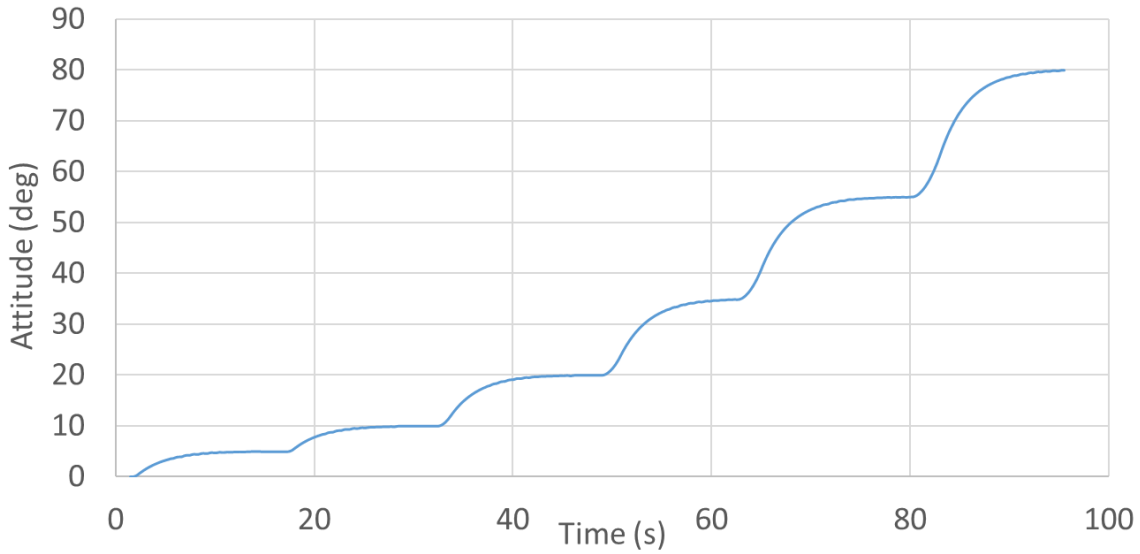

Figure 5.8 - Reaction Wheel 80 Degree Maneuver

5.3.2 Gas Thrusters

The alternative actuator onboard the SS is the series of gas thrusters. These gas thrusters were described previously in Section 5.1, and are capable of outputting a constant force of 0.065N. The controller for the thrusters is fundamentally the same and for the reaction wheel with a difference in the final tuned gains for the PD controller. To compare the behaviour of the attitude control system implemented with the thrusters against the reaction wheel, the same angular maneuvers were performed, and are shown in Figure 5.9. The blue plots are the maneuvers performed using the reaction wheel, the same as in Figure 5.7, while the red plots show the same maneuvers performed using the gas thrusters as the actuator.

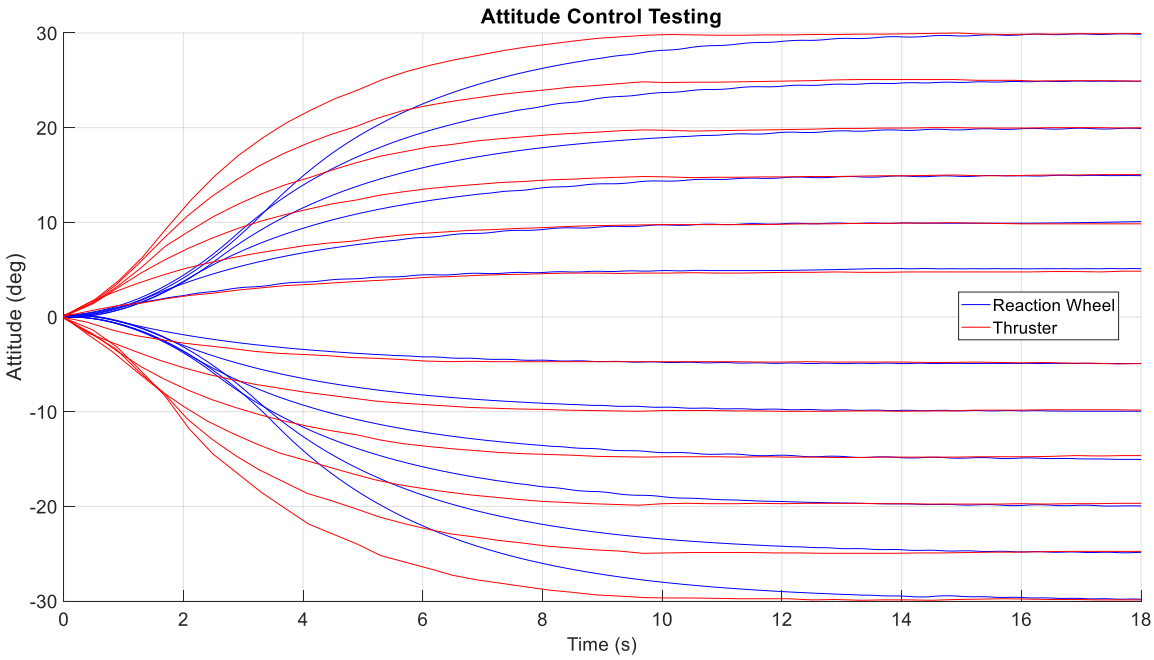

Figure 5.9 - Attitude Control Actuator Comparison

Observing the plotted data, it is clear that the gas thrusters are capable of a faster response overall. At small angles, such as the 5° maneuver, the performance between the different actuators is quite close, however as the angular maneuvering distance increases the thrusters are consistently able to achieve the target angle and stabilize faster. Over the range of maneuvers shown, the time it takes the thrusters to achieve the desired state is 8-10 seconds. The thruster implementation also achieves the same precision as the reaction wheel implementation at ±0.15° of the target attitude.

The performance of the thruster attitude control for large attitude maneuvers is shown in Figure 5.10, Figure 5.11, and Figure 5.12.

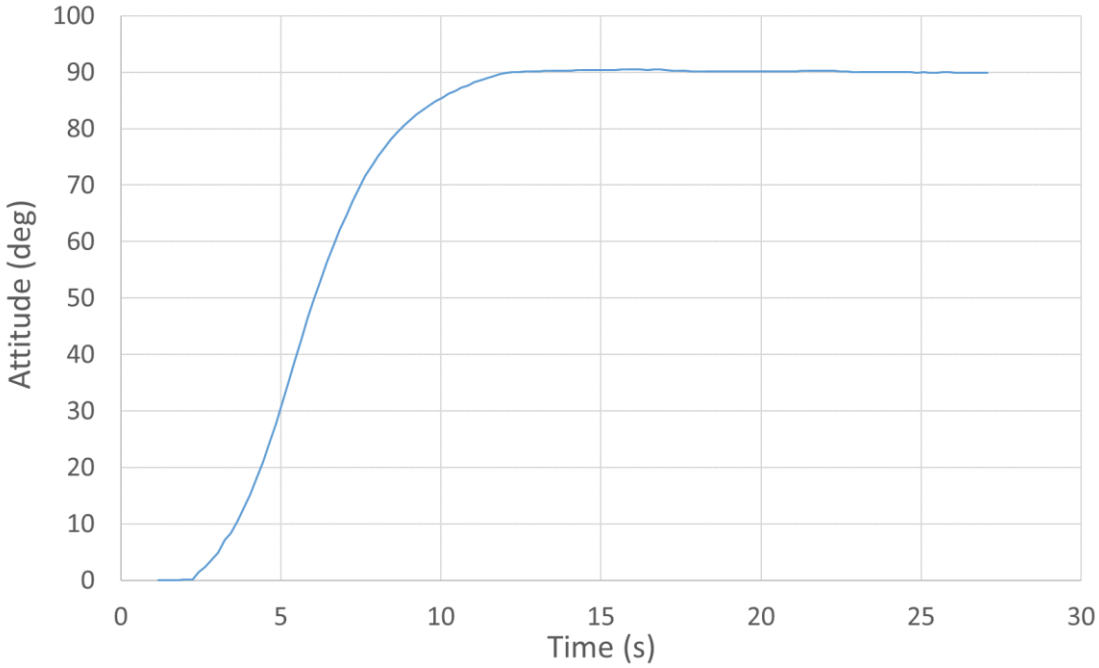

Figure 5.10 - Thruster 90 Degree Attitude Maneuver

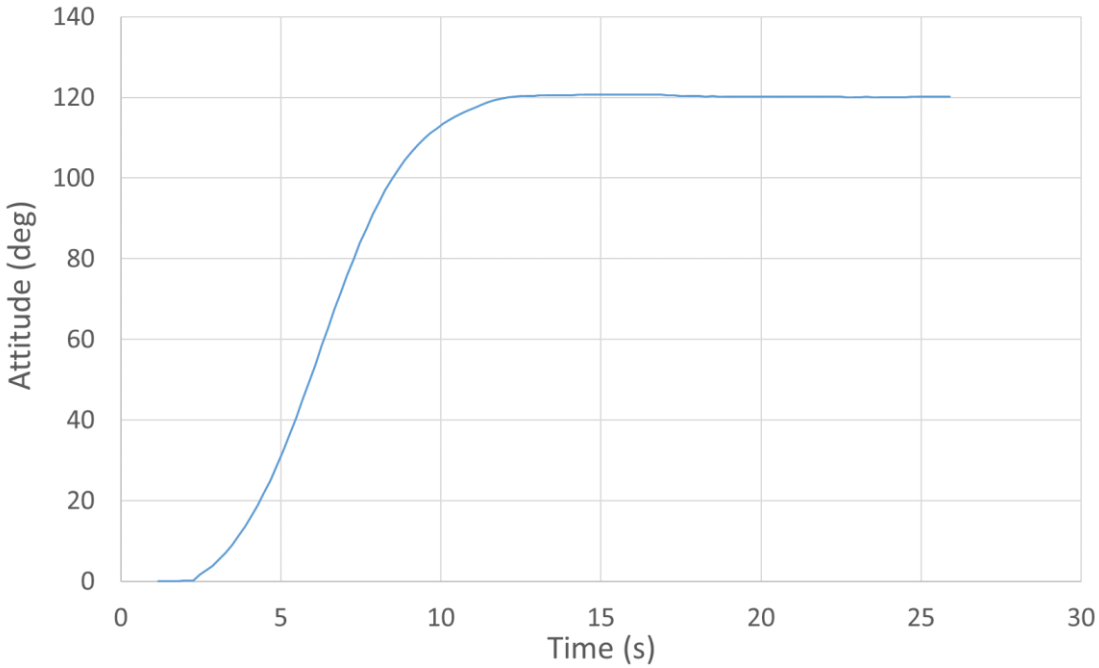

Figure 5.11 - Thruster 120 Degree Attitude Maneuver

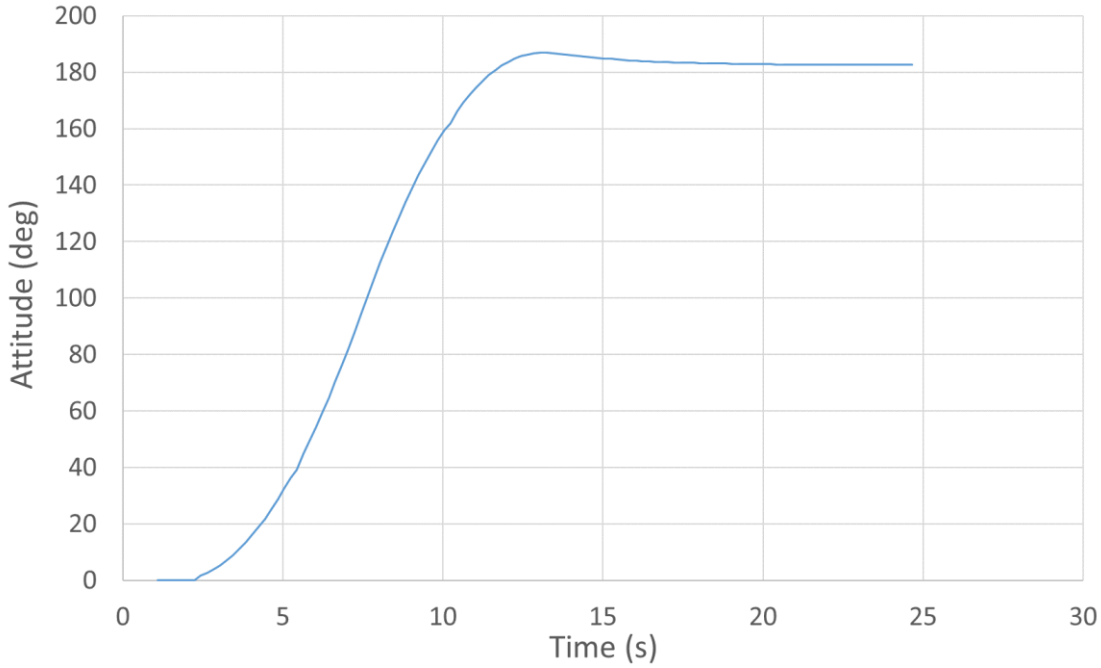

Figure 5.12 - Thruster 180 Degree Attitude Maneuver

The attitude controller implemented using the gas thrusters is able to handle a very large range of attitude maneuvers, with minimal overshoot. For the 90° and 120° maneuvers the system operates with overshoot well under 1°, and at 180° the overshoot is 6°. For the 90° and 120° maneuvers, it takes about 10 seconds from the start of the maneuver to achieve steady state at the target angle, while the 180° maneuver takes about 13 seconds.

Comparing this against the attitude controller implemented with the reaction wheel, the thrusters clearly have better performance and comparable accuracy.

5.4 Path Following

The SS performs operations by following a set path defined by a series of waypoints. This series of waypoints is either predetermined and given to the SS, or is calculated by the SS before beginning operations, as is done for docking operations. The SS is not able to

navigate without a waypoint to navigate to, if the current waypoint is the same as the current position, the system will be performing station keeping by maintaining that position. As was noted in 4.2, the waypoints do not have a time requirement for execution, and therefore are executed as quickly as possible.

All test paths shown in this section begin at the center of the granite surface, coordinates [2, 1], and proceed initially in the +Y direction. This starting location was chosen to allow the experiments to be recorded using a wall mounted camera, which is fixed and focused at the center of the granite table, and paths are designed to keep the SS well within the field of view of the camera. The location that the paths are set at has no influence on the performance of the SS.

Initial path following testing was performed in order to tune the PD control system. This test path was comprised of a figure eight curve, which was predetermined and loaded onto the SS. As the SS navigates through the waypoints, the path following system tracks the distance between the center of the SS and the current waypoint. When the SS is a distance of 0.02m away from the current waypoint, the system switches to the next waypoint in the series. This allows the SS to traverse the path using a PD controller without attempting to stop at each waypoint, since the desired state is to be at the location of the waypoint with a 0 velocity. This switching threshold value was determined experimentally, smaller values cause the system to slow down too much, which increases the time required to maneuver, while larger values cause the system to deviate from the path since the error remains consistently large.

The waypoint switching events are easy to see in the error graphs below, such as Figure 5.16, where there are frequent jumps in the error throughout. It is also worth noting that, observing the error graphs, the error for either X or Y may exceed 0.02m. the switching case is for a distance of 0.02m from the next waypoint, this distance is calculated using both the X and Y positions, so individual errors in X and Y may be larger or smaller. The error shown in these graphs represents the difference between the current state of the SS and the desired state, and is the error which the control system attempts to minimize. As the waypoint switches the error immediately increases, causing the graph to appear to jump rapidly, however this is the intended behaviour.

The SS was tasked to follow this figure eight path while maintaining a constant attitude, and while maintaining an attitude tangent to the path.

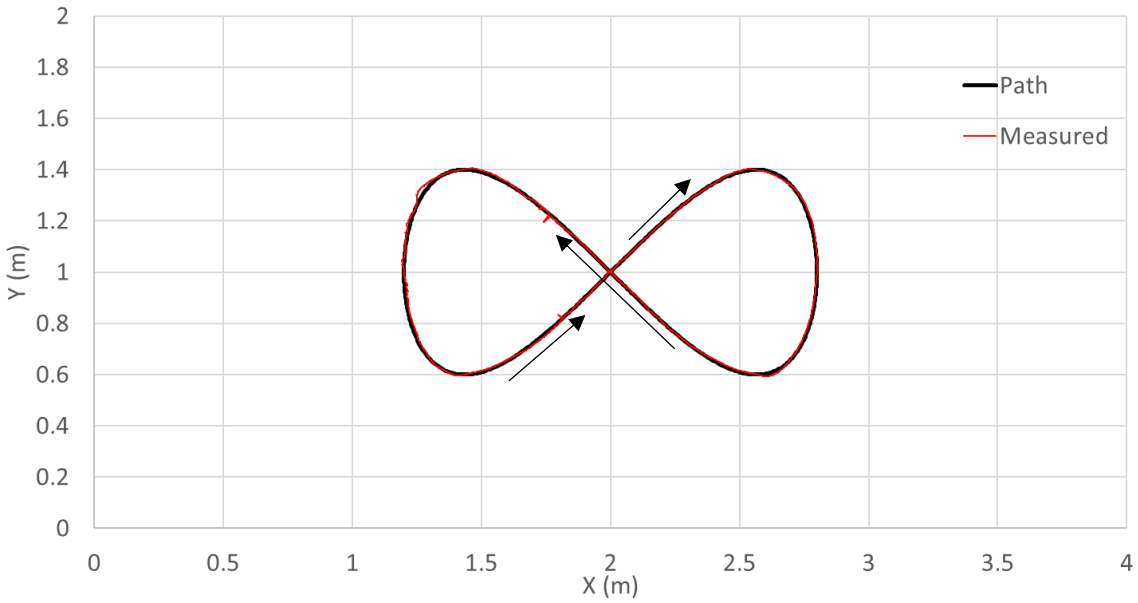

Figure 5.13 - Figure Eight Path Trace
Arrows indicate direction of motion

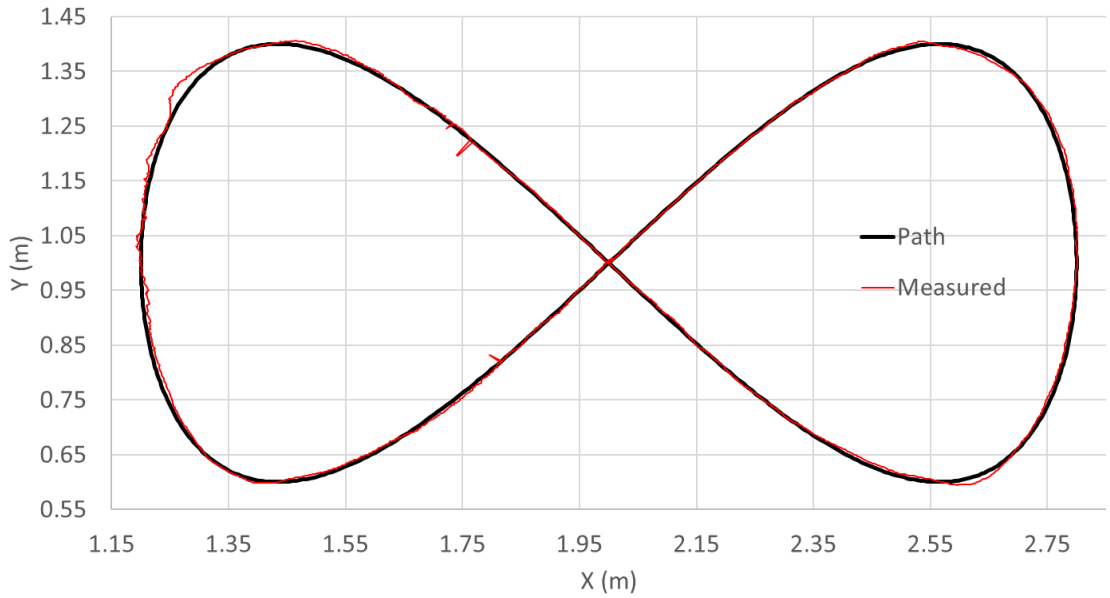

Figure 5.14 - Figure Eight Path Trace Zoom

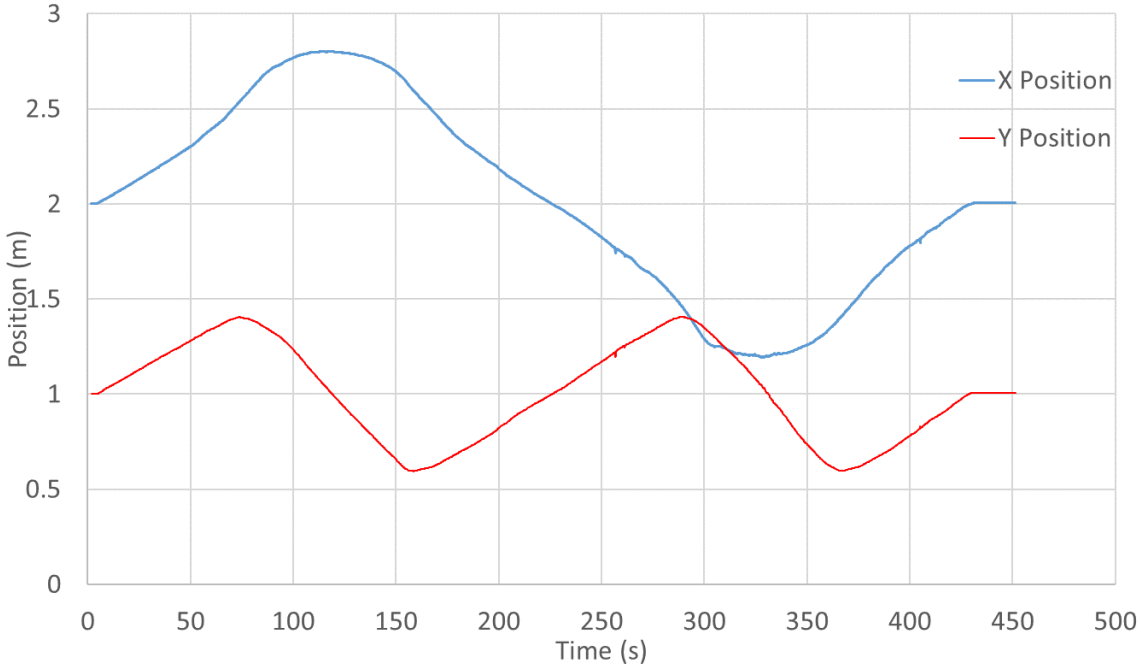

Figure 5.15 - Figure Eight Path Position Vs. Time Plot

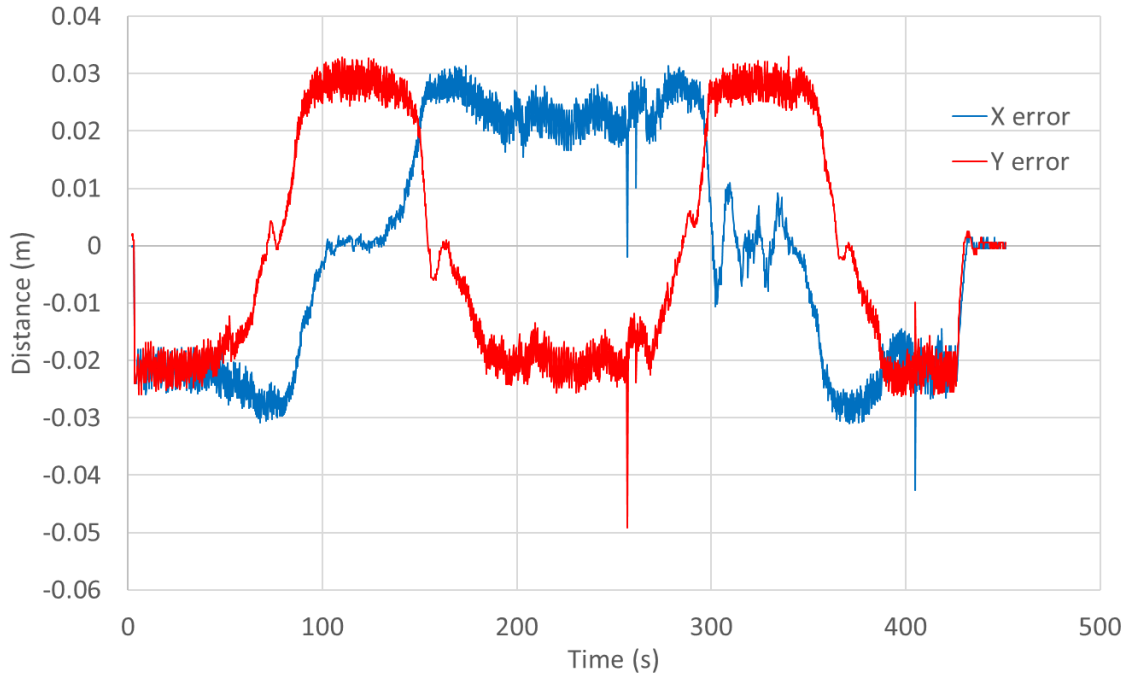

Figure 5.16 - Figure Eight Path Position Error Vs. Time Plot

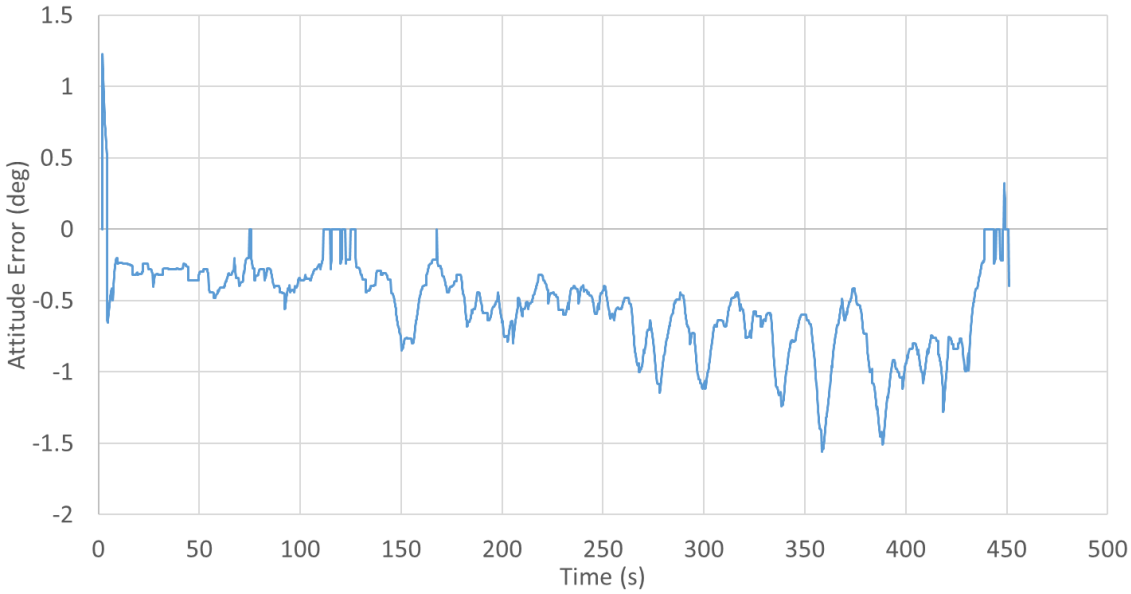

Figure 5.17 - Figure Eight Path Attitude Error Vs. Time Plot

The above figures, Figure 5.13 through Figure 5.17, show the SS performance for the figure eight test path while maintaining a constant attitude throughout the maneuver. Observing Figure 5.13 it is easy to see that the SS was able to follow the figure eight path very closely without major deviation. It can be seen that towards the left-hand side of the figure eight path the SS did begin to deviate from the path by about 3cm, but was quickly corrected. A small deviation like this is likely the result of processor lag which causes the gas thrusters to actuate incorrectly, however the system was able to recover and continue on the path.

It is also worth noting the small spikes which appear to occur in the position and attitude. This is easiest to see in Figure 5.16 at about 260 seconds and 410 seconds. These spikes are not the result of the SS deviating from the path but are caused by errors within the positioning system itself. Since the camera for the positioning system is attached to the moving SS, it is possible for the movements to distort the image. It is also possible that the image that is being processed is corrupted or contains some other errors, however it is easy to see that these errors do not effect the overall performance of the system, as they do not result in any deviation from the path or alteration of the trajectory of the SS.

The nature of these errors is much easier to see in the tangent attitude figure eight test, which is shown in Figure 5.18 through Figure 5.22 below. These error spikes occur much more frequently, and observing Figure 5.21 and Figure 5.22 which show the errors in position and attitude, or rather the difference between the current position and attitude and the current waypoint. As the desired attitude begins to change by a large amount, as occurs

at each curve in the figure 8, the attitude error increases. As this error increases the attitude controller works to reduce this error, causing the SS to rotate. As the error grows the SS rotates faster to reduce this. This increasing rotational velocity causes distortions in the image taken by the camera, which in turn causes errors in the positioning system. The translational velocity of the SS is sufficiently low that it doesn't affect the camera, however rotational rates can easily become large enough to affect the camera.

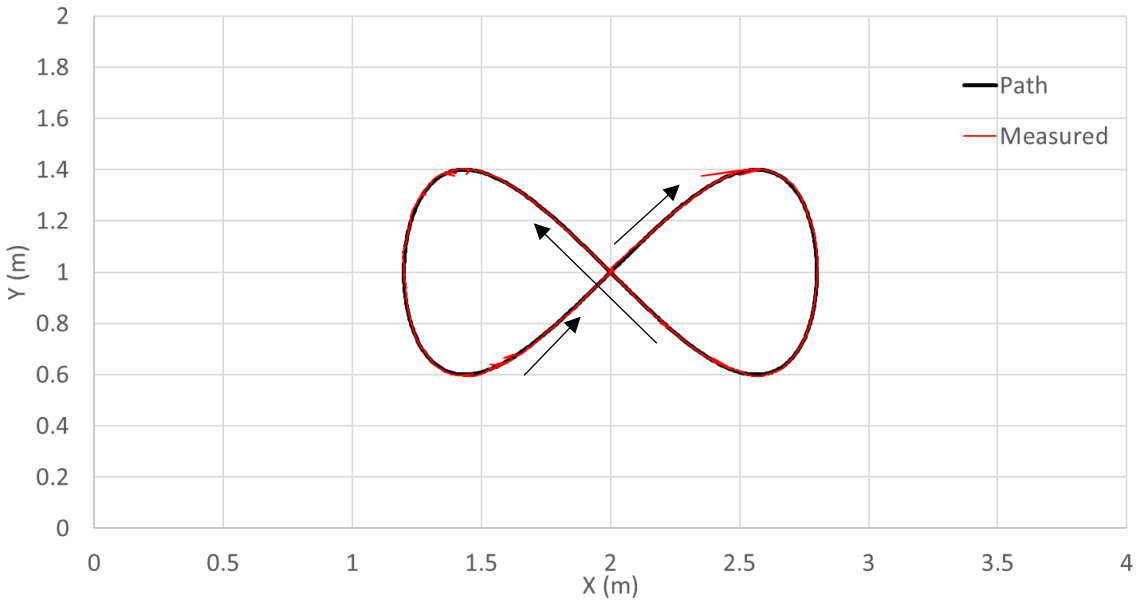

Figure 5.18 - Figure Eight Tangent Attitude Path Trace
Arrows indicate direction of motion

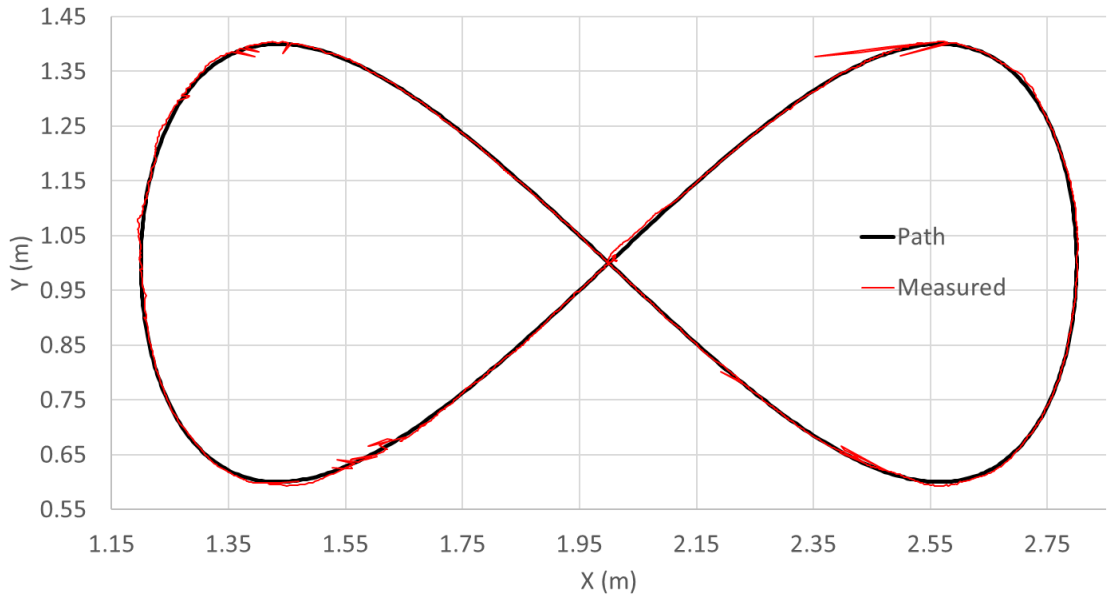

Figure 5.19 - Figure Eight Tangent Attitude Path Trace Zoom

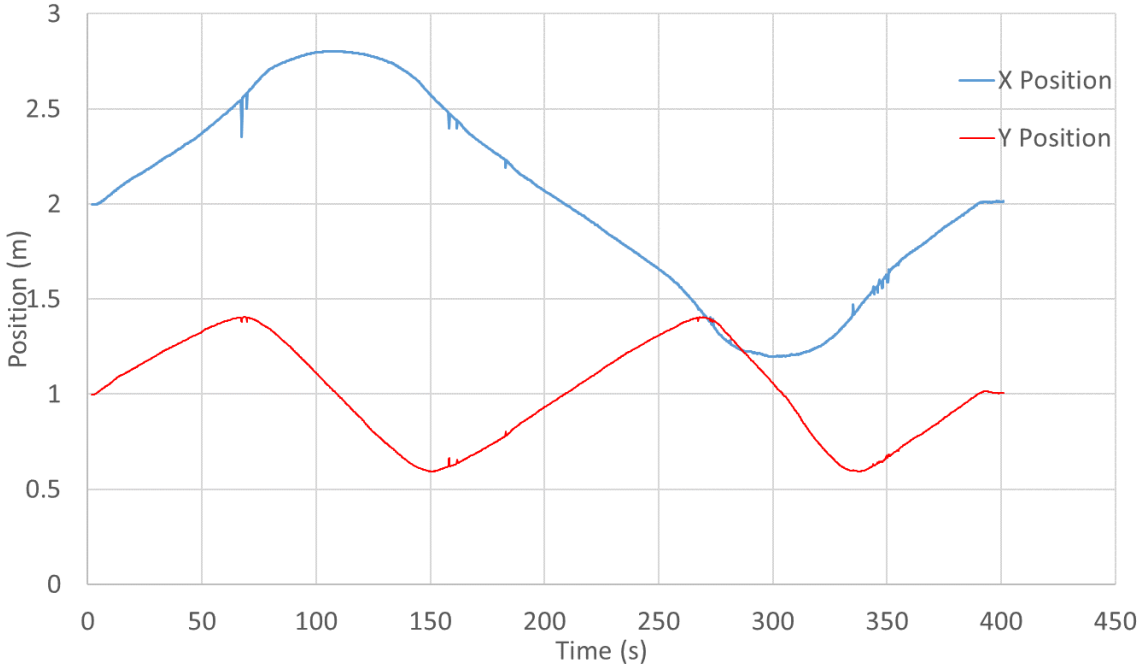

Figure 5.20 - Figure Eight Tangent Attitude Position Vs. Time Plot

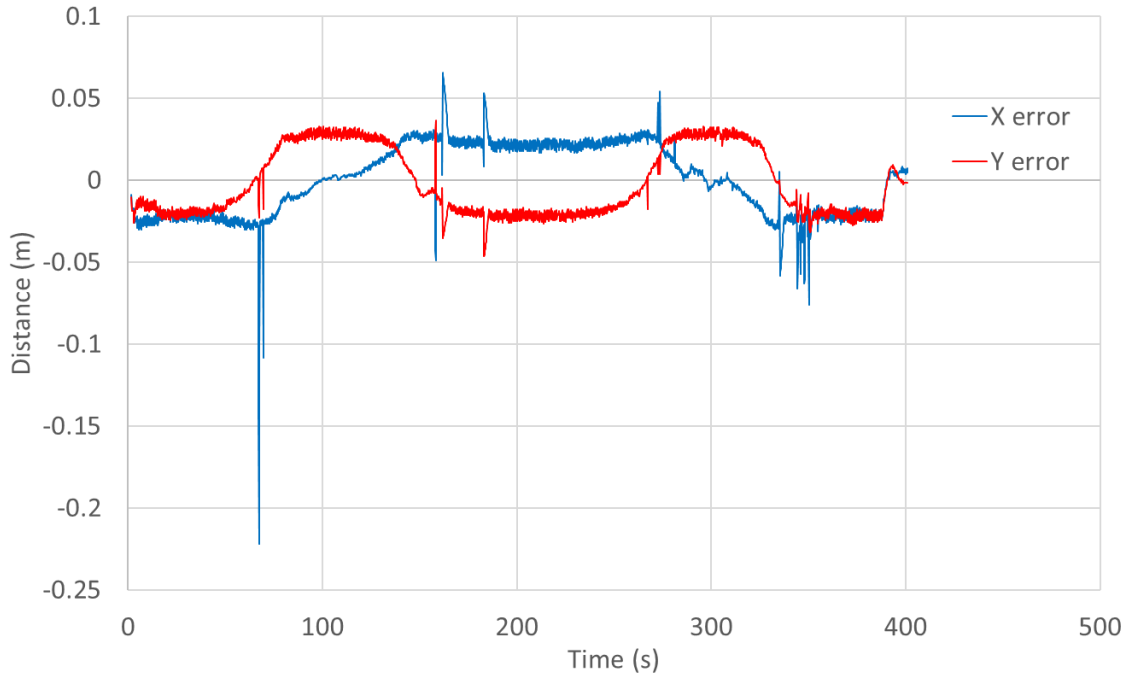

Figure 5.21 - Figure Eight Tangent Attitude Position Error Vs. Time Plot

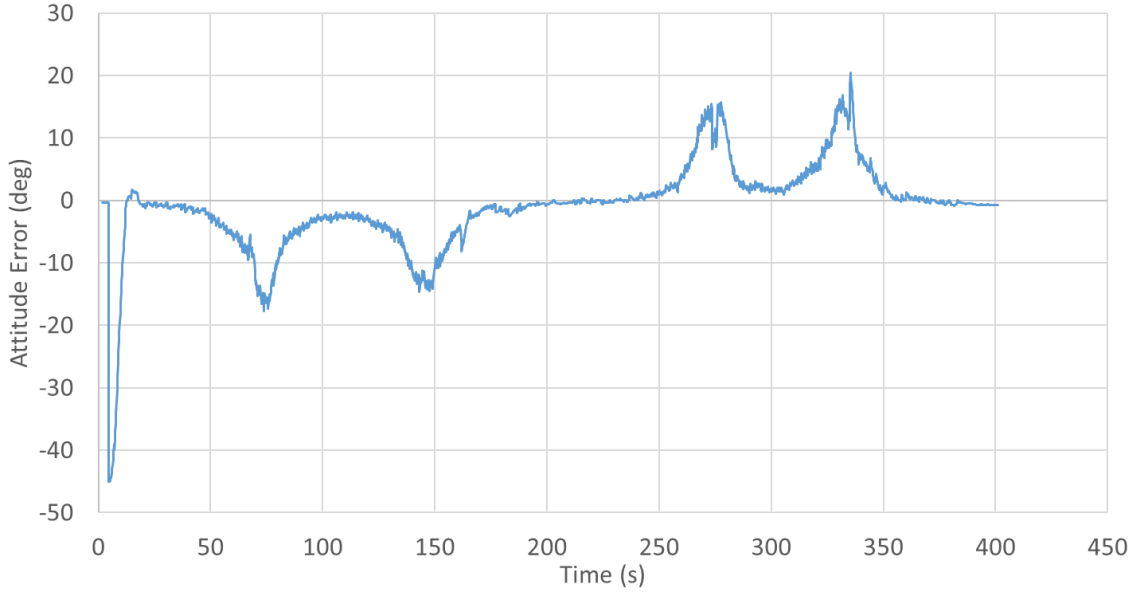

Figure 5.22 - Figure Eight Tangent Attitude Error Vs. Time Plot

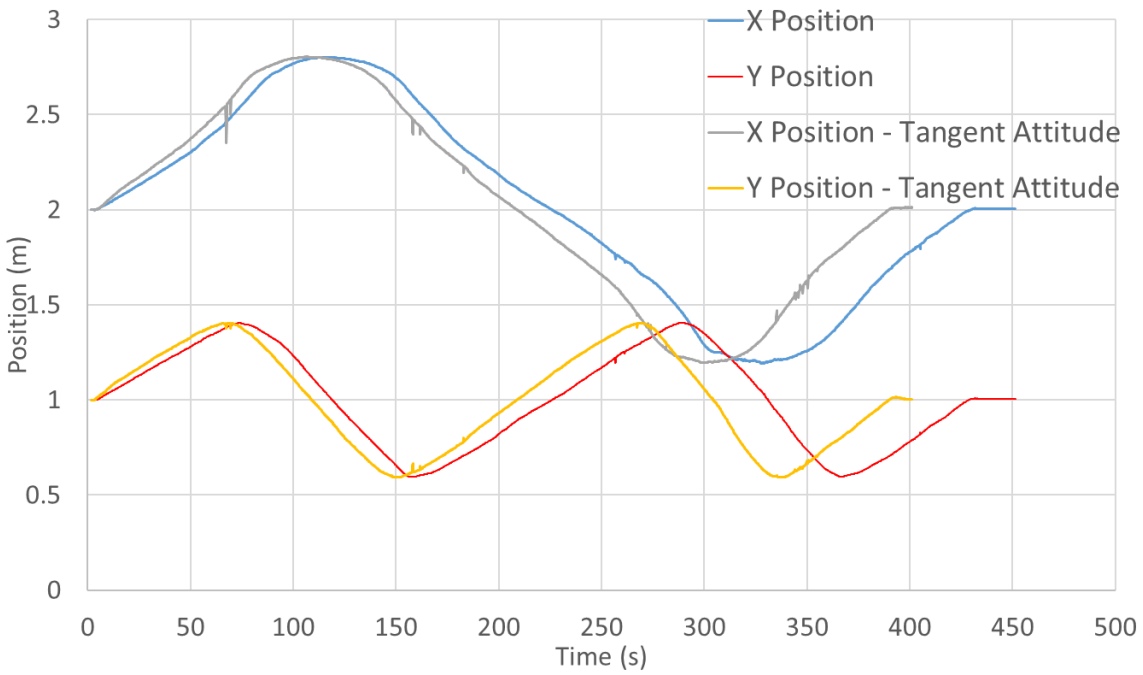

Figure 5.23 - Figure Eight X Y Positions Comparison

Observing Figure 5.23, which compares the X and Y positions of the SS between both tests of the figure eight path, it is evident that both have very similar performance. In both the fixed and tangent attitude tests, the SS was able to follow the path accurately, however it is clear that the tangent attitude path was more prone to errors within the positioning system. These errors are caused by the frequent attitude changes, which cause distortion in the images captured by the positioning system.

The following figures, Figure 5.24 through Figure 5.33, show the performance of the SS for a variety of other paths. For these tests the SS was tasked to maintain a constant attitude. The SS is capable of following these paths with a tangent attitude, as was demonstrated through the figure eight path testing. The tangent attitude operations, however, require

constant attitude adjustments, consume more compressed air to operate the thrusters to make the adjustments, and can cause small errors with the positioning system.

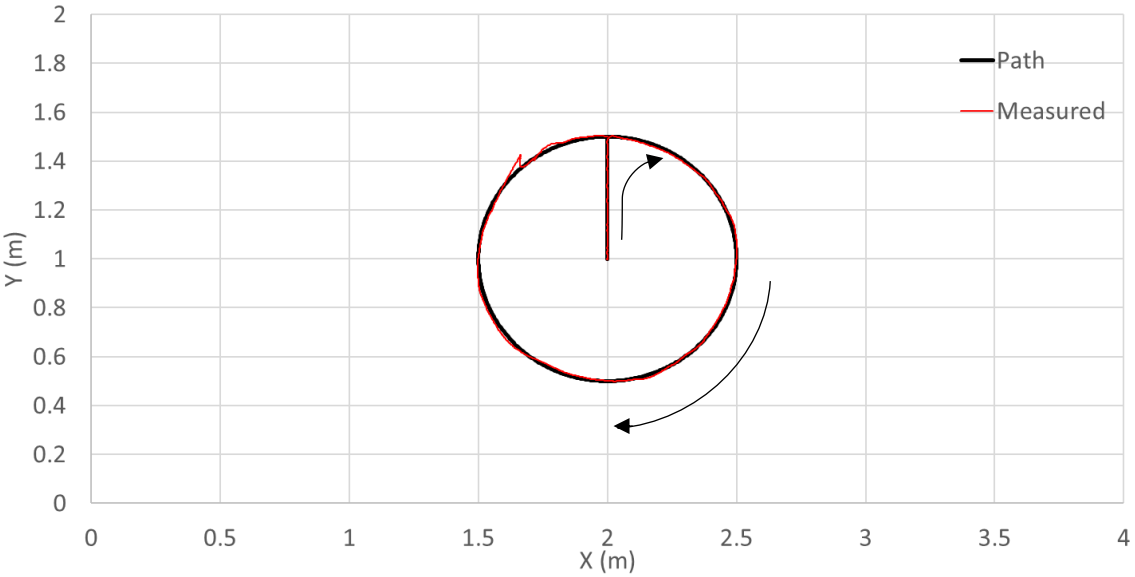

Figure 5.24 – Circle Path Trace
Arrows indicate direction of motion

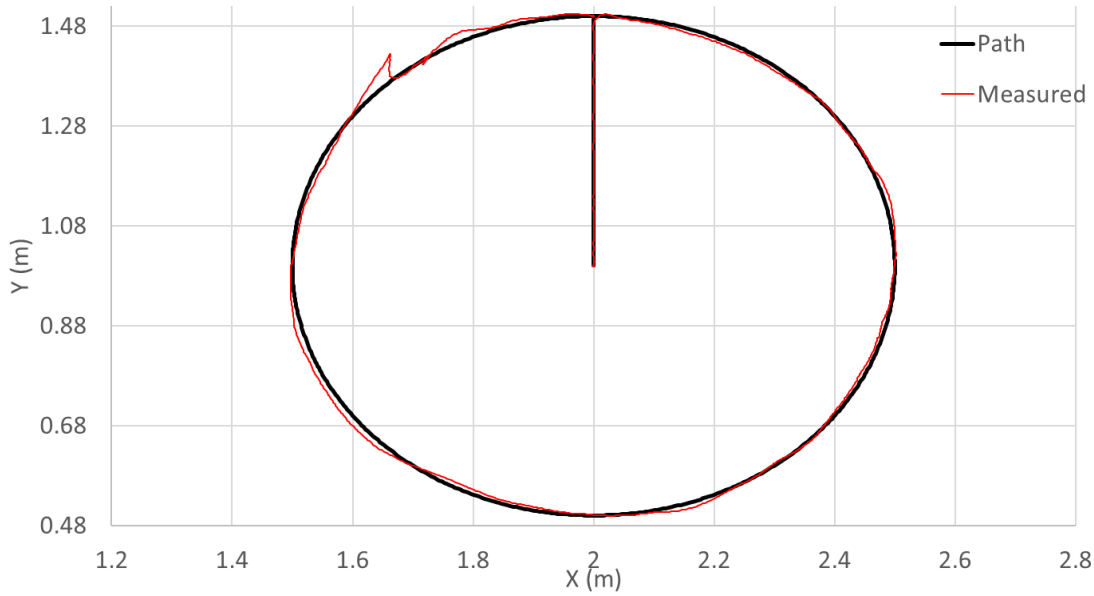

Figure 5.25 - Circle Path Trace Zoom

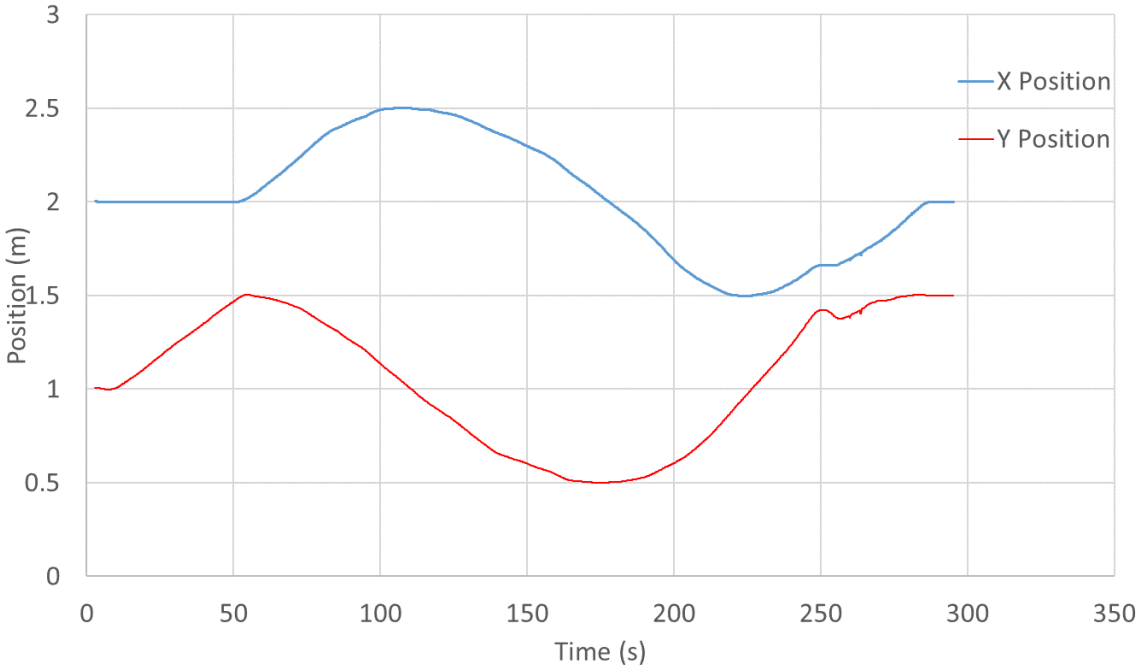

Figure 5.26 - Circle Path Position Vs. Time Plot

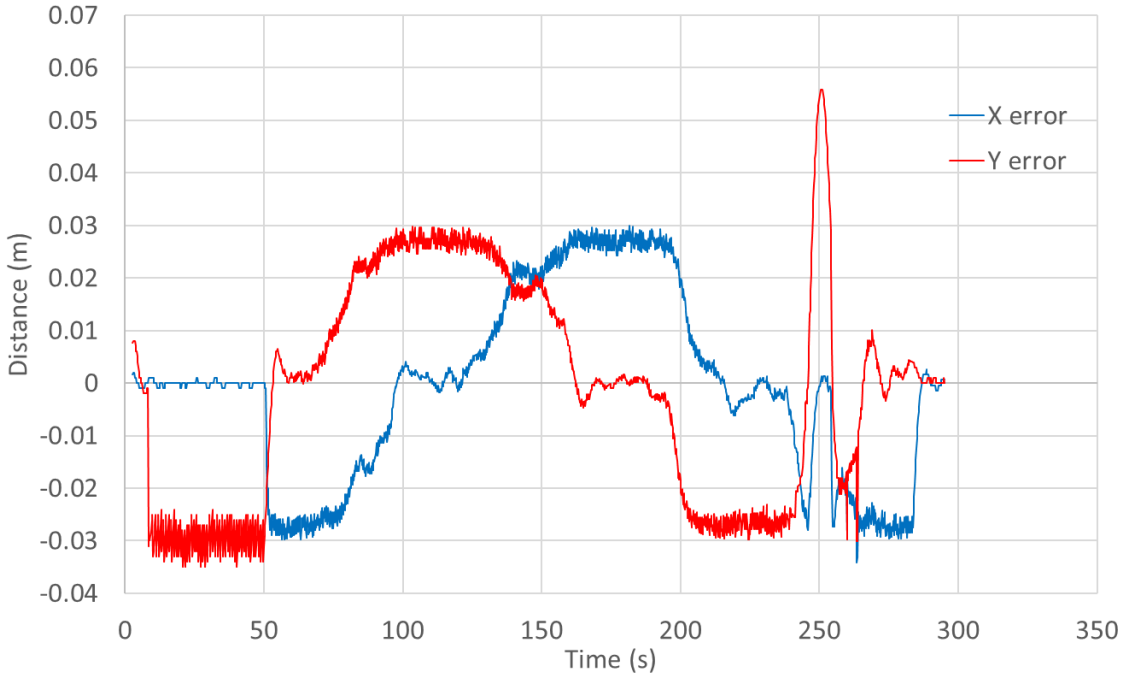

Figure 5.27 - Circle Path Positioning Error Vs. Time Plot

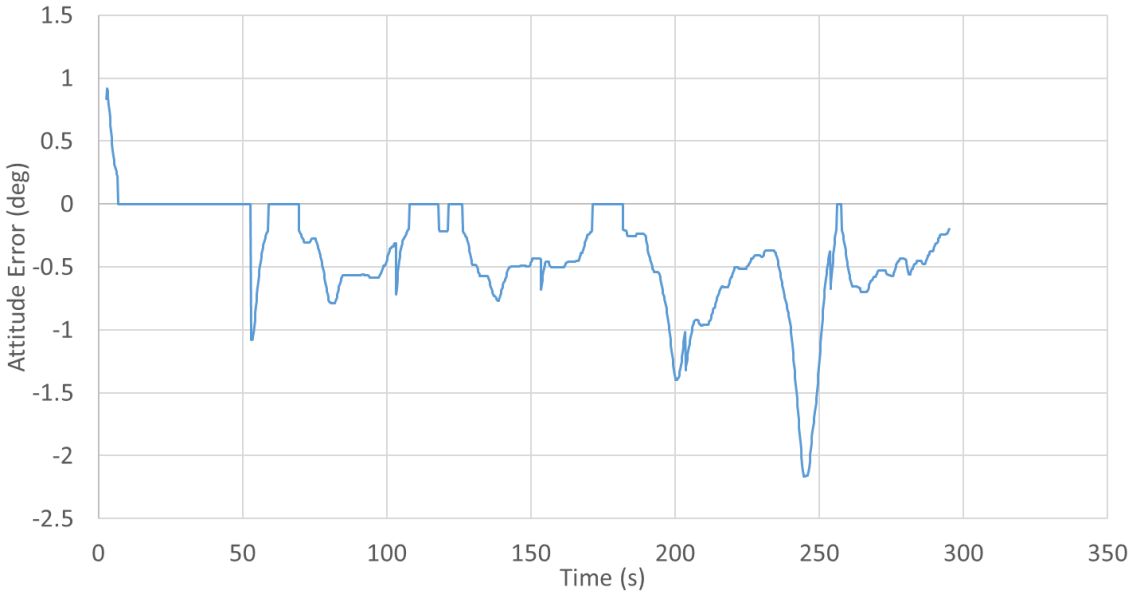

Figure 5.28 - Circle Path Attitude Error Vs. Time Plot

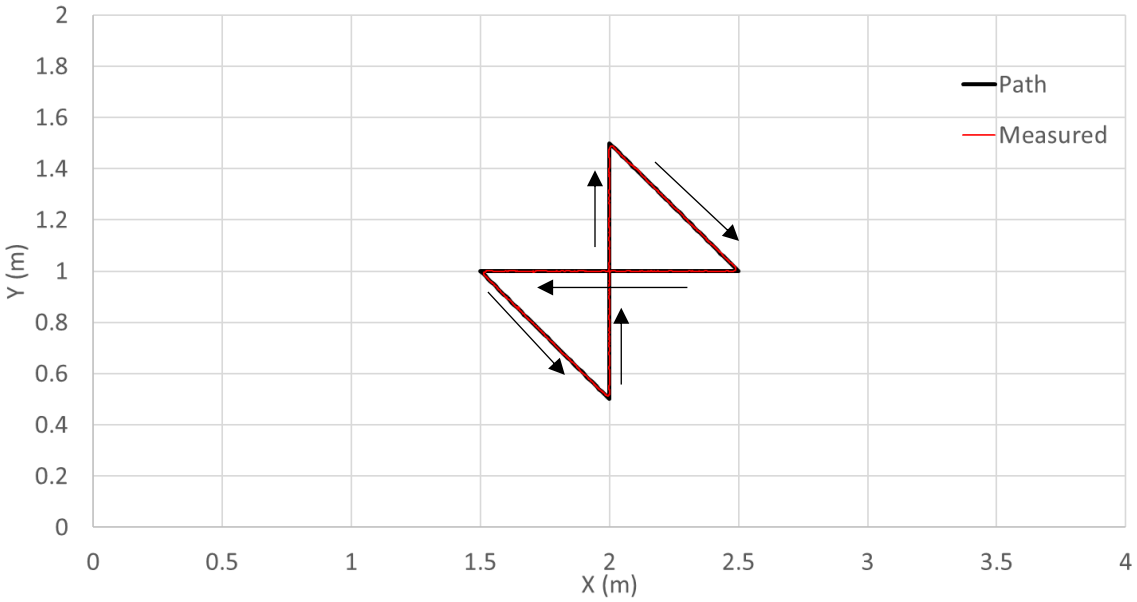

Figure 5.29 - Cross Path Trace
Arrows indicate direction of motion

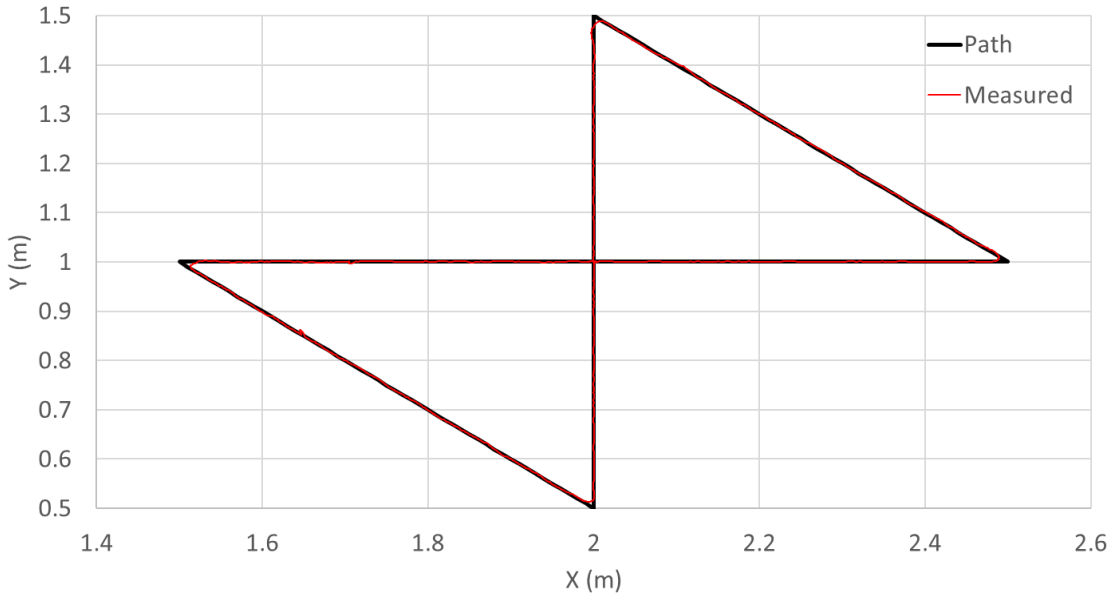

Figure 5.30 - Cross Path Trace Zoom

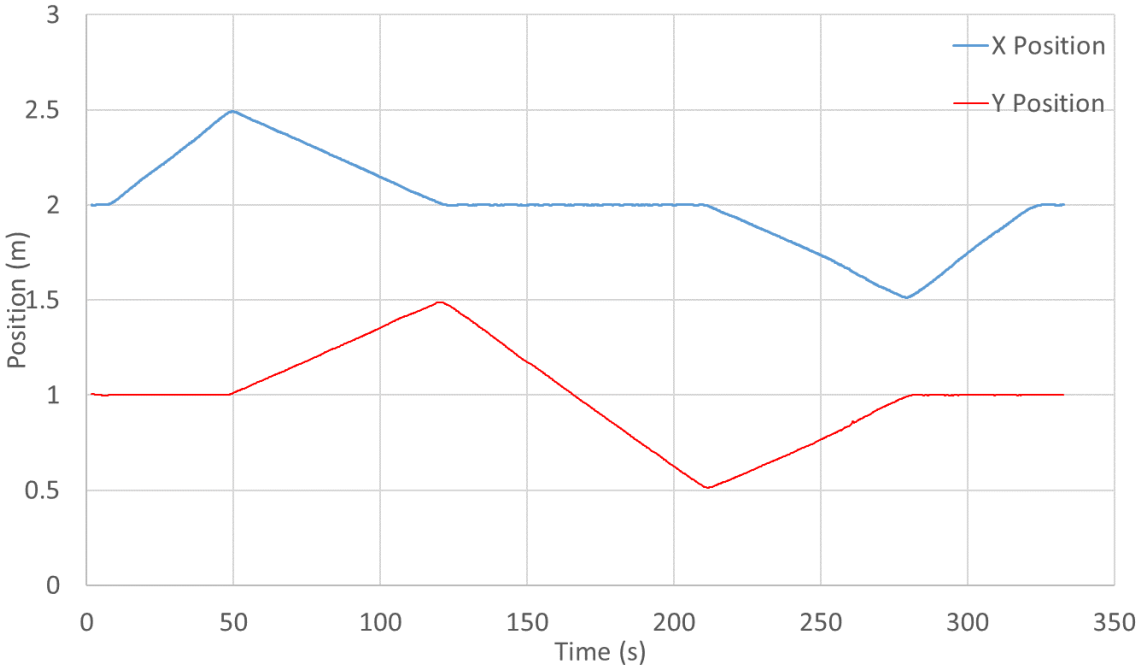

Figure 5.31 - Cross Path Position Vs. Time Plot

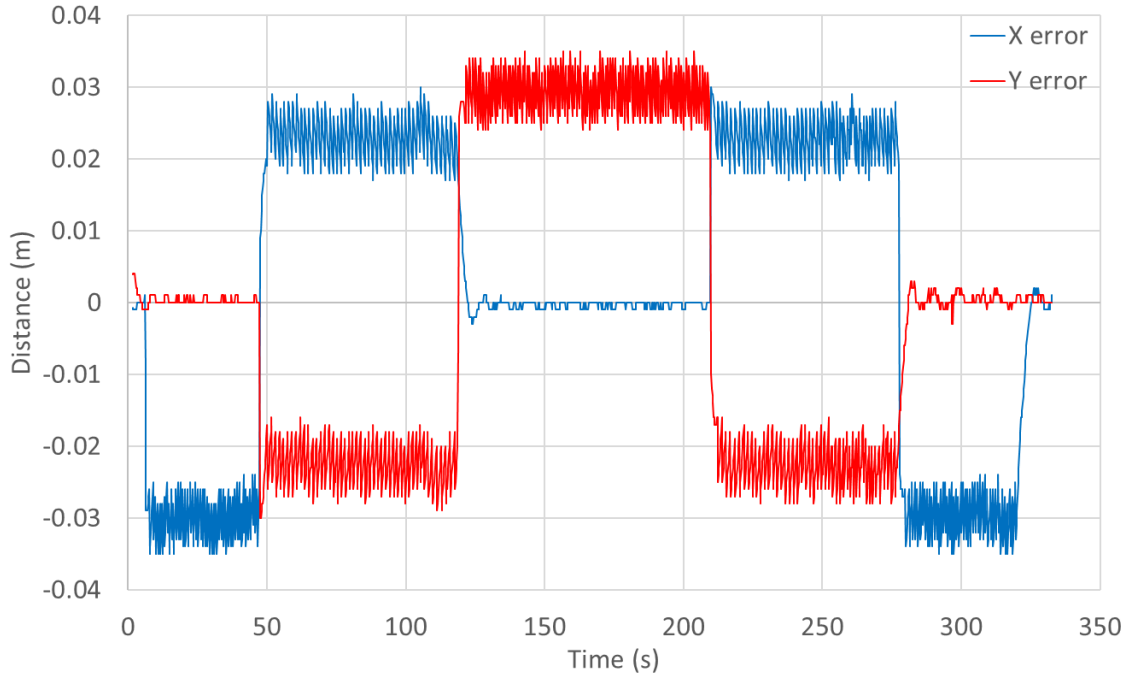

Figure 5.32 - Cross Path Positioning Error Vs. Time Plot

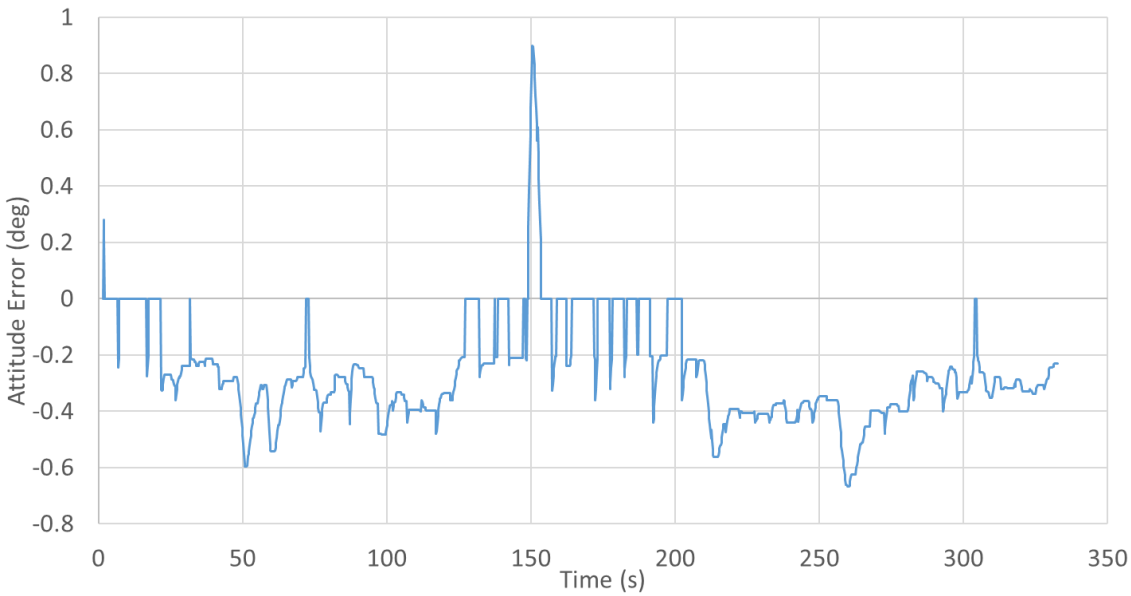

Figure 5.33 - Cross Path Attitude Error Vs. Time Plot

For the circular path following test it is worth noting the deviation from the path that occurs around the 250 second mark. Observing the attitude error plot in Figure 5.28 it can be seen that a deviation in the attitude occurred before the deviation in the position, which occurs immediately after this time in Figure 5.27. Since this deviation in not shown by a single spike in the graph, but rather several points, the SS did actually deviate from the path here. Observing the granite table surface following this it was evident that the surface had accumulated a large amount of dust in that area. The likely cause of this is that the SS hit a piece of debris on the surface of the granite while it was moving, which interfered with the air bearing, this caused the SS to rotate about the point where it had become stuck. As the attitude deviated the system immediately tried correct it, and as this happened with the interfering debris the SS also deviated in its X, Y position. The system was able to recover

from this event, and as such shows the adaptability of the system in the event of such an error.

The cross path experiment was performed to demonstrate the ability of the SS to navigate through sharp turns. The previous path tests only featured various curves. The cross path features only straight lines followed by sharp turns. The SS is able to navigate this path without deviation or overshoot in the turns. There is one small deviation in the attitude, likely due to debris on the surface of the granite, which is quickly corrected and does not affect the position of the SS.

These experimental results clearly show the capabilities of the attitude and position controllers implemented on the satellite simulator through the use of the gas thrusters. The SS are capable of following a complex path, with a variety of features including various straight lines, curves, and sharp turns, with minimal deviation and overshoot.

5.5 Station Keeping

Station keeping describes the process of the SS maintaining the same position and attitude. This process is one of the most important, as many tests may require the SS to be able to stabilize itself and maintain its position and attitude. This requires the control system to also be capable of combating the external forces acting on the system which affect its position, such as air currents within the environment and residual gravitational acceleration due to the imperfectly leveled surface.

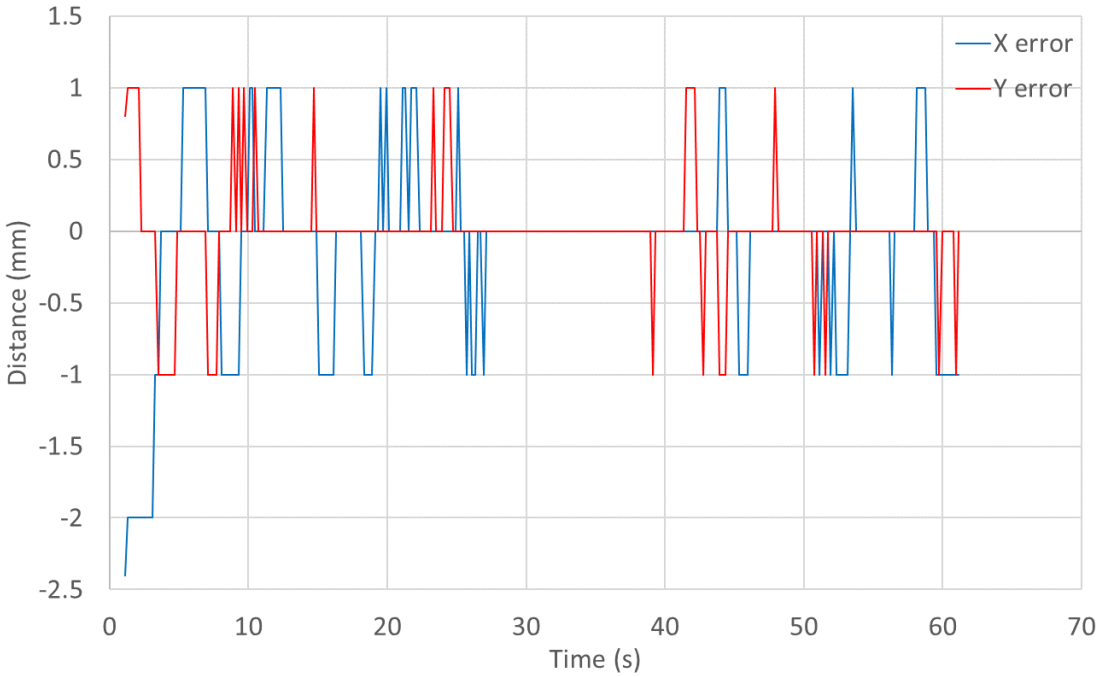

Figure 5.34 - Station Keeping Positioning Error Vs. Time Plot

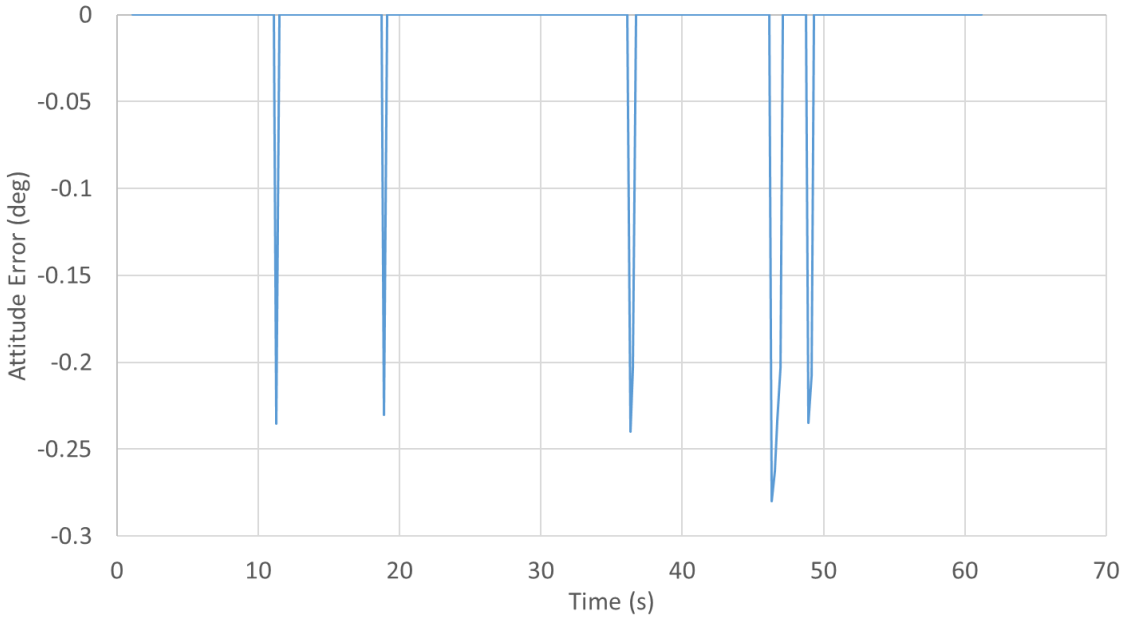

Figure 5.35 - Station Keeping Attitude Error Vs. Time Plot

Figure 5.34 and Figure 5.35 show the station keeping performance of the SS over a 60 second period. It can be seen that the position and attitude are maintained accurately over the entire period. Observing the position error plot shown in Figure 5.34, the SS appears to deviate from its position by ± 1 mm. This deviation is extremely minor, and given that the positioning system is accurate to ± 1 mm, it is the highest performance which can be expected with the positioning accuracy available.

The attitude station keeping, Figure 5.35, shows a similar result. The occasional spikes in the attitude occur at points where the system updates the attitude using the attitude calculated from the camera, and occurs due to noise within the camera system, and drift which has accumulated due to the FOG. Given that the spikes are quite small, are quickly corrected, and do not occur every time the attitude is updated, it can be concluded that the SS is sufficiently capable of performing attitude station keeping.

5.6 Docking

The performance and capability of this testbed for docking and autonomous docking operations is the primary focus of this implementation of this testbed. All other aspects of this project have served to develop the capabilities of these SS systems to perform docking. Here docking refers to the action of the chaser SS, equipped with a magnetic docking probe, making and maintaining contact with the target SS, which is equipped with a magnetic docking receiver. The reason for making the probe and receiver magnetic is that it allows both SS to maintain contact, similarly to what would be done using a mechanical gripper or other such implement to mechanically fix the systems together. While a magnetic

docking implement would not likely be used in actual flight application, due to interference with magnetically sensitive instruments such as magnetorquers, the focus here is not on the development of a docking implement; therefore, the simple magnetic solution is a good choice as it requires little development, can be 3D printed, and requires no additional software to operate.

Similar to the path following data discussed in Section 5.4, Figure 5.36 through Figure 5.49 outline the performance of the chaser SS as it performs docking maneuvers and successfully docks with the target SS. The target SS is at a known point on the granite table and is performing station keeping maneuvers to maintain its position and attitude while floating. The initial position and orientation of both the chaser SS and the target SS are arbitrary, however the test cases shown here allow the docking maneuver to be performed in the center of the field of view of the observer camera for recording purposes. The chaser is capable of completing docking operations from any relative starting position, provided there is sufficient room within the table boundaries to maneuver. It is also important to note that all data collected and shown here was collected from the chaser SS.

For the first test, Figure 5.36 shows the planned waypoint trajectory to dock with the target, and the path as it was traced using the onboard positioning system. Observing the path, the chaser SS was able to execute the intended path. Docking occurred with the target after 140 seconds, which can be seen easily in Figure 5.39 where the X and Y position errors drop and remain around 0. After docking the SS were both left floating and performing station keeping maneuvers, each SS performing these maneuvers independently.

Observing Figure 5.39 and Figure 5.40, the chaser SS maintained its position and attitude while experiencing minor influences from the target satellite which was attached.

Representations of the initial states of the chaser and target SS have been added to the docking path trace. These illustrate the initial testing conditions; the depictions of the SS are not precisely to scale.

Figure 5.36 - Docking Test 1 Path Trace

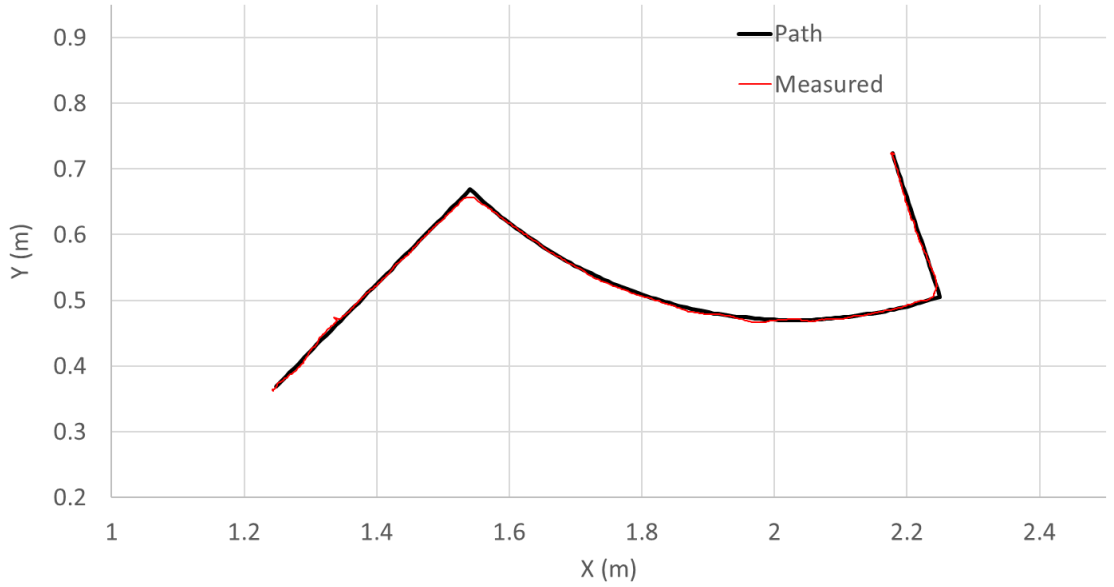

Figure 5.37 - Docking Test 1 Path Trace Zoom

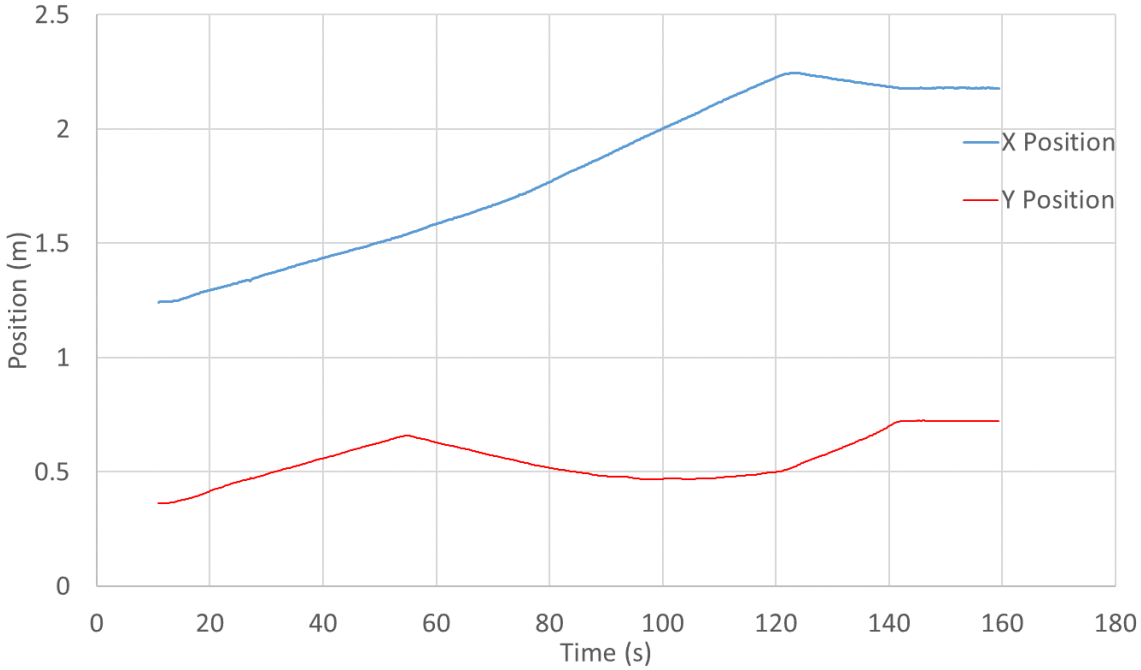

Figure 5.38 - Docking Test 1 Position Vs. Time Plot

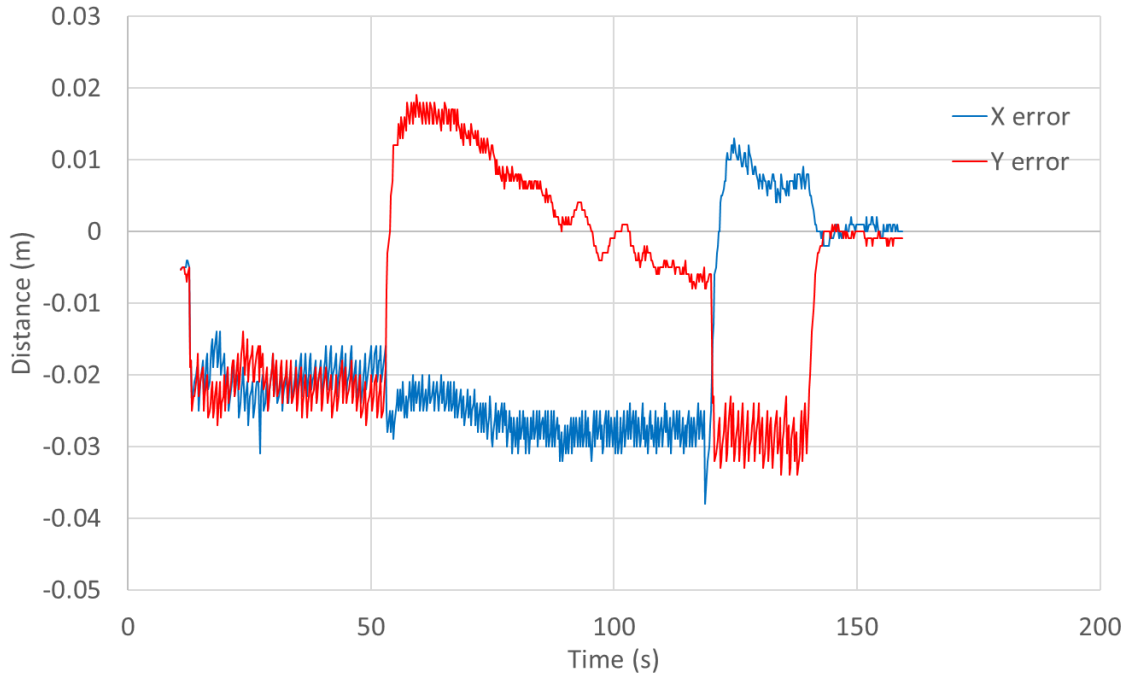

Figure 5.39 - Docking Test 1 Position Error Vs. Time Plot

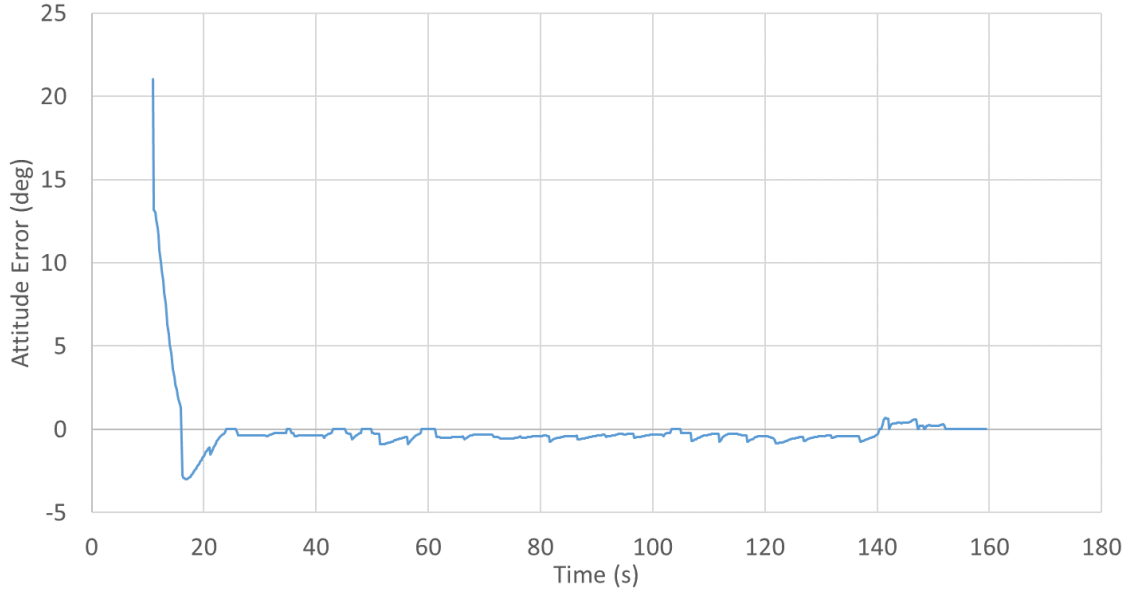

Figure 5.40 - Docking Test 1 Attitude Error Vs. Time Plot

Figure 5.41 - Docking Test 1 Initial Satellite Simulator Positions

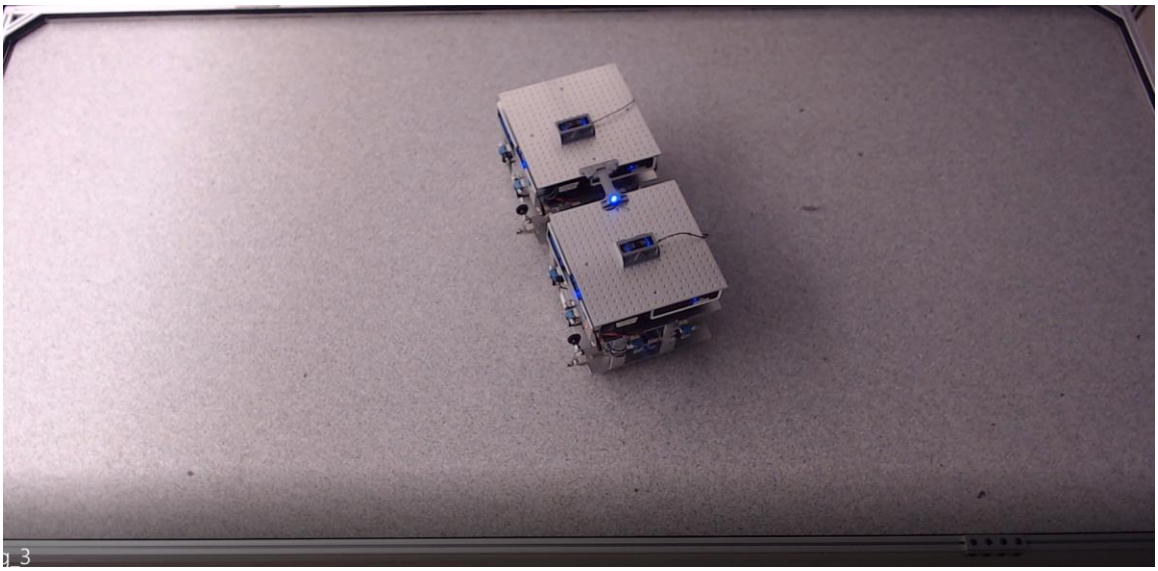

Figure 5.42 - Docking Test 1 Docked Satellite Simulators

The images shown in Figure 5.41 and Figure 5.42 show the initial and final positions of the SS as it docks with the target. The images show that the chaser SS began at a different attitude and a position which did not align the docking mechanisms. The chaser was able

to maneuver to match the attitude of the target and bring itself into position to dock with the target which was free floating and performing station keeping maneuvers.

The below set of figures shows the results for a second docking test. This test involved a similar setup to the previous test, however the target satellite was oriented differently.

Observing the path trace in Figure 5.43, the SS followed the intended trajectory closely. Near the end of the trajectory, as it began the final approach to dock there appear to have been a few bad samples in the positioning system. These samples can be seen more clearly around the 150 second mark in Figure 5.46.

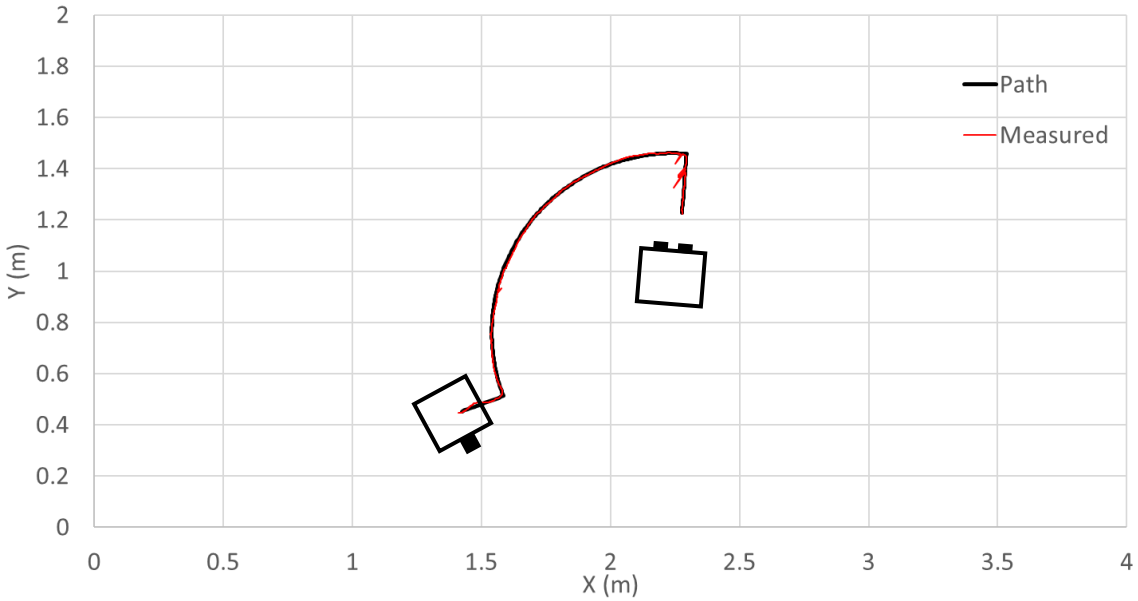

Figure 5.43 - Docking Test 2 Path Trace

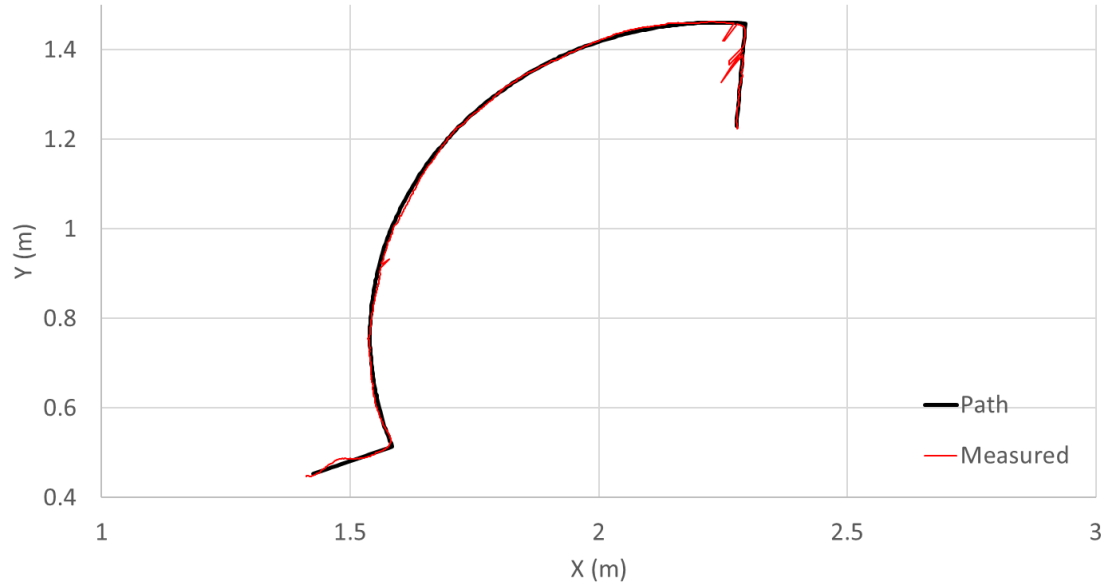

Figure 5.44 - Docking Test 2 Path Trace Zoom

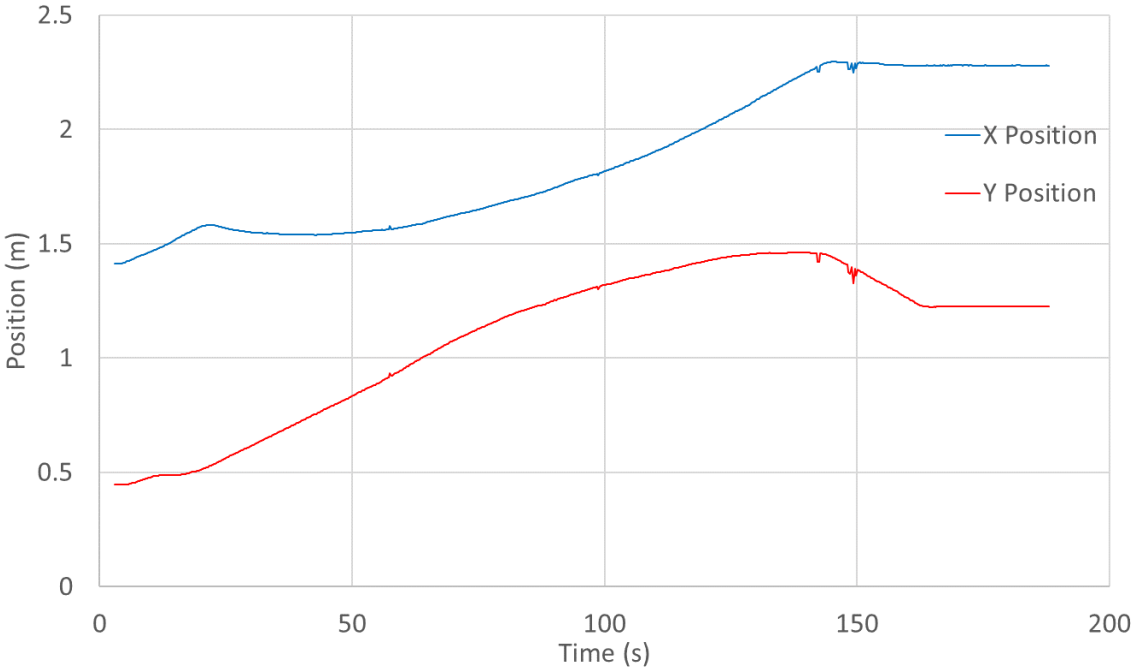

Figure 5.45 - Docking Test 2 Position Vs. Time Plot

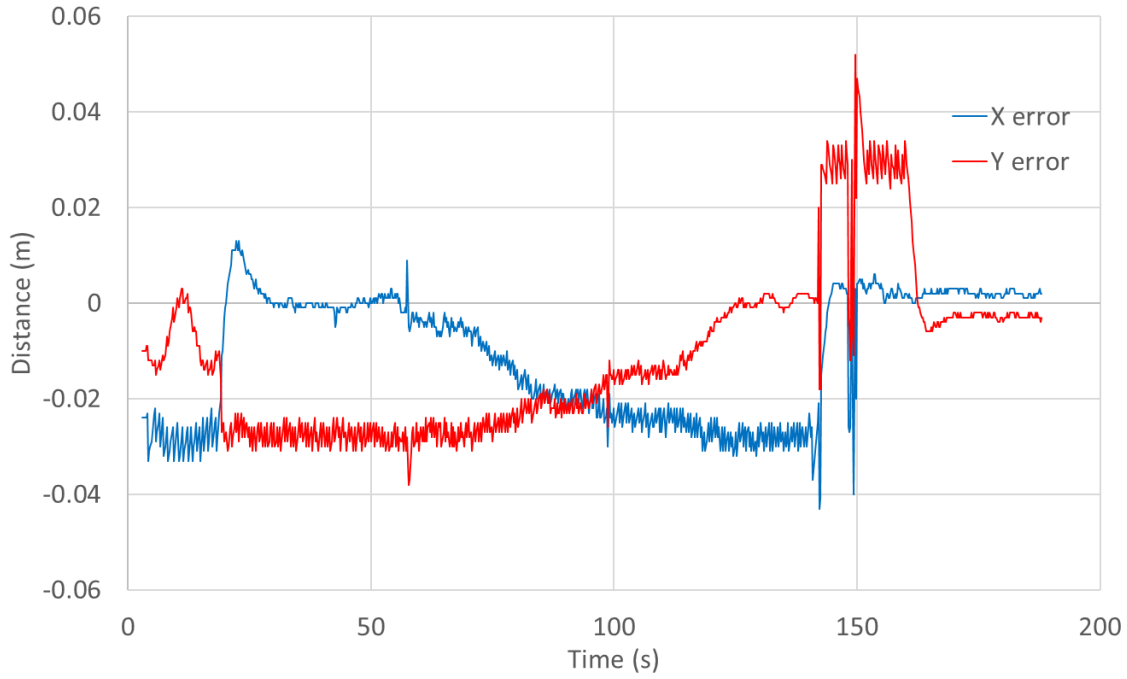

Figure 5.46 - Docking Test 2 Position Error Vs. Time Plot

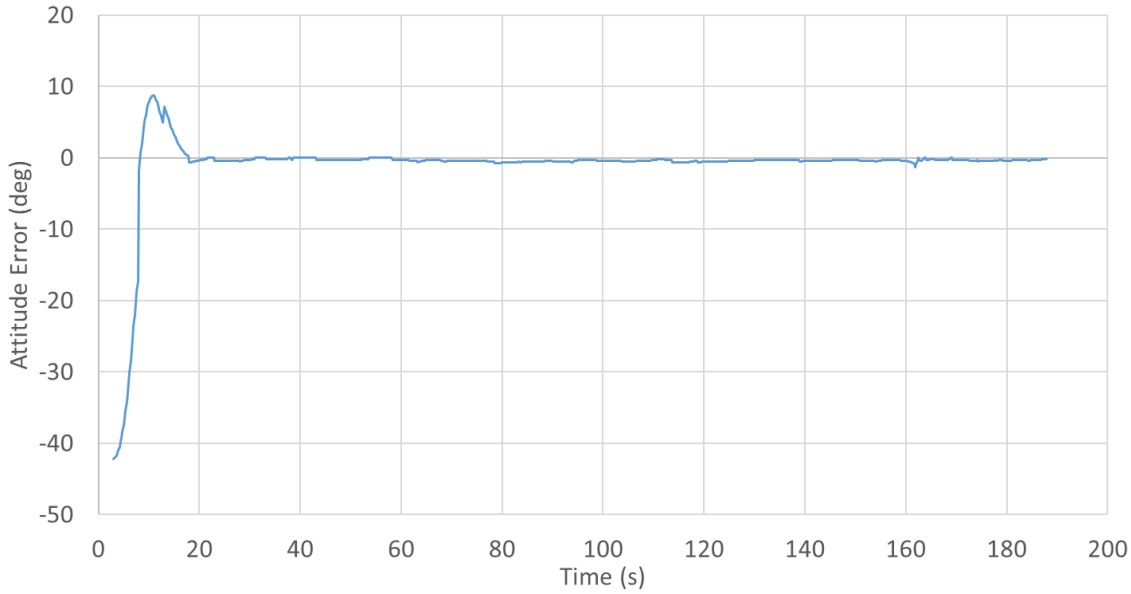

Figure 5.47 - Docking Test 2 Attitude Error Vs. Time Plot

Observing the trajectory plot it is evident that the point where the positioning system provided a bad sample did not affect the overall performance of the system. The position was able to be corrected quickly and the SS maintained its trajectory along the intended path. At about 170 seconds the chaser made contact with the target and was docked.

The position error seen in Figure 5.46 shows that the SS did not achieve exactly the desired position, which would result in a 0 error for the X and Y. This is the result of the magnetic docking system which may have altered the position of the target SS, pulling it as the chaser approached. This in turn would alter the final position of the docked systems. It can be seen however that the system was able to maintain the position and attitude it had when it docked.

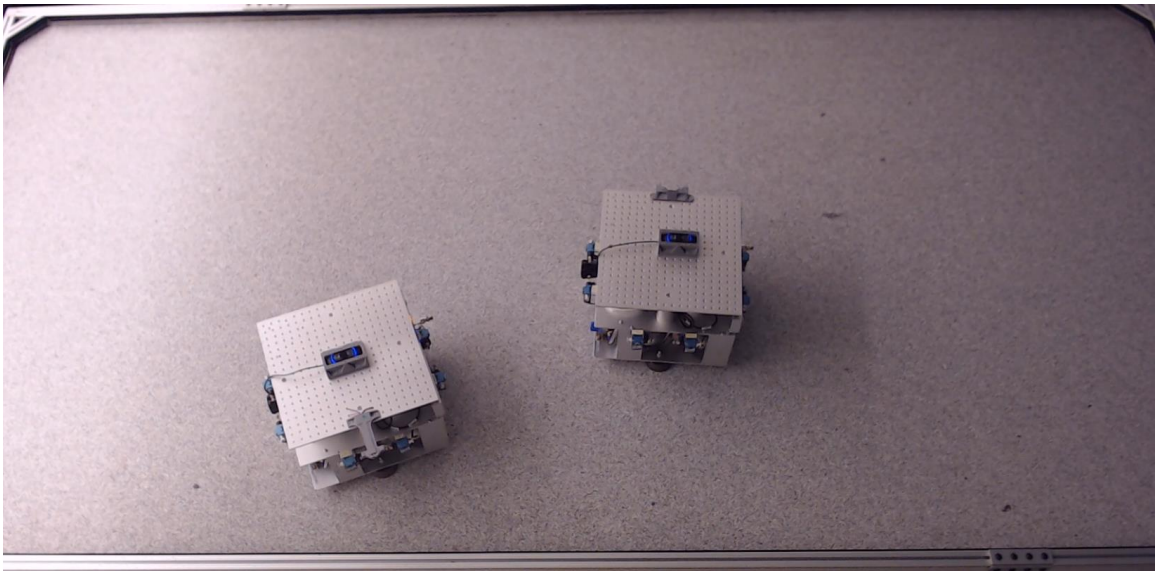

Figure 5.48 - Docking Test 2 Initial Satellite Simulator Positions

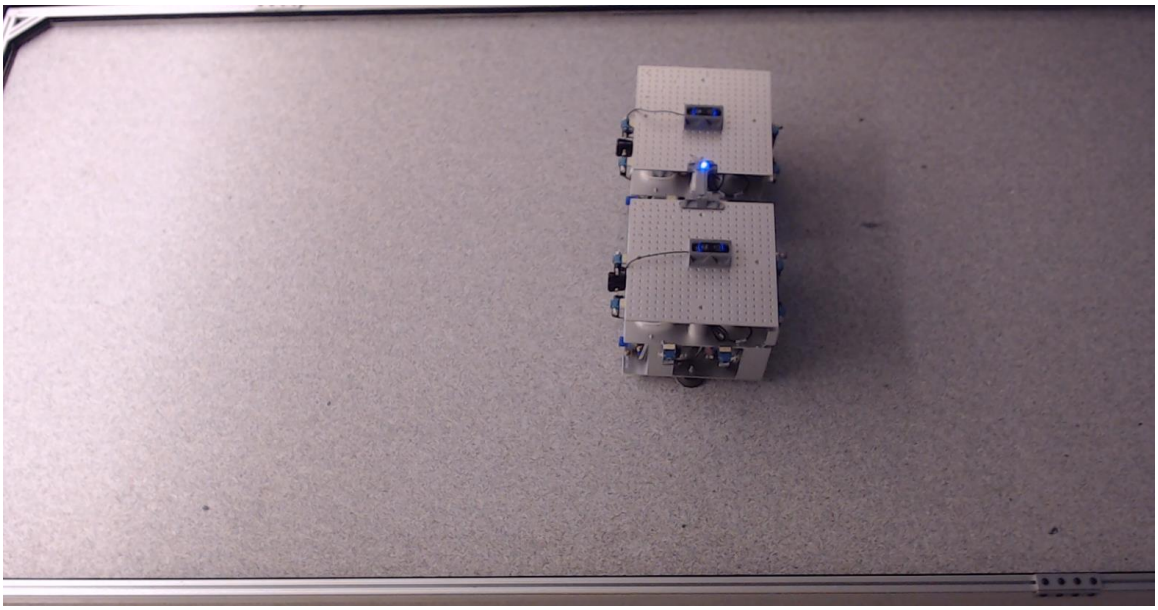

Figure 5.49 - Docking Test 2 Docked Satellite Simulators

The ability of the SS system to successfully perform soft docking operations and maintain post contact stability confirms the operability of this test bed.

Chapter 6 CONCLUSIONS AND FUTURE WORK

Summary: This chapter summarizes the various aspects of the results obtained through this thesis, the contributions of this thesis work, and addresses various areas for future research using this 3DOF testbed.

6.1 General Conclusions

This thesis developed and implemented a 3DOF satellite simulator testbed for the purposes of experimentally analyzing the various aspects involved in spacecraft docking on a ground-based testbed. The testbed makes use of an air bearing system to provide free body motion with 3DOF, and the satellite simulators developed can perform operations using only onboard systems. Existing testbeds in this area of research implement 3DOF satellite simulators, however they are not capable of operating using only the systems found onboard the satellite simulators. Existing testbeds utilize external camera and computer systems to track and calculate controls for the simulators, and then relay the information to the satellite simulator. This thesis covers the various hardware and software systems required to perform autonomous docking procedures with a free floating, stationary target.

6.1.1 Systems Commissioning

The various hardware systems required for the satellite simulator to function were first commissioned in order have them in a usable state. Many of the systems, such as the DAQ, OBC, and FOG either required no calibration or were calibrated by the manufacturer. Provided these parts were installed and connected properly, very little commissioning was required. The gas thrusters all had different output forces initially, these were calibrated using a force sensor to all output a force of 0.065N.

6.1.2 Software Implementation

All systems software was implemented in LabVIEW, and was produced from scratch. The software developed allows for parallel processing of the key system operations, including positioning, GNC, and data logging. The software implemented here has proven to be effective and efficient.

6.1.3 Absolute Positioning System

The absolute positioning system developed here makes use of a series of passive markers mounted to the ceiling over the test platform, and a single observer onboard the satellite simulator. This positioning system operates with a positional accuracy of ±1 mm, and an attitude accuracy of ±0.05°, with an update rate of 15 Hz. This positioning system allows the satellite simulators implemented in this testbed to perform operations using only onboard systems, which sets this testbed apart from existing testbeds.

6.1.4 Control Systems Implementation

The control system implemented here utilizes a series of 3 PD controllers. Each controller handles a different degree of freedom for the satellite simulator, X, Y, and θ. The 3 separate control outputs of combined and assigned to the appropriate thrusters using a mapping matrix. The control system for this implementation is capable of ±1 mm in the X and Y dimensions, and ±0.15° for the attitude, θ. As was shown through the successful path following, station keeping, and docking operations, this control system can perform all required operations with minimal errors.

6.2 Contributions of Thesis Work

This thesis has developed a cutting edge 3 DOF air bearing satellite simulator testbed which improves upon existing air bearing testbeds. The work performed here was motivated by the growing need for the ability to test the various aspects of a space flight mission on the ground with the increasing interest in space in both the private and government sectors. Existing solutions rely heavily on external computational power and positioning systems to determine the position and motions of the satellite simulators, and to calculate the controls which should be executed. The testbed developed here enables the satellite simulators to operate without the use of any external computational support. The ability for the satellite simulators implemented in this testbed to operate using only onboard systems allows them to better emulate autonomous operations. For future advances in spaceflight autonomous operations will be essential, much the same as robotics and automation

enabled modern industries to expand and improve upon tasks which were once performed by humans.

6.3 System Limitations

The testbed implemented here is capable of performing the intended tasks, however it does operate within certain limitations.

The physical size of the granite slab limits the operational space and prevents maneuvers from taking place over a long distance, or certain maneuvers being performed too close to the edge of the platform.

The OBC currently in use of the SS is limited in the types of hardware it can use. It is unable to use spinning hard disks for storage or fans for cooling. Despite these hardware constraints the OBC is capable of operating with solid state hardware and passive cooling and provides a considerable amount of computational power. As was mentioned previously, the OBC is significantly more powerful than a flight capable computer would be, this is another limitation of the OBC. In the current implementation, the SS does not provide a suitable analog for computational power in current flight systems.

The positioning system provides an accurate and serviceable measure of the position and attitude of the SS on the granite surface. The main limitation of this positioning system is the absence of a ground truth measurement. A ground truth would be a secondary measurement of the position and attitude which would be taken as the “correct” measurement, which the positioning system measurement could then be compared against

for verification. Without this ground truth it is not possible to verify the precision of the positioning system. The positioning system is also limited by the capabilities of the hardware being used. The precision which the system is capable of is dictated by the size of the pixels in the camera. A higher resolution camera would be required in order to produce a measurement with a higher precision.

6.4 Future Work

From the research performed throughout the course of this thesis, the following areas of research are considered for future analysis using this testbed:

6.4.1 Robotic Arms

The applications for robotic arms in space are a natural advancement from the implementation of docking technology. Robotic arms enable spacecraft to perform operations with precision and dexterity, such as wire handling and tool manipulation, as well as grasping and manipulating other objects in orbit. Operations involving robotic arms would be simple to test with this testbed, as a robotic arm would simply need to be attached to the existing satellite simulators.

6.4.2 Optimal Controller Design

Controller design is essential for efficient and effective operations in any space mission. In the current implementation, a simple PD controller was implemented to provide a performance baseline and prove the operability of the testbed. Future workings into more advanced and modern control theory would allow the spacecraft simulators to operate with

a high precision, and perform more complex maneuvers. optimal controller design seeks to develop a control system which is optimal for a specific application. Common optimizations for controller are time optimization, where the controller responds and executes maneuvers in a time efficient manner, and fuel consumption optimization, where the controller performs operations while minimizing fuel consumption.

6.4.3 Flight Hardware Analogs

The current implementation of the satellite simulators in this testbed do not strictly adhere to the limitations of space flight hardware, most notably the OBC. While the systems onboard are all analogs of space capable technologies, the OBC is significantly overpowered. This increase in power means that the system cannot reliably provide a baseline for flight software. Future work on this testbed may be done to more effectively emulate the restrictions of a flight grade computer. This could be done by implementing the OBC using a microcontroller such as a Raspberry Pi, which is a good analog for the capabilities of current small satellite flight computers, or by allocating resources on the current OBC to provide a better analog. This could be done through virtualization where an alternative environment, such as Linux, is run alongside the current Windows OS, and given access to a restricted resource pool, limiting the available computational power. This virtualization would allow the system to emulate the power and capabilities of a flight grade computer, without actually having to implement a different OBC, and provide a more suitable test environment for flight software.

References

[1] J. Cook, V. Aksamentov, T. Hoffman and W. Bruner, "ISS Interface Mechanisms and their Heritage," The Boeing Company.

[2] B. Granath, "Gemini's First Docking Turns to Wild Ride in Orbit," 3 March 2016. [Online]. Available: https://www.nasa.gov/feature/geminis-first-docking-turns-to-wild-ride-in-orbit. [Accessed 5 June 20119].

[3] National Aeronautics and Space Administration, "One-Year Mission | About," 8 Aug 2018. [Online]. Available: https://www.nasa.gov/1ym/about. [Accessed 5 June 2019].

[4] F. Garrett-Bakelman and e. al., "The NASA Twins Study: A multidimensional analysis of a year-long human spaceflight," *Science,* vol. 364, no. 6436, 2019.

[5] European Space Agency, "Space Debris by The Numbers," January 2019. [Online]. Available: https://www.esa.int/Our_Activities/Space_Safety/Space_Debris/Space_debris_by_the_numbers. [Accessed 5 June 2019].

[6] M. Wei-Hass, "Space junk is a huge problem - and it's only getting bigger," 25 April 2019. [Online]. Available: https://www.nationalgeographic.com/science/space/reference/space-junk/. [Accessed 5 June 2019].

[7] R. Nemiroff and J. Bonnell, "Astronomy Picture of the Day - Satellites Collide in Low Earth Orbit," NASA, 18 February 2009. [Online]. Available: https://apod.nasa.gov/apod/ap090218.html. [Accessed 5 June 2019].

[8] T. S. Kelso, "Analysis of the 2007 Chinese ASAT Test and the Impact of its Debris on the Space Environment," in *AMOS Conference*, Maui, Hawaii, 2007.

[9] OneWeb, "OneWeb Satellite Stats," [Online]. Available: https://www.oneweb.world/technology#keyshot-module. [Accessed 5 June 2019].

[10] Wikipedia, "Satellite Constellation," [Online]. Available: https://en.wikipedia.org/wiki/Satellite_constellation. [Accessed 5 June 2019].

[11] NASA, "ATV Jules Verne Docks with Station," 23 October 2010. [Online]. Available: https://www.nasa.gov/mission_pages/station/expeditions/expedition16/atv_dock.html. [Accessed 25 August 2019].

[12] SpaceX, "Crew Dragon Docks at the ISS," 4 March 2019. [Online]. Available: https://www.spacex.com/news/2019/03/04/crew-dragon-docks-iss.

[13] NASA, "Cubesat Proximity Operations Demonstration (CPOD)," 2 May 2013. [Online]. Available: https://www.nasa.gov/directorates/spacetech/small_spacecraft/cpod_project.html. [Accessed 25 August 2019].

[14] NASA, "ELaNa 19: RSat," 11 December 2018. [Online]. Available: https://www.nasa.gov/image-feature/elana-19-rsat. [Accessed 25 August 2019].

[15] National Aeronautics and Space Administration, "Sonny Carter Training Facility: The Neutral Buoyancy Laboratory," NASA, Houston.

[16] M. Zebenay, T. Boge, R. Lampariello and D. Choukroun, "Satellite Docking Simulator Based on Hardware-in-the-loop Hybrid Contact Model".

[17] National Aeronautics and Space Administration, "Air Bearing Floor," 22 January 2013. [Online]. Available: https://www.nasa.gov/centers/johnson/engineering/integrated_environments/air_bearing_floor/index.html. [Accessed 7 June 2019].

[18] C. Sun, Chen, Shiyu, J. Yuan and Z. Zhu, "A Six-DOF Buoyancy Tank Microgravity Test Bed with Active Drag Compensation," *Microgravity Science and Technology*, vol. 29, no. 5, pp. 391-402, 2017.

[19] S. M. Lauren, D. L. Dietrich and B. J. Motil, "Microgravity Fluids and Combustion Reseearch at NASA Glenn Research Center," *Journal of Aerospace Engineering*, vol. 26, no. 2, pp. 439-450, 2013.

[20] N. Callens, J. Ventura-Traveset, T.-L. de Lophem, C. L. de Echazarreta, V. Pletser and J. van Loon, "ESA Parabolic Flgihts, Drop Tower and Centrifugre Opportunities for University Students," *Microgravity Science Technology*, vol. 23, pp. 181-189, 2011.

[21] Center of Applied Space Technology and Microgravity, "Weightless In The Drop Tower," [Online]. Available: https://www.zarm.uni-bremen.de/fileadmin/user_upload/Flyer_Fallturm_EN_digitale_Nutzung.pdf. [Accessed 17 June 2019].

[22] E. Kufner, J. Blum, N. Callens, C. Eigenbrod, O. Koudelka, A. Orr, C. C. Rosa, A. Vedernikov, S. Will, J. Reimann and G. Wurm, "ESA's Drop Tower Utilisation Activities 2000 to 2011," *Microgravity Science Technology*, vol. 23, pp. 409-425, 2011.

[23] T. Liu, Q. Wu, B. Sun and F. Han, "Microgravity Level Measurement of the Beijing Drop Tower Using a Sensitive Accelerometer," *Scientific Reports*, 2016.

[24] Canadian Space Agency, "Parabolic Flights," CSA, 27 November 2008. [Online]. Available: http://www.asc-csa.gc.ca/eng/sciences/parabolic.asp. [Accessed 17 June 2019].

[25] J. Pavlich, P. Tchoryk, A. Hays and G. Wassick, "KC-135 zero-G testing of a microsatellite docking mechanism," in *AeroSense 2003*, Orlando, 2003.

[26] M. Shelhamer, "Parabolic flight as a spaceflight analog," *Journal of Applied Physiology*, vol. 120, pp. 1442-1448, 2016.

[27] D. Sternberg, C. Pong, N. Filipe, S. Mohan, S. Johnson and L. Jones-Wilson, "Jet Propulsion Laboratory Small Satellite Dynamics Testbed Simulation: On-Orbit Performance Model Validation," *Journal of Spacecraft and Rockets*, vol. 55, pp. 322-334, 2018.

[28] S. Kwok-Choon, K. Buchala, B. Blackwell, S. Lopresti, M. Wilde and T. Go, "Design, Fabrication, and Preliminary Testing of Air-Bearing Test Vehicles for the Study of Autonomous Satellite Maneuvers," in *31st Florida Conference on Recent Advances in Robotics* , Orlando, 2018.

[29] M. Sabatini, G. Palmerini and P. Gasbarri, "A testbed for visual based navigation and control during space rendezvous operations," *Acta Astronautica,* vol. 117, pp. 184-196, 2015.

[30] J. Hall and R. Marcello, "Laboratory Experimentation of Guidance and Control of Spacecraft During On-orbit Proximity Maneuvers," Naval Postgraduate School, Monterey.

[31] R. Zappulla, J. Virgili-Llop, C. Zagaris, H. Park, A. Sharp and M. Romano, "Floating Spacecraft Simulator Test Bed for the Experimental Testing of Autonomous Guidance, Navigation, and Control of Spacecraft Proximity Maneuvers and Operations," in *AIAA/AAS Astrodynamics Specialist Conference*, Long Beach, 2013.

[32] M. Romano, D. Friedman and T. Shay, "Laboratory Experimentation of Autonomous Spacecraft Approach and Docking to a Collaborative Target," *Journal of Spacecraft and Rockets,* vol. 44, pp. 164-173, 2007.

[33] T. Rybus, K. Seweryn, J. Oles and et al., "Application of a planar air-bearing microgravity simulator for demonstation of operations required for an orbital capture with a manipulator," *Acta Astronautica,* vol. 155, pp. 211-239, 2019.

[34] T. Rybus, J. Nicolau-Kuklinski, K. Seweryn, T. Barcinski, M. Ciesielska, K. Grassmann, J. Grygorczuk, M. Karczewski, M. Kowalski, M. Krzewski, T.

Kucinski, J. Lisowski, R. Przybyla, K. Skup, T. Szewczyk and R. Wawrzaszek, "New Planar Air-Bearing Microgravity Simulator For Verification of Space Robotics".

[35] T. Rybus and K. Seweryn, "Planar air-bearing microgravity simulators: Review of applications , existing solutions and design parameters," *Acta Astronatutica,* vol. 155, pp. 211-229, 2019.

[36] P. Tsiotras, "ASTROS: A 5DOF Experimental Facility For Research in Space Proximity Operations," *Advances in the Astronautical Sciences,* vol. 151, pp. 717-730, 2014.

[37] H. Yao, Y. Wang, J. Cui and et. al, "Implementation of Three DoFs Small Satellite Ground Simulation System," in *AIAA SciTech*, San Diego, 2016.

[38] B. Spratling and D. Mortari, "A Survey on Star Identification Algorithms," *Algorithms,* vol. 2, pp. 93-107, 2009.

[39] G. Lamy au Rousseau, J. Bostel and B. Mazari, "Star Recognition Algorithm for APS Star Tracker: Oriented Triangles," *IEEE A&E Systems Magazine,* 2005.

[40] D. C. C. Liebe, "Star Trackers for Attitude Determination," *IEEE AES Systems Magazine,* 1995.

[41] The Stanford University Aerospace Robotics Laboratory, "Control of Free-Flying Space Robot Manipulator Systems," Ames Research Center, Moffett Field, 1987.

[42] B. Wie, Space Vehicle Dynamics and Control, American Institute of Aeronautics and Astronautics, Inc., 2008.